Mean Motion Resonances and Planetary Scattering

Erik Dahlöf

Lund Observatory
Lund University

2018-EXA135

Degree project of 60 higher education credits (for a degree of Master)
May 2018

Supervisor: Alexander Mustill

Lund Observatory
Box 43
SE-221 00 Lund
Sweden

Abstract:

The observed distribution of giant exoplanet eccentricities and inclinations are significantly larger than what is measured for their Solar system analogues, Jupiter and Saturn. Since the first observations of exoplanets, planet-planet scattering has been proposed as a possible mechanism for exciting the eccentricities and inclinations of giant exoplanets. Many works have showed that indeed the observations can be reproduced fairly well by unstable planetary systems undergoing planet-planet scattering, e.g. Marzari & Weidenschilling (2002); Jurić & Tremaine (2008); Chatterjee et al. (2008). Most of these works disregard mean motion resonances in their simulations.

In the early stages of a planet system the planets are embedded in a protoplanetary disk, consisting mostly of gas. Planet-disk interactions causes planets to migrate which allows for capture into mean motion resonances. This significantly affects the dynamical evolution of the system. In this work I investigate what effect mean motion resonances has specifically on the planet-planet scattering phase of an unstable system. I numerically simulate systems of three Jupiter-mass planets orbiting a solar mass star, including planet-disk interactions to form resonant configurations. The systems are split into two sets: MMR simulations, with all planets locked in mean motion resonance chains before the scattering phase, and NON-MMR simulations, with similar initial orbital elements but no mean motion resonances before the scattering phase.

I find that eccentricity and inclination distributions of relaxed systems are not directly correlated with initial mean motion resonances. Resonances seem to be broken in the first few close encounters and have no further impact on the systems afterwards. However, mean motion resonances have an impact on the initial eccentricity, inclination and semimajor axis of the scattering phase, all of which affects the relaxed systems. Therefore mean motion resonances do affect the scattering phase indirectly through the initial orbital elements. The duration of the scattering phase seems to be uncorrelated with both initial resonance and initial eccentricity and inclination. The onset time of the scattering phase is, in contrast, very dependent on both initial mean motion resonance and initial orbital elements.

Populärvetenskaplig beskrivning

Vetenskap inom planetformation är ett område som har utvecklats mycket sedan de allra första exoplaneterna upptäcktes. Där vi tidigare hade ett enda exemplar av planetsystem att studera (vårt egna Solsystem) har vi idag tusentals observationer av planetsystem runt andra stjärnor. Något som förbryllade forskare då de första upptäckterna gjordes är att exoplaneter, specifikt gasjättar, har betydligt högre excentricitet och inklination än gas jättarna Jupiter och Saturnus i vårt Solsystem. För att beskriva denna avvikelse föreslogs teorin planet-planet spridning (planet-planet scattering). Teorin går ut på att planeter under ett tidigt stadie kommer tillräckligt nära varandra för att interagera kraftigt genom gravitation. Med andra ord så blir gravitationskraften mellan de två planeterna betydlig i jämförelse med gravitationskraften från den centrala stjärnan. Under sådana interaktioner kan de involverade planeterna avvika från sina ursprungliga banor runt stjärnan. Dessa avvikelser involverar bland annat excitation av excentricitet och inklination vilket skulle förklara observationerna.

Många tidigare studier har gjorts inom ämnet planet-planet spridning, ex. Marzari & Weidenschilling (2002); Jurić & Tremaine (2008); Chatterjee et al. (2008). Studierna går ut på att ostabila planetsystem får interagera genom planet-planet spridning tills dess att en eller flera planeter blir utstötta ur systemet. De kvarvarande planeterna bildar då ett stabilt system med förhöjd excentricitet och inclination. Dessa studier bortser från resonanser mellan planetbanor, vilket har en stor effekt på planetdynamik. Resonanser mellan planetbanor uppkommer då planeternas omloppsperioder närmar sig en enkel bråkdel, ex. 2:1 eller 3:2. Viktigt för det här projektet är att resonanser mellan planetbanor kan stabilisera planetsystem som annars skulle varit ostabila.

I det här projektet undersöker jag hur stor effekt, om någon alls, som resonanser mellan planetbanor har på planet-planet spridningen i ostabila planetsystem. Jag undersöker särskillt hur excentricitet och inklination av planeter berörs.

Acknowledgements

I want to thank my supervisor Alex Mustill for pointing me in the right direction and having answers to every possible question. He really has been super helpful. I want to thank Bertram Bitsch who helped me coming up with a strategy for planetary migration. Bertrams research is also a substantial part of my bibliography. I also want to thank Fran Bartolic for his help on planet-disk interactions, David Hobbs and Guido Moyano for reading and correcting my draft.

Contents

Chapter 1

Introduction

1.1 Exoplanets

For a long time our solar system was the only sample of planets and other sub-stellar bodies available for study. Because of this, theories of planetary formation were limited and suffered from extreme bias. Lately, observations of planetary systems orbiting other stars have provided a larger sample of products of the planetary formation process.

The two most common observational techniques to detect exoplanets are the radial velocity method (RV) and the transit method. In short, the radial velocity method detects the small orbital motion of a star around the system center of mass due to a massive planet companion. The transit method detects the dip in luminosity of a star that has a planet passing in front of it.

There are three major groups of observed exoplanets: Super Earths (or small planets), giant planets and hot Jupiters (Winn & Fabrycky 2015). Super Earths are small planets with masses $M < 0.1\,\mathrm{M_J}$, mostly detected by the transit method. According to measured occurrence rates (Winn & Fabrycky 2015), small planets with periods $P < 1\,\mathrm{yr}$ exist around $\sim 50\%$ of Sun-like stars, usually in groups of closely spaced orbits. Super Earths have high density and are most likely terrestrial planets. Giant planets have masses $M > 0.1\,\mathrm{M_J}$ and are much less common than super Earths within the same period limit $P < 1\,\mathrm{yr}$. For $P\,\epsilon[2, 2000]\,\mathrm{yr}$ their occurrence rate is estimated at $\sim 10\%$ for Sun-like stars. In contrast to super Earths, giant planets have been observed at large distances of several AU. However, most of these are detected by the radial velocity method which is not sensitive enough to detect low-mass planets at such separations. Giant planets seems to be large and thus have low densities, which indicates that they are gas planets. Hot Jupiters are giant planets found extremely close to their host stars with periods of a couple of days. Despite being very rare, many hot Jupiters have been detected, mostly due to a strong bias towards large

planets at close separation in the transit detection method.

In the solar system, the planets are roughly coplanar and have nearly circular orbits (Mercury is the only solar system planet with a significantly eccentric orbit). The planets also have a geometric relation between their orbital separation described by the Titius-Bode "law", e.g. Winn & Fabrycky (2015). This motivates a theory where planetary systems form from an ordered system. A popular planetary formation theory is planets forming from small particles and gas in circumstellar accretion disks around young stars. Such disks go by the name protoplanetary disks and the theory is to date the favored planetary formation scenario.

1.1.1 Protoplanetary Disks

Protoplanetary disks are thought to exist around most protostars, e.g. Williams & Cieza (2011). Asymmetries in the collapse of a molecular cloud, forming protostars, leads to a net angular momentum of the system which results in a rotating disk around a rotating protostar. Thus a protoplanetary disk initially has the same composition as the central star, mostly in gas form due to the high temperature. Viscous friction in the disk leads to angular momentum exchange between neighboring layers. Therefore the inner disk is slowly accreted to the protostar as the outer disk spreads outwards.

1.1.2 Planet Formation

The accretion and expansion of the disk decreases temperature and density meaning gas particles can condense into porous solid matter. Dust grains in the disk grow by gas condensation as well as mergers with other grains to form pebbles. Johansen et al. (2014) describes several processes by which pebbles can grow and form massive planetasimals, e.g. streaming instability. Planetesimals continue to accrete pebbles and other planetesimals to form protoplanets eg. Johansen & Lambrechts (2017). Should they grow massive enough they can start accreting gas from the surrounding disk in a runaway process and form gas giants (Johansen & Lambrechts 2017). If the protoplanet fails to get massive enough to start accreting gas from the disk it instead forms a rocky terrestrial planet. Due to lower temperature and therefore larger fraction of solids, gas giants are expected to form at larger separations than small planets, e.g. Winn & Fabrycky (2015).

According to the formation theory described, planets are born from a circumstellar disk with low eccentricity and inclination, with giant planets at larger separations than small planets. One could therefore assume that all planets have low eccentricity and inclination and rotate in prograde orbits. While the solar system is completely consistent with this, exoplanet observations challenge the planet formation theory. Specifically, gas

giants in other planet systems seem to have larger eccentricities and inclinations than seen in our solar system. The exceptions are hot Jupiters which tend to have low eccentricity and inclination, most likely due to strong tidal interactions with the host star at close separation (Winn & Fabrycky 2015). Instead hot Jupiters are difficult to explain as a product of formation close to the host star.

In order to explain these anomalies planetary scattering has been proposed, e.g. Marzari & Weidenschilling (2002); Jurić & Tremaine (2008); Sotiriadis et al. (2017); Chatterjee et al. (2008). Moreover, planetary migration, eccentricity- and inclination damping and mean motion resonances contributes shaping planetary systems, see e.g. Kley (2000); Papaloizou & Larwood (2000); Sotiriadis et al. (2017); Libert & Tsiganis (2011). In short, planetary scattering redistributes semimajor axes and increases eccentricities and inclinations of the involved planets. Planetary migration usually acts to move planets closer to the host star and can lead to mean motion resonance captures and hot Jupiters. Mean motion resonances can stabilize otherwise unstable systems. Furthermore migration of planets in mean motion resonances increases their eccentricities and/or inclinations.

In this work we combine the effects of planetary scattering, planetary migration, eccentricity damping and inclination damping and mean motion resonances to simulations of giant planet systems. The goal of the project is to investigate the effect of mean motion resonances on the planetary scattering.

1.2 Scattering Phase

Consider two planets orbiting a central star. Each planet experiences a gravitational force towards the central star and a disturbing force towards the other planet. Given that the star is much more massive than the planets, the disturbing force is much smaller than that towards the star. In most cases, the disturbing force can thus be neglected and each planetary orbit can be treated as a Keplerian two-body orbit around the host star.

However, if the planets come close enough to each other during their orbits, their mutual gravitational force becomes significant in comparison to that of the star. The Keplerian orbits of the planets are perturbed by this interaction, and as a result orbital eccentricities and inclinations are slightly excited. Subsequent perturbations lead to crossing of orbits and particularly close interactions: close encounters. During a close encounter, the mutual gravitational force between the planets becomes dominant and the planetary trajectories scatter. The new trajectories of the involved planets create new Keplerian orbits. This means that each planet scattering event redistributes the orbital elements of the involved planets. Most importantly for this project: the semimajor axis, eccentricity and inclination changes in each scattering event.

One can imagine such a scattering event putting a planet on a trajectory directly away from the central star. If its velocity during the scattering was large enough the planet is ejected from the system. Ejecting a planet from a system might result in the system becoming stable, given that the separations of the remaining planets are large enough.

For a planet system with sufficiently small separations between its orbits or with eccentric orbits, the disturbing perturbations described above become significant with time. We call this an unstable system. Eccentricities of the planets slowly increase until it reaches a state where orbits are crossing and planetary scattering becomes frequent. During a phase of planetary scattering and disturbing perturbations, the orbital eccentricities and inclinations of the planets vary rapidly. Usually, the net result is a large increase in eccentricity and inclination with time. Eventually one or more planets are ejected and the system becomes stable (relaxed system). This chaotic phase of an unstable planetary system is called the scattering phase.

1.3 Planet-Disk Interactions

1.3.1 Migration

Small orbital separations can be achieved by planetary migration. Gravitational interactions between the protoplanetary disk and the planets results in exchange of angular momentum. Planets that change their angular momentum change their orbital distance to the star and thus migrate. The most important migration mechanism for gas giants is called “Type II”

Type II Migration

A planet exchanges angular momentum with spiral wakes that are created by density waves excited by Lindblad resonances between the planet and the disk, see e.g. Baruteau et al. (2014). Effectively this results in the planet gaining angular momentum from the inner disk and loosing angular momentum to the outer disk. For a sufficiently massive planet, the angular momentum exchange due to planet-disk interactions is greater than the viscous angular momentum exchange trying to replenish disk material, and the planet opens a gap in the disk (Baruteau et al. 2014). When a gap is opened, the angular momentum exchange with the outer and inner disk locks the planet orbit somewhere in the gap. The planet then migrates at the viscous accretion rate of the disk. Type II is usually inward migration unless the planet is at very large semimajor axis where the angular momentum transfer spreads the disk outwards.

Mean Motion Resonance Capture

During planetary migration, two planets can approach each other (or move apart) and the relation between their orbital periods change. As the ratio of periods $T_2 : T_1$, approaches some fractional number, e.g. $2 : 1$, $3 : 2$, etc, the planets encounter a mean motion resonance (hereafter MMR) and have a probability of capturing into this configuration. Planets that are captured in MMR experience a restoring force that keeps the system in the resonant configuration, e.g. $T_2 : T_1$. Resonance captures therefore affect the dynamics of planetary systems.

Examples of a stable MMR in the solar system are Neptune and Pluto, being locked in a $3 : 2$ configuration, the satellites Titan and Hyperion orbiting Saturn, in a $4 : 3$ MMR with Hyperion being the outer body, and the three Galilean satellites Io, Europa and Ganymede, in a $1 : 2 : 4$ MMR chain (orbiting Jupiter).

1.3.2 Eccentricity- and inclination-damping

Works by e.g. Bitsch et al. (2013); Baruteau et al. (2014); Goldreich & Tremaine (1980) show that the angular momentum exchange between planets and a protoplanetary disk in most cases result in continuous damping of eccentricity and inclination of the planets. This means that eccentricity and inclination decreases with time for all planets in a protoplanetary disk.

1.4 Aims of Project

In this project I am interested in multi-planet systems that are dynamically unstable on short time scales. The aim of the project is to investigate the effect of MMR on the scattering phase of unstable planet systems. To do this I simulate 3-planet systems with a central solar mass star. All three planets are of Jupiter mass. The simulations are split into two parts:

MMR: 3-planet systems that migrate and capture into MMR before the scattering phase starts.

NON-MMR: 3-planet systems that undergo a scattering phase without MMR as initial condition.

At the end of each simulation, a set of parameters related to the scattering phase are measured and MMR simulations are compared to NON-MMR simulations.

To date there exists several works showing that the observed giant exoplanet eccentricity and inclination can be fairly well described by planetary scattering, e.g. Marzari & Weidenschilling (2002); Jurić & Tremaine (2008); Chatterjee et al. (2008). These works are only concerned with planet systems after dispersion of the protoplanetary disk and generally initialize the planetary systems with arbitrary or small eccentricities and inclinations. However, the planet-disk interaction phase is important for the initial conditions of the scattering phase. In particular, due to planetary migration, MMR is expected to be a common feature of planetary systems in the protoplanetary disk phase. In this work I tested the implications of ignoring MMR in planetary scattering simulations.

Chapter 2

Theory

For this project we are interested in the dynamics of a planetary system containing three planets and a star. There is no exact analytical solution to this dynamical problem and thus numerical simulations are needed.

However, we can derive approximate analytical solutions for the system using Newton's laws. This is important, both for setting initial conditions and analyzing the results of the simulations. Most of this chapter is based on the book on solar system dynamics by Murray & Dermott (1999).

2.1 Two-Body Problem

The natural starting point is considering a system of only one planet orbiting a star, the two-body problem. By only considering the gravitational accelerations of two bodies, of masses m_1 and m_2, towards each other we can solve the equations of motion for the system exactly, see e.g. Murray & Dermott (1999). This was done first by Newton who showed that the orbit of each body forms an ellipse around the other body. The distance between the two bodies, r, is given by

$$r = \frac{a(1-e^2)}{1+e\,\cos(\theta-\varpi)}, \tag{2.1}$$

which is called Kepler's first law. a is the semimajor axis of the ellipse and e is the eccentricity of the ellipse, given in the range $e \in [0, 1]$. θ is the angle of m_2 with respect to m_1 and a reference direction, which is called the true longitude of m_2. ϖ is the angle from the reference angle to pericenter of m_2, called longitude of pericenter. These two angles are often combined into one, called the true anomaly,

$$f = \theta - \varpi. \tag{2.2}$$

Newton also showed that for each orbit, the orbital period T is determined simply by the semimajor axis and the masses of the bodies involved

$$T^2 = \frac{4\pi^2}{\mu} a^3, \tag{2.3}$$

which is Kepler's third law. $\mu = G(m_1 + m_2)$ with G as the gravitational constant. It is important to note that in a general coordinate system with origin at center of mass, both m_1 and m_2 also orbit in elliptical orbits around the origin.

2.1.1 Orbital elements

So far we have found some important quantities of the orbit of m_2 around m_1. These are the semimajor axis a, the eccentricity e, the true anomaly f, the true longitude θ and the longitude of pericenter ϖ. This section introduces more orbital elements that are useful for the project.

The average angular velocity of m_2, the mean motion, is defined as

$$n = \frac{2\pi}{T}. \tag{2.4}$$

The mean anomaly is the angle represented by n

$$M = n(t - \tau), \tag{2.5}$$

where τ is the time where m_2 is found at pericenter. M is the angle of m_2 with respect to pericenter if the orbital velocity would be constant. If t is known for a certain orbit we also know M. The mean longitude is defined as

$$\lambda = M + \varpi = nt + \epsilon, \tag{2.6}$$

where ϵ is the mean longitude at $t_0 = 0$. Since it is defined from M it cannot easily be interpreted by a position.

As we later will consider the orbits of three bodies, it is important to define a reference plane. The reference plane is usually taken to be the plane in which the most massive body m_1 orbits the center of mass. For the two-body problem, m_1 and m_2 automatically orbit in the same plane. However, this is not the case for three or more bodies. If an orbit is inclined with respect to the reference orbit it has inclination angle i. We then have to introduce some more important angles, seen in figure 7.13. The angle from the reference direction in the reference plane to the intersection between orbit and reference plane is the ascending node Ω. The angle from the intersection to pericenter in the plane of the orbit of m_2 is the argument of pericenter ω. Thus, for inclined orbits ϖ becomes a more abstract angle. Unless $i = 0$ it is measured in two planes. The inclination is in the range $i \in [0, 180]^\circ$, with $i \in [0, 90]^\circ$ representing a prograde orbit.

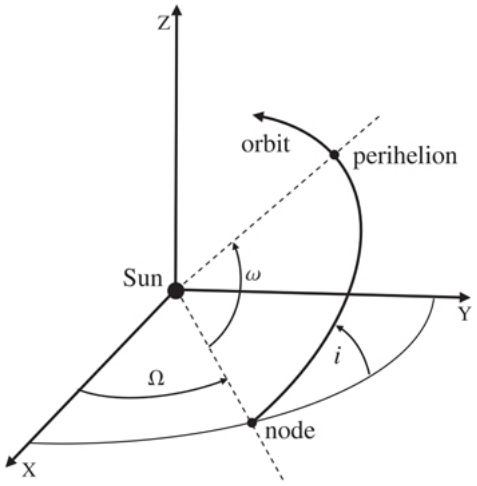

Figure 2.1: The position of the orbit of m_2 relative the reference frame (X, Y, Z) in a coordinate system centered on m_1 (Sun). The inclination of the orbit is given by i. The crossing of the orbital plane and the reference plane (the ascending node) is given by Ω. Pericenter of the orbit measured from the ascending node is given by ω. The figure is taken from Murray & Dermott (1999)

2.2 Disturbing Function

2.2.1 Three-Body Problem

Consider now a system of three bodies m_c, m_i and m_j. We take m_c to be the primary body in a coordinate system centered on m_c. The distances to the other two bodies from m_c are given by the vectors $\mathbf{r_i}$ and $\mathbf{r_j}$. As shown in Murray & Dermott (1999) the equation of motion for m_i can then be expressed as

$$\ddot{\mathbf{r}}_i = \nabla_i(U_i + R_i), \tag{2.7}$$

where U_i is the gravitational potential due to two-body interactions between m_i and m_c. R_i is the perturbing potential from the third body interaction, m_i and m_j, given by

$$R_i = \frac{Gm_j}{|\mathbf{r_j} - \mathbf{r_i}|} - Gm_j \frac{\mathbf{r_i} \cdot \mathbf{r_j}}{r_j^3}. \tag{2.8}$$

This is called the disturbing function. The first term on the right side is the direct term due to interactions between m_i and m_j. The second term is called the indirect term. It is due to the choice of origin of the coordinate system. It can be shown that if the origin is taken as center of mass the indirect term of equation 2.8 vanishes. Equations 2.7 and 2.8 have similar expressions for the other body m_j.

2.2.2 Disturbing function

The distance vectors in the disturbing function can be rewritten as

$$|\mathbf{r_i} - \mathbf{r_j}|^2 = r_j^2 + r_i^2 - 2r_j r_i \cos\,\psi, \tag{2.9}$$

$$\mathbf{r_i} \cdot \mathbf{r_j} = r_i r_j \cos\,\psi, \tag{2.10}$$

where ψ is the angle between the two planets in the reference plane centered on m_c. Equation 2.9 comes from the cosine rule. Using these relations, the disturbing function (equation 2.8) can be expanded into Fourier series in the orbital elements. The details on how exactly to do this are rather lengthy and instead of describing it here I refer to chapter 6 of Murray & Dermott (1999). The result is that the disturbing function can be described as

$$R = \mu' \sum S(a, a', e, e', i, i') \cos\,\phi, \tag{2.11}$$

where the planet on the exterior orbit (largest semimajor axis) is denoted by a prime on all its orbital elements and parameters. A similar expression exists for R'. Here we take $\mu = Gm$ and $\mu' = Gm'$. S is a function of the orbital elements of both planets. The angle ϕ is described by a linear combination of the orbital angles

$$\phi = j_1\lambda' + j_2\lambda + j_3\varpi' + j_4\varpi + j_5\Omega' + j_6\Omega. \tag{2.12}$$

j_1, ..., j_6 are all integers that follow

$$\sum_{i=1}^{6} j_i = 0, \tag{2.13}$$

by Murray & Dermott (1999). The disturbing function, equation 2.11, is therefore a sum of contributions of different functions S and different orbital angle combinations ϕ.

In order to see how the disturbing function affects the planetary motion we go back and look at the equation of motion equation 2.8. If we treat each planetary orbit as a two-body problem with the central star, the disturbing function determines the perturbation to the two-body problem due to a second planet. The disturbing function is used to calculate the changes in orbital elements due to a perturbing second planet. To do this we use Lagrange's planetary equations (Brouwer & Clemence 1961). These give the evolution of the orbital elements in time $\dot{a}$, $\dot{e}$, $\dot{i}$, $\dot{\Omega}$, $\dot{\varpi}$ and indirectly also $\dot{\lambda}$, as functions of the disturbing function R. Clearly, the disturbing function grows large when two planets come close to each other, see equation 2.8. Another important property of the disturbing function is that it provides a significant force in two more cases, called secular evolution and resonance evolution.

2.2.3 Cosine Argument & Secular Evolution

Each term contributing to R (equation 2.11) includes a specific cosine argument ϕ which is a combination of orbital angles (equation 2.12). ϖ, ϖ', Ω and Ω' are slowly varying

angles of the orbit. On the other hand λ and λ' are rapidly varying since they describe the periodic position of the planet, see equations 2.5 and 2.6. With rapidly periodically varying ϕ, the cos ϕ term cancels out over each orbit of the planets,

$\int_0^{2\pi} \cos\,\phi\, dM = 0.$

These orbital averaged disturbing function terms are zero and has no effect on R or R'. However, there are terms R and R' that have ϕ which does not contain λ or λ'. This means arguments that have $j_1 = j_2 = 0$. ϕ is slowly varying for these terms and they provide finite contributions to R and R' each orbit. Such terms are called secular and give rise to disturbing functions that can alter orbits even at large planetary separations.

2.3 Mean Motion Resonances

We have seen that a term of the disturbing function is important only if $\dot{\phi} \approx 0$. The time derivative of ϕ is given by equations 2.6 and 2.12

$$\dot{\phi} = j_1(n' + \dot{\epsilon}') + j_2(n + \dot{\epsilon}) + j_3\dot{\varpi}' + j_4\dot{\varpi} + j_5\dot{\Omega}' + j_6\dot{\Omega}. \tag{2.14}$$

We see that $j_1 n' = -j_2 n$ results in $\dot{\phi} \approx 0$, since ϖ', ϖ, Ω', Ω, ϵ' and ϵ are all slowly varying angles. By equation 2.4 we get

$$j_1 T = -j_2 T'. \tag{2.15}$$

So there exist relations between the orbital periods that provide a nonzero averaged disturbing function. The fact that j_1 and j_2 can only be integers means that this can only occur for certain period relations, e.g. 2:1, 3:1, 3:2, etc. Equation 2.15 describes the nominal (approximate) resonance configuration. Exact MMR is described by setting the full equation 2.14 to zero ($\dot{\phi} = 0$), and is therefore slightly shifted from the condition described by 2.15.

As an example, for first order mean motion resonances, e.g. 2:1, 3:2 etc., we have $j_1 = -j_2 + 1$. To satisfy the condition 2.13 we then need the other angle integers j_3, j_4, j_5 and j_6 to sum up to minus one.

More specifically, one can show that (see chapter 8 of Murray & Dermott (1999)) to lowest order, each term in the disturbing function can be expressed as

$$\langle R \rangle \propto \frac{\mu'}{a'} e^{|j_4|} e'^{|j_3|} s^{|j_6|} s'^{|j_5|} cos\,\phi, \tag{2.16}$$

with a similar expression for $\langle R' \rangle$. s is related to i by $s = sin\,\frac{1}{2}i$. Since $e < 1$ and $|s| \leq 1$ the strongest resonances are those with small integers j_3, j_4, j_5 and j_6.

We call resonances either eccentricity- or inclination-resonances depending on which integers j_i are used for the resonant angle ϕ. As an example, a first order internal eccentricity resonance is given by:

$$\phi = j_1\lambda - (j_1 - 1)\lambda - \varpi. \tag{2.17}$$

This is an eccentricity resonance because ϕ includes ϖ (j_4 in equation 2.12 equals -1 while j_3, j_5 and j_6 are all zero). According to equation 2.16 the disturbing function for this resonance is proportional only to e. As we will see later in section 2.3.4 the type of resonance determines whether eccentricity or inclination is excited during migration in MMR. An important note here is that the sum of integers j_5 and j_6 can ONLY be even integers e.g. $j_5 + j_6 = 0, 2, 4, ...$

2.3.1 Qualititive Description of Mean Motion Resonances

Mean motion resonances are repeated conjunctions at the same orbital location. Consider two planets with the following nominal relation of periods

$$\frac{T'}{T} = \frac{|j_1|}{|j_2|}. \tag{2.18}$$

It can be shown (Murray & Dermott 1999) that the period between conjunctions is then given by

$$T_{con} = \frac{j_1 - j_2}{j_2}T' = \frac{j_1}{j_2}T, \tag{2.19}$$

where T and T' is the period of the inner planet and outer planet respectively. So for a 2:1 resonance, we see that a conjunction occurs once every period of the outer planet. This can be seen in figure 2.2. For a 3:1 resonance a conjunction occurs every second orbit of the outer planet etc. This means that conjunctions always occur at the same locations in space. By taking into account exact resonances, e.g. precession rates $\dot{\varpi}$, $\dot{\Omega}$, $\dot{\epsilon}$ etc. the conjunctions no longer occur at the same locations in space, but instead at the same locations in a rotating reference frame.

Let's now look more closely at what happens at these conjunctions. In figure 2.3 we show again a 2:1 nominal resonance location. The outer planet is on a circular orbit ($e = 0$) and has some finite mass. The inner planet has a slightly eccentric orbit and is for simplicity considered massless. In this situation the conjunction is slightly offset from the pericenter of the inner planet.

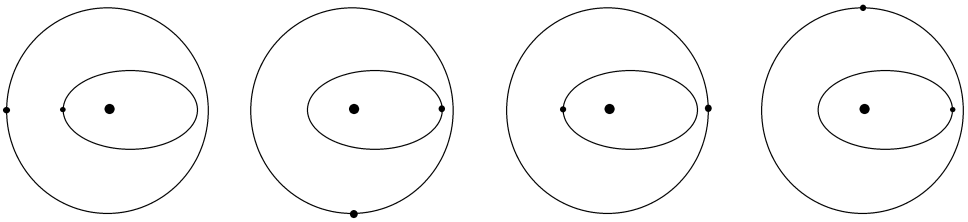

(a) t_1 (b) t_2 (c) t_3 (d) t_4

Figure 2.2: Two planets in an exact 2:1 period relation. The outer planet has $e = 0$ while the inner planet has some finite eccentricity. Conjunctions always occur in the position at t_1. $t_1 = n \cdot T'$ for $n = 0, 1, 2, ...$ and T' as the period of the outer planet. $t_2 = t_1 + 1/4 \cdot T'$, $t_3 = t_1 + 1/2T'$ and $t_4 = t_1 + 3/4 \cdot T'$.

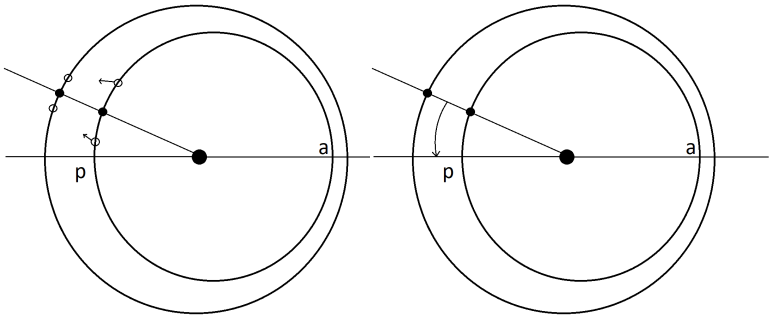

(a) (b)

Figure 2.3: a) Forces before and after conjunctions near pericenter in 2:1 MMR. b) The resulting movement of future conjunctions.

By comparing the situation right before the conjunction to right after the conjunction we see that: due to the eccentric orbit of the inner planet, the distance between the two planets is slightly smaller before the conjunction than after. This means that the force on the inner planet towards the outer planet is larger before the conjunction than after. The angular momentum of the inner planet is therefore increased which means that it migrates slightly outwards. By equation 2.3 this increases T which means slower orbital velocity. Future conjunctions will therefore occur slightly closer to the pericenter of the inner planet. So successive conjunctions pushes the location of conjunction towards pericenter. This is an example of a stable resonance. Similarly, in the model provided by figure 2.3 one can show that conjunctions occurring close to apocenter of the inner planet leads to a repulsive potential, pushing conjunctions away from apocenter.

We can think of this mean motion resonance as a potential well for the orbits with its bottom at pericenter of the inner planet. It provides a restoring force that pushes the conjunctions of the orbits closer to pericenter. This leads to a typical pendulum motion of conjunctions librating about pericenter.

2.3.2 Pendulum Model

Using equation 2.14 for $\dot{\phi}$ we can take the second derivative

$$\ddot{\phi} = j_1(\dot{n}' + \ddot{\epsilon}') + j_2(\dot{n} + \ddot{\epsilon}) + j_3\ddot{\varpi}' + j_4\ddot{\varpi} + j_5\ddot{\Omega}' + j_6\ddot{\Omega}, \tag{2.20}$$

of the resonant argument. Using Lagrange's planetary equations that relates the variation of orbital elements to the disturbing function (chapter 8 Murray & Dermott (1999) we can express this in a simpler form

$$\ddot{\phi} = -\omega_0^2 \sin\phi. \tag{2.21}$$

ω_0^2 is a parameter that depends on the orbital elements, masses, the resonant argument ϕ and the type of resonance considered (Murray & Dermott 1999). This is the equation of pendulum motion. In a resonance, the restoring force acts to push the resonant argument ϕ to a certain value.

The sign of ω_0^2 changes depending on the type of resonance and whether the considered planet is the exterior or interior in the resonance. For first order resonances ($|j_1| - |j_2| = 1$) we have for the interior planet $\omega_0^2 > 0$. By looking at equation 2.21 we see that the stable point then lies at $\phi = 0°$. Similarly, for exterior first order resonances we have $\omega_0^2 < 0$, thus changing the stable point of the pendulum motion to $\phi = 180°$. The energy of the system can be divided into kinetic and potential energy by

$$E = \frac{1}{2}\dot{\phi}^2 + 2\omega_0^2 \sin^2\frac{1}{2}\phi, \tag{2.22}$$

where the first term is the kinetic energy and the second term is the potential energy.

2.3.3 Libration Width

In this section we outline a simple method of calculating the libration in semimajor axis of two planets in a mean motion resonance. In this work I use the libration width to initialize planets on orbits.

To simplify the problem we consider the restricted three-body problem, in which a test particle on an eccentric orbit feels the disturbing force from a massive planet on a perfectly circular orbit. Both objects have $i = 0$. In Murray & Dermott (1999) the libration width

is calculated for an interior object in resonance in the restricted three-body problem. We refer to chapter 8.7 in Murray & Dermott (1999) to see the details on how this is done.

In the interior restricted three body problem, since $\dot{n}' = 0$, $\ddot{\epsilon} \approx 0$, $\dot{\epsilon}' = 0$, $\dot{\varpi}' = 0$ and $\dot{\Omega} = \dot{\Omega}' = 0$, the most important first order resonant argument and its derivatives becomes:

$$\phi = j_1\lambda' + j_2\lambda - \varpi, , \tag{2.23}$$

$$\dot{\phi} = j_1 n' + j_2 n - \dot{\varpi}, \tag{2.24}$$

$$\ddot{\phi} = j_2\dot{n} - \ddot{\varpi}. \tag{2.25}$$

We note in equation 2.22 that the oscillation amplitude is given by $\phi = 180°$ which yields $E_{max} = 2\omega_0^2$. By equating equation 2.22 with E_{max} we obtain an expression for $\dot{\phi}$,

$$\dot{\phi} \propto \cos\frac{1}{2}\phi. \tag{2.26}$$

By Lagrange's equations and an approximation of $\langle R\rangle$ we calculate $\dot{n}$, see Murray & Dermott (1999). We then relate $\dot{n}$ to $\dot{\phi}$ by: $\dot{n} = \frac{dn}{dt} = \frac{dn}{d\phi}\frac{d\phi}{dt} = \frac{dn}{d\phi}\dot{\phi}$. By combining with equation 2.26 and integrating we get an equation on the form

$$n = n_0 \pm k\cos\frac{1}{2}\phi. \tag{2.27}$$

By equations 2.3 and 2.4 we can convert this into semimajor axis by $da = -\frac{2}{3}\frac{a}{n}dn$. For the exact details on doing this in the restricted three-body problem for an inner body, see section 8.7 in Murray & Dermott (1999). The result is

$$\frac{\Delta a}{a} = \pm\left(\frac{16}{3}\frac{|C_r|}{n}e\right)^{1/2}\left(1 + \frac{1}{27j_2^2e^3}\frac{|C_r|}{n}\right)^{1/2} - \frac{2}{9j_2e}\frac{|C_r|}{n}, \tag{2.28}$$

where C_r is a constant depending on the type of resonance, that is proportional to ω_0^2. For an inner resonance $C_r < 0$ which means $\omega_0^2 > 0$. The $\pm$ represents extension of libration width on each side of the libration point.

For this work I modify this formula to work also for the outer body in MMR. This is done by considering libration about $\phi = 180°$, calculating the new resonance constant C_r' and using orbital elements of the outer body (denoted by '). I can use the exact same approach as outlined above by considering a new angle $\phi' = \phi + 180°$ and remembering that $C_r' > 0$. This leads to libration of a'

$$\frac{\Delta a'}{a'} = \frac{2}{9}\frac{1}{j_1}\frac{C_r'}{n'}\frac{1}{e'} \pm \frac{2}{3n'}\left(\frac{4}{9}\frac{1}{j_1^2}\frac{C_r'^2}{e'^2} - 12C_r'e'n'\right)^{1/2}. \tag{2.29}$$

.

2.3.4 Resonance Capture

As planets migrate in the protoplanetary disk their semimajor axis a changes. By equation 2.3 this means that the orbital period changes. For multiplanet systems the period relations can then approach resonant configurations. This means that the conjunctions of the planets approach a similar configuration to that shown in figure 2.3 and start experiencing the restoring potential. It can be shown (Murray & Dermott 1999) that in the case of convergent migration $\frac{d}{dt}|a_2 - a_1| < 0$, there is a probability that the planets capture into a mean motion resonance. The probability of capture is high for slow convergence of planets as well as for low eccentricities. In fact for significantly low eccentricity and convergence rate, capture is certain (Murray & Dermott 1999). For divergent migration $\frac{d}{dt}|a_2 - a_1| > 0$ the probability of capture is zero. Instead, in the moment the resonant configuration is crossed, eccentricity (and/or for some resonances inclination) is rapidly excited (Murray & Dermott 1999).

After a successful capture into a mean motion resonance the restoring potential keeps the periods of the planets in the given configuration. This effectively means that the planets migrate together in the resonant configuration and the resonant argument ϕ librates about either $\phi = 0°$ or $\phi = 180°$ according to equation 2.21. As shown by many works e.g. Bitsch & Kley (2010, 2011); Libert & Tsiganis (2011) planets migrating in a mean motion resonance drives rapid eccentricity and/or inclination excitation. Whether eccentricity, inclination or both are excited depends on the type of resonance. From Lagrange's equations we have to first order approximation in e and i (Murray & Dermott 1999)

$$\dot{e} \propto \frac{\partial R}{\partial \varpi}, \tag{2.30}$$

$$\dot{i} \propto \frac{\partial R}{\partial \Omega}. \tag{2.31}$$

If we consider an eccentricity resonance on the form $\phi = j_1\lambda' + j_2\lambda + j_4\varpi$ we have from equation 2.16

$$\langle R \rangle \propto e^{|j_4|}\cos\phi. \tag{2.32}$$

By equation 2.30 we then see a finite contribution to $\dot{e}$ while $\dot{i} = 0$. Similarly for a pure inclination resonance we have $\dot{e} = 0$ and finite contribution from $\dot{i}$.

2.4 Planetary Scattering

As we saw already in sections 1.2 and 2.2 the disturbing force grows dominant when two planets have a close encounter. The two-body Keplerian orbits of each planet is then significantly perturbed and the orbital trajectories change. This is the underlying principle for the scattering phase.

How close do two planets need to be in order to undergo scattering? The boundary is not simple to define since the gravitational potential gradients are smooth. However, there exist a popular empirical measure for the sphere of influence of a planet: the Hill radius R_H. R_H is the radius around a planet within which the gravitational force on a test particle is significant compared to that of the central star. In Jurić & Tremaine (2008) it is defined as

$$R_H = r \left(\frac{M}{3M_*} \right)^{\frac{1}{3}}, \tag{2.33}$$

where r is the distance between the planet and the central star. By assuming small e we take $r \approx a$ (see equation 2.1). In line with Jurić & Tremaine (2008) we take the mutual Hill radii between two planets as

$$R_M = \frac{1}{2}(R_{H,1} + R_{H,2}). \tag{2.34}$$

Chapter 3

Method

In this work I simulate systems of three Jupiter-mass planets orbiting a solar mass star. This is done numerically using the N-body integrator package Mercury6.2 (Chambers 1999). All of the planetary systems are unstable within the stopping time and feature a phase of scattering. At this point it is useful to remind ourselves of the goal of the project: **I investigate what effect mean motion resonances has on the planetary scattering phase of a multi-planet system.**
With this in mind, the simulations are split into two parts:

MMR: 3-planet systems that migrate and capture into MMR prior to the scattering phase.

NON-MMR: 3-planet systems that undergo a scattering phase without MMR as initial condition.

The difference between MMR and NON-MMR simulations, as we will see in this chapter, is that the former includes planet-disk interactions. This allows the planets to migrate and capture into MMR before the scattering starts. The NON-MMR systems are unstable by their initial conditions and feature no planet-disk interactions.

Before moving on to describe my simulations in detail I will briefly introduce the numerical integration method.

3.1 Numerical Approach

3.1.1 Mercury6.2

Mercury6.2 is a second order hybrid symplectic integrator. Most of the time it uses a symplectic integrator as described in appendix B.

The Hamiltonian is split into three parts H_A: total energy of each planet in a two-body system with the star, H_B: potential energy of each planet due to all other planets and H_C: kinetic energy of the sun due to all other planets,

$$H_A = \sum_i \left(\frac{p_i^2}{2m_i} - G\frac{m_\odot m_i}{r_{i\odot}} \right), \tag{3.1}$$

$$H_B = G\sum_i \sum_{j=i+1} \frac{m_i m_j}{r_{ij}}, \tag{3.2}$$

$$H_C = \frac{1}{2m_\odot} \left(\sum_i p_i \right)^2, \tag{3.3}$$

where the sums include all bodies except the star. Each of the split Hamiltonians are separately solvable analytically. These are called mixed-center variables because coordinates are measured in central coordinates (origin is at the star coordinates) while velocities are measured in barycentric coordinates. As shown in Chambers (1999), any quantity of the system, $q(t)$, can then be expressed as

$$q(t) = e^{\tau B/2} e^{\tau C/2} e^{\tau A} e^{\tau C/2} e^{\tau B/2} q(t-\tau), \tag{3.4}$$

in accordance with notation and method in appendix B. When planets are widely separated H_A completely dominates over H_B and H_C. Having one of the splittings dominating over the others significantly reduces the error ΔH as can be seen in appendix B and Chambers (1999).

During close encounters, as a specific r_{ij} becomes small, H_B grows dominant and thus severely increases the energy error. Therefore, the term in H_B that is responsible for the small r_{ij} is moved temporarily into H_A during the close encounter. This ensures that H_A stays dominant over both H_B and H_C and ΔH stays small. For details on how the specific term with r_{ij} responsible for the close encounter is moved into H_A, see Chambers (1999). Basically the sum in H_B is added also to H_A but modified by a factor $(1 - K(r_{ij}))$. H_B itself is similarly multiplied by a factor $K(r_{ij})$. When r_{ij} is large $K(r_{ij}) = 1$. The moving of terms is ensured by $K(r_{ij}) \to 0$ when r_{ij} becomes small.

With the addition of the extra term from H_B, the term ij in H_A becomes a three-body problem that has to be integrated numerically using standard methods. This is

done using a BS-integrator (Burlisch-Stoer). A variable time step is needed in the BS-integrator to maintain accuracy during the close encounter. The time step decreases as the objects approach each other. To control the energy error of the BS-integrator an accuracy parameter ϵ is used. It determines the maximum allowed fractional energy error.

Input Parameters

The initial parameters of a planetary system can be expressed in orbital element coordinates a, e, i, ω, Ω and M describing the instantaneous orbit of each planet fully. The coordinates and their meaning were described in section 2.1. They are given relative to the position of the central star and its reference plane. Planet orbits can also be described by standard Cartesian coordinates x, y, z and v_x, v_y, v_z, given in the reference plane of the central star. They are used for various calculations within mercury6.2, such as the migration implementation discussed in section 3.2.3.

Output Parameters

Mercury6.2 can output both orbital elements and Cartesian coordinates of each integrated body. For the output parameters there is also a choice of reference frame. I mostly use central coordinates, giving each coordinate with the origin at the central star. There is no apparent reason for choosing central coordinates over for example barycentric coordinates. As long as the analysis is consistent in using the same coordinate system, any coordinate system is equally good. However, for investigating energy conservation and angular momentum conservation, a barycentric reference frame must be used.

3.1.2 Energy conservation and optimization

The time step of the hybrid symplectic integrator is fixed for the whole system when there are no close encounters. The error that the constructed Hamiltonian H_c makes compared to the true Hamiltonian H is proportional to the time step τ, see Appendix B. Saha & Tremaine (1992) describes that an n-th order symplectic integrator has

$$\Delta H \propto \tau^n. \tag{3.5}$$

This means that our second order hybrid symplectic integrator should have an energy error proportional to τ^2, given that there are no close encounters. In this section I analyze the impact of τ on the energy- and angular momentum-error in a test integration. Clearly, smaller τ should lead to smaller errors but at the cost of long run-time. The goal is to

choose an optimal value of τ to get accurate results without too lengthy simulations. The fractional energy error is measured by

$$\Delta E = \frac{|E_0 - E(t)|}{E_0}. \tag{3.6}$$

The fractional angular momentum error is similarly defined as

$$\Delta L = \frac{|L_0 - L(t)|}{L_0}, \tag{3.7}$$

where E_0 and L_0 are the initial energy and angular momentum of the system. $E(t)$ and $L(t)$ are the current energy and angular momentum of the system.

The first constraint on τ is the period of the bodies in the simulation. If $\tau \sim T_{inner}$ the resolution of that orbit is insufficient and energy- and angular momentum errors become large. As a guiding point we adopt $\tau \leq \frac{1}{20} T_{inner}$ similar to, but more strict than Jurić & Tremaine (2008). It is important to test the energy and angular momentum conservation for both stable and unstable systems especially since the BS integrator is partly used in unstable systems. The accuracy and speed of this integrator is inherently different from the purely symplectic integrator. The systems simulated in this section therefore differs from main simulations (MMR and NON-MMR), which are all unstable. In order to achieve both very stable systems and very unstable systems for this section I modify the orbital separations and masses of the planets. Both tests uses $t_{stop} = 10^7\, yrs$ and a solar mass central star.

Stable system

The stable system has the following configuration:

	a_i [AU]	$m_{p,i}$ [$M_\odot$]
planet 1	6.2205	$3.9685 \cdot 10^{-4}$
planet 2	23.0000	$7.3233 \cdot 10^{-4}$
planet 3	70.0000	$2.8400 \cdot 10^{-4}$

Table 3.1: Stable system configuration.

According to the stability analysis provided in section 3.2.2 this system should be stable for longer than the age of the Universe.

First, I confirm that ΔE and ΔL are bounded during a simulation as predicted by a symplectic integrator. An arbitrary time step $\tau = 7.54\,\mathrm{d}$ is used. As can be seen in figure 3.1, ΔE and ΔL are bounded during the simulation.

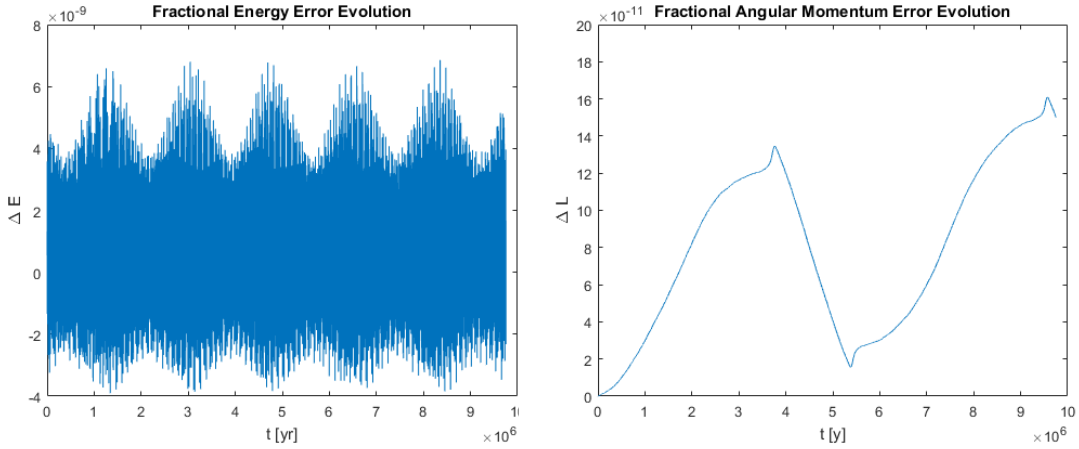

(a) ΔE evolution with simulation time. (b) ΔL evolution with simulation time.

Figure 3.1: The fractional energy and angular momentum errors, ΔE and ΔL, are plotted as functions of simulation time t. Using only the symplectic integrator both are bounded quantities.

I proceed to analyze the impact of τ on ΔE, ΔL and the real time t_r. Using the condition $\tau \leq \frac{1}{20} T_{inner} \sim 280\,d$ I take a logarithmic scale in the time step $\tau\,\epsilon\,[3, 300]$. In figure 3.2 we see that $\Delta E \propto \tau^2$ as predicted by equation 3.5. The runtime t_r decreases with larger τ as expected. ΔL on the other hand seems to decrease with larger τ. This could be due to round-off errors for small changes in ΔL in each time step.

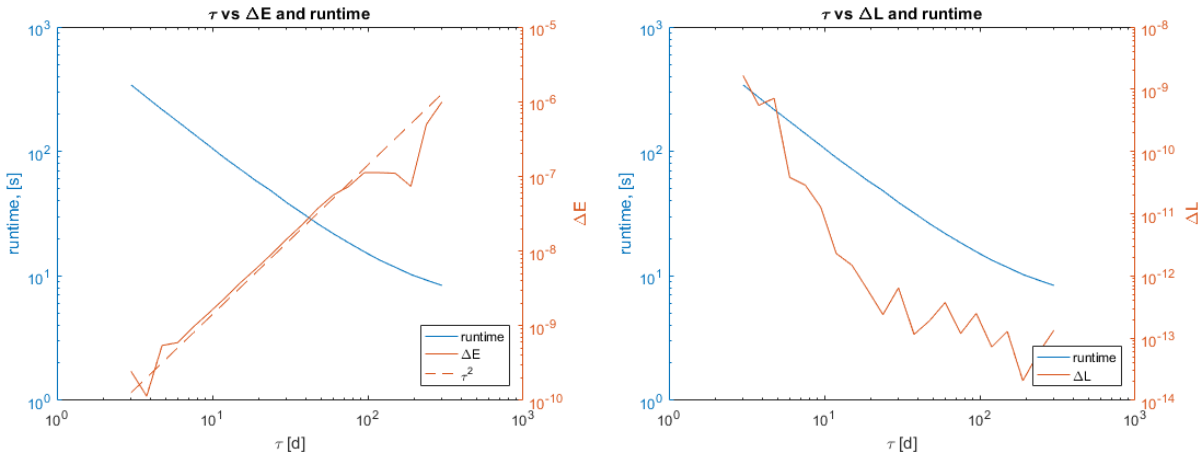

(a) ΔE and t_r as functions of τ. The dashed line represents a fitted τ^2 function.

(b) ΔL and t_r as functions of τ.

Figure 3.2: ΔE, ΔL and t_r as functions of the time step τ for a stable system without close encounters. a) shows that $\Delta E \propto \tau^2$ as was predicted.

Unstable system

According to the stability criterion in section 3.1.4 the following system is unstable within the integration time.

	a_i [AU]	$m_{p,i}$ [$M_\odot$]
planet 1	6.2205	$3.9685 \cdot 10^{-3}$
planet 2	8.0000	$7.3233 \cdot 10^{-4}$
planet 3	12.0000	$2.8400 \cdot 10^{-4}$

Table 3.2: Unstable system configuration.

In figure 3.3 we see that ΔE increases more steeply with τ for the unstable runs. In fact, $\Delta E \propto \tau^3$. This could be due to scattering of planets leading to eccentric orbits at low semimajor axis. As τ approaches T_{inner}, ΔE increases rapidly due to bad resolution at $\tau \sim T_{inner}$. The runtime t_r is slightly shorter for unstable systems but follows roughly the same trend with τ as for stable systems. This is due to planets getting ejected leading to less data in the integration process. ΔL seems to oscillate between 10^{-12} and 10^{-13} for different τ. Combined with the result for stable systems above it seems that the dependence on τ is minor and in all cases ΔL is small.

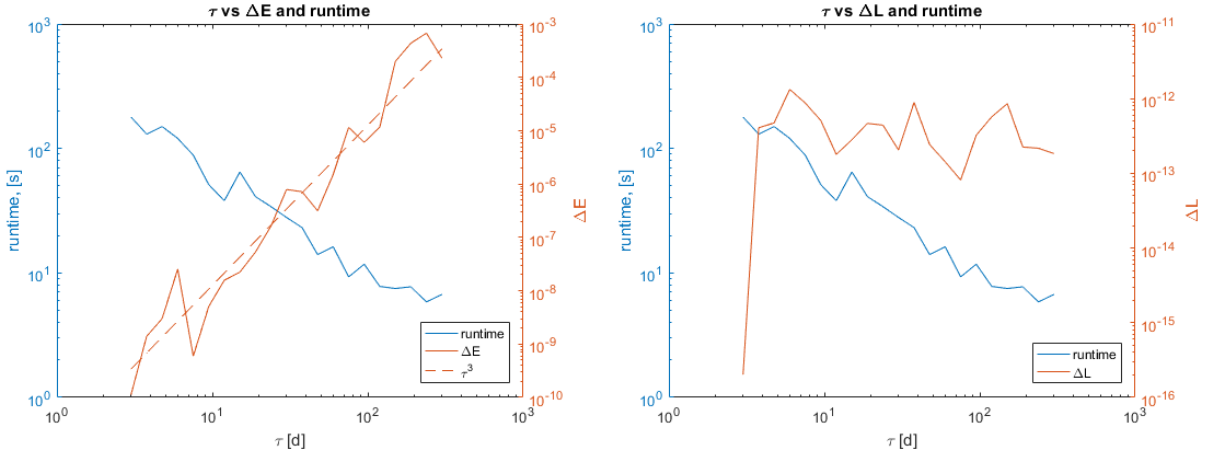

(a) ΔE and t_r as functions of τ. The dashed line represents a fitted τ^3 function.

(b) ΔL and t_r as functions of τ.

Figure 3.3: ΔE, ΔL and t_r as functions of the time step τ for an unstable system with close encounters. a) shows that $\Delta E \propto \tau^3$.

A good compromise between ΔE and t_r is found for:

$$\tau = 10\,\mathrm{d}. \tag{3.8}$$

This is a fairly typical time step which also satisfies the $\tau \leq \frac{1}{20} T_{inner}$ condition. Three different values of the BS-integrator accuracy parameter was tested with a stopping time of $t_s = 10^6$ yr: $\epsilon_1 = 10^{-10}$, $\epsilon_2 = 10^{-12}$ and $\epsilon_3 = 10^{-14}$. A smaller ϵ should result in better energy- and angular momentum conservation in the BS integrations, at the cost of longer run time. However, I do not see any trends in ΔE or ΔL and not in the run time t_r either. This can be explained by the relatively short time that the system spends in close encounters. I conclude that the contribution of ϵ to ΔE and ΔL is negligible compared to τ and take $\epsilon = 10^{-12}$.

3.2 Simulations

In this section I describe my simulations in detail. Remember, in order to investigate the effect of MMR on the scattering phase I split my simulations into two parts: MMR and NON-MMR simulations, which are explained further below. The systems consist of three Jupiter-mass planets and a solar mass star. Systems of three planets has been showed to be more unstable and chaotic than systems of two planets, e.g. Chambers et al. (1996). This is advantageous for this work since an extended planetary scattering phase is required. The masses of the three planets are equal for simplicity. This similarly affects the stability of the system. Works by e.g. Chambers et al. (1996) and Carrera et al. (2016) showed that for three-planet systems the systems of equal mass planets are more prone to dynamical instabilities. Furthermore, equal mass planets means that all should be affected equally much by the scattering phase. For example, a scattering event between a massive planet and a smaller planet with negligible mass would leave the massive planet with minor changes to its orbit. At the same time the smaller planet would be heavily affected.

All systems must be unstable and undergo scattering and subsequent relaxation before the analysis. I start by describing the stability analysis and which resonances are chosen for investigation. Then the MMR and NON-MMR simulations are explained.

3.2.1 General Parameters

$t_{stop} = 10^8$ yr
$\tau = 10$ d
$\epsilon = 10^{-12}$
$m_p = 9.5479 \cdot 10^{-4}\,\mathrm{M}_\odot$ (Jupiter mass)
$M_* = \mathrm{M}_\odot$

3.2.2 Stability Criterion and Choice of Resonances

It is important that all the simulated systems undergo significant planetary scattering. They shoud be gravitationally unstable well within the given t_{stop}. The stability analysis is based on the Hill radius R_H, defined in equation 2.33. The distance between two planetary orbits D_{ij} can be measured in units of mutual Hill radii, see equation 2.34. The minimum separation between two orbits D_{ij} depends on a_i, a_j, e_i, e_j, i_i, i_j and the orientation of the orbits in space ω_i and ω_j. For this work I consider only orbits with low initial inclination. By neglecting also the eccentricity- and argument of pericenter dependence I obtain approximate upper limits for D_{ij}. I thus simplify $D_{ij} \approx \frac{a_i - a_j}{R_M}$, where R_M is the mutual Hill radius.

In Jurić & Tremaine (2008) and Chambers et al. (1996) predictions regarding the long term stability of a planetary system are made based on statistics of numerous N-body simulations. They find that the stability of a system depends on its shortest D_{ij}, called D_{min}. In particular, the onset time of the scattering phase t_{onset} is highly dependent on the initial D_{min}, as can be seen in figure 3.4a. A small initial D_{min} results in early scattering while large D_{min} means late scattering or perhaps no scattering at all depending on t_{stop}.

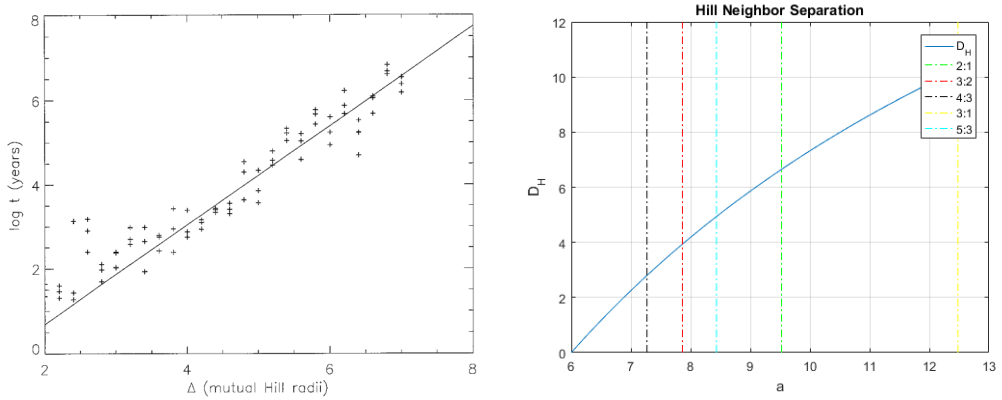

(a) (b)

Figure 3.4: a) The plot and associated simulations are taken from Chambers et al. (1996). It shows the time of the first $D_H < 1\,R_H$ close encounter plotted against mutual initial Hill separation ($\Delta = D_{min}$). All the systems were initialized with three $m_p = 10^{-7}\,\mathrm{M}_\odot$ planets equally spaced circular orbits. b) shows D_H as function of semimajor axis a measured from the innermost planet at $a_0 = 6\,AU$. In the plot are some important nominal resonant locations as dashed vertical lines.

Picking MMR

As seen in section 2.3 first order resonances ($|j_1 - j_2| = 1$) with simple fractions ($|j_1|$ & $|j_2|$ small) are the strongest and will be used in this project. For two planets, on circular orbits, at nominal resonance locations their separation measured in Hill radii D_H does not change with a. D_H is thus a unique property of each resonance. This can be seen by taking

$$D_H = \frac{a_2 - a_1}{R_M}. \tag{3.9}$$

From equation 2.33 we see that $R_H \propto r$. For circular orbits we approximate $R_H \propto a$. By equation 2.34 this means $R_M \propto a_1 + a_2$. Inserting this into equation 3.9 we obtain

$$D_H \propto \frac{a_2 - a_1}{a_1 + a_2}. \tag{3.10}$$

For objects in nominal resonance we have $\frac{a_2}{a_1} = C$ for some constant C, given by equation 2.3. Inserting this into equation 3.10 gives

$$D_H \propto \frac{C - 1}{C + 1}, \tag{3.11}$$

which is constant with a.

I require MMR with D_H such that systems are unstable well within t_{stop}. In figure 3.4b D_H is plotted as a function of a_2 given that $a_1 = 6\,AU$. In the plot the vertical lines represent the nominal resonance locations of some of the strongest MMR. Based on the arguments above and remembering that the strength of a resonance is proportional to the order of the resonance, I choose to focus on two first order resonances: 2:1 and 3:2. Since the integers j_5 and j_6 has to be even numbers, this means that the strongest MMRs should be eccentricity resonances on the form

$$\phi = 2\lambda' - \lambda - \varpi, \tag{3.12}$$

$$\phi = 3\lambda' - 2\lambda - \varpi, \tag{3.13}$$

with similar expressions for outer resonances with ϖ'.

For the 2:1 nominal MMR we have $D_H = 6.6503$.
For the 3:2 nominal MMR we have $D_H = 3.9352$.

Unfortunately, figure 3.4a cannot be used to determine t_{onset} since the Chambers et al. (1996) simulations feature $m_p = 10^{-7}\,\mathrm{M}_\odot$ planets and the same paper also showed that the $t_{onset} - D_H$ relation depends on planetary masses. However, according to Jurić & Tremaine (2008) both of these resonances are partially active meaning they will undergo planetary scattering given enough time (more about this in section 5.4). Additionally, my simulated planetary systems will obtain non-zero eccentricities during migration which further decreases system stability.

3.2.3 MMR Simulations

The MMR simulations includes planet-disk interactions. I implement a simple model of planet-disk interactions in the simulations by applying migration, eccentricity damping and inclination damping to the planets. This means that I do not explicitly simulate a protoplanetary disk. Instead I model the interactions between the disk and the planets directly through a set of accelerations, which are explained below. The goal is to migrate the three planets to approach and capture into 3:2 and 2:1 MMR chains where each planet is in MMR with its neighbor/neighbors. As the planets migrate in resonances, eccentricity (and for some resonances inclination) is excited. Eccentricity damping allows the system to stay stable in MMR until the disk is fully dissipated. The system then enters a scattering phase due to its small D_H. Therefore these simulations are with MMR as initial condition.

Implementation of Migration and Damping

To mimic the behavior of planets embedded in a gaseous disk I implement accelerations into MERCURY6.2 that drive $\dot{a}$, $\dot{e}$ and $\dot{i}$. I follow the approach of Papaloizou & Larwood (2000) and take the following accelerations into account

$$\mathbf{a_a} = -\frac{\mathbf{v}}{\tau_a}, \tag{3.14}$$

$$\mathbf{a_e} = -2\frac{(\mathbf{v}\cdot\mathbf{r})\,\mathbf{r}}{r^2\tau_e}, \tag{3.15}$$

$$\mathbf{a_i} = -2\frac{(\mathbf{v}\cdot\mathbf{k})\,\mathbf{k}}{\tau_i}. \tag{3.16}$$

Here $\mathbf{v} = (v_x, v_y, v_z)$ is the velocity vector of the considered body, $\mathbf{r} = (x, y, z)$ is the positional vector and $\mathbf{k}$ is the vector perpendicular to the reference plane. The reference plane and the orbital plane were defined in section 2.1.1 and they are separated by the inclination angle i. The coordinates (x, y, z) and (v_x, v_y, v_z) of MERCURY6.2 is written in terms of the reference plane. Therefore we simply have $\mathbf{k} = \hat{\mathbf{z}} = (0, 0, 1)$. Planets interacting with a protoplanetary disk has been showed to drive migration, eccentricity damping and inclination damping, e.g. Bitsch et al. (2013), Baruteau et al. (2014) and Goldreich & Tremaine (1980). The accelerations in equations 3.14, 3.15 and 3.14 are not directly connected to any real physical planet-disk interactions. They simply drive migration, eccentricity damping and inclination damping. For example, $\mathbf{a_a}$ provides an acceleration against the orbital velocity $\mathbf{v}$. This leads to decreased angular momentum which forces the planet inwards. At the same time it also has an effect on the eccentricity of the orbit.

All the accelerations above have dominant effects on their associated orbital element. $\mathbf{a_a}$ has dominant effect on the semimajor axis a. However, as seen above it also slightly

affects e. $\mathbf{a_e}$ has a dominant effect on e but it also slightly affects a. $\mathbf{a_i}$ acts mostly to change i but has small contributions to both a and e. Furthermore, all the accelerations depend on the instantaneous a, e and i which adds further complexity.

$$\mathbf{a}_a \rightarrow \frac{da}{dt} = f_a(a, e, i, ...), \tag{3.17}$$

$$\mathbf{a}_e \rightarrow \frac{de}{dt} = f_e(a, e, i, ...), \tag{3.18}$$

$$\mathbf{a}_i \rightarrow \frac{di}{dt} = f_i(a, e, i, ...). \tag{3.19}$$

I implemented equations 3.14, 3.15 and 3.16 into MERCURY6.2. The coordinate system is given in terms of the reference orbit plane (x, y, z) and the accelerations are thus implemented in Cartesian coordinates, using $\mathbf{v} = (v_x, v_y, v_z)$, $\mathbf{r} = (x, y, z)$ and $\mathbf{k} = (0, 0, 1)$.

Evidently $\dot{a}$, $\dot{e}$ and $\dot{i}$ are controlled by the timescale parameters τ_a, τ_e and τ_i. For example, a large τ_a leads to slow migration and vice versa. These values can be tuned and even changed over time to imitate realistic migration and damping effects as well as disk dissipation. This is not a simple task since neither migration nor damping effects are well constrained. In this project I focus mainly on obtaining MMR configurations prior to a scattering phase. τ_a, τ_e and τ_i can be used for this as explained in section 3.2.5 and 3.2.6.

Initial Conditions

In the MMR simulations both inclination and eccentricity of orbits should be small to start with, considering planetary formation in a protoplanetary disk. Following the approach of Jurić & Tremaine (2008) I use a Rayleigh distribution to draw the inclination from

$$S(x|\sigma_x) = \frac{x}{\sigma_x^2} e^{\frac{1}{2}\frac{x^2}{\sigma_x^2}}, \tag{3.20}$$

taking $\sigma_i = 5.73$ also from Jurić & Tremaine (2008). Only positive values of i are accepted. The Rayleigh distribution of inclination is a result of Gaussian spreads with the same variance and mean in the two dimensions: $i\cos\Omega$ and $i\sin\Omega$. Ω is the ascending node described in section 2.1.1. The two Gaussian distributions of $i\cos\Omega$ and $i\sin\Omega$ also results in $\Omega \sim U(0°, 360°)$. The Rayleigh distribution is successful in describing distributions of e and i in for example the asteroid belt. For simplicity I take $e = 0$ initially for all the planets. As the planets undergo secular evolution, resonant encounters, migration in resonances and scattering the eccentricities increases for each of them.

The migration of planets is always inwards in my simulations. In order to ensure reliable capture into MMR the migration and damping accelerations, equations 3.14, 3.15 and 3.16, are only applied to the two outer planets. This leaves the inner planet initially

stationary. Therefore, by initializing the planets with slightly larger separations than the nominal resonance locations, the planets can quickly migrate and capture into MMR.

The initial semimajor axis of the inner planet a_1 is fixed. The resonance in consideration, 2:1 or 3:2, is used to calculate the nominal resonance period relation by equation 2.15. Equation 2.3 is used to calculate the nominal resonance location $a_{2,nom}$. The middle planet is then initialized such that $a_2 > a_{2,nom}$. Once a_2 is obtained I repeat the same steps again to obtain the semimajor axis of the outer planet a_3 with respect to a_2. The nominal 3:2 location lies close to the nominal 5:3 location, see figure 3.4b. By taking $a_i \gg a_{i,nom}$ there is a risk of initializing the planet exterior to the 5:3 resonance. Subsequent migration can then potentially lead to capture into this resonance instead of 3:2, which I do not want. Therefore I calculate the nominal resonance location for both the 3:2 and 5:3 resonance and initialize a_i somewhere between $a_{nom}^{3:2}$ and $a_{nom}^{5:3}$, see figure 3.5. In order to start the simulations far from both resonances I initialize a_i exactly in the middle of the two.

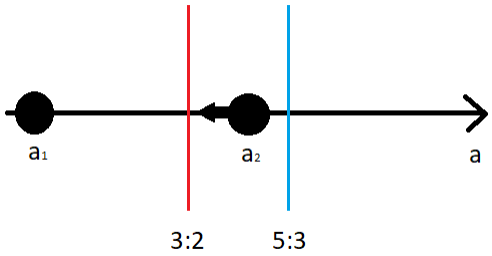

Figure 3.5: For the 3:2 resonance, given a certain a_1 I want to initialize a_2 such that $a_{nom}^{3:2} < a_2 < a_{nom}^{5:3}$. Once the simulation has started, planet 2 will then migrate into the 3:2 mean motion resonance while avoiding the 5:3.

To add another stochastic element to the simulations I initialize the semimajor axes with a Gaussian spread around the set initial values. I take $a_1(t = 0)$, $a_2(t = 0)$ and $a_3(t = 0)$ according to normal distributions $N(a|\mu, \sigma)$ with $\mu_i = a_i$. The variance is taken as half the libration width, $\sigma_i = \Delta a_i/2$, of the desired resonance. Δa_i is calculated at the nominal resonance, a_1, $a_{2,nom}$ and $a_{3,nom}$, where I expect capture to occur. The theory and the procedure of calculating the libration width is given in section 2.3.3. The 2:1 resonance is initialized such that, even with the largest possible spread in semimajor axis, $a_2(t = 0) \geq a_{2,nom}^{2:1}$ is ensured.

The orbital angles ω, Ω and M (defined in section 2.1.1) describe orientation of orbits and initial positions of planets in the orbits. They are generated randomly from a uniform distribution $U(0°, 360°)$. By using a Schwarzchild distribution, equation 3.20, to generate i, $\Omega \sim U(0°, 360°)$ is a natural choice.

MMR Capture Procedure

The three planets are initialized on orbits as described above. Migration and damping accelerations are applied only to the outer two planets. This means that first the middle planet will encounter a MMR with the inner planet. Given that the migration rate is not too large, the planets will capture in MMR. The restoring force tries to keep the planets in MMR and therefore they will continue migration inwards, now at a slower rate since the same migration acceleration now pushes two planets. This allows the outer planet to catch up and capture into the same MMR with the middle planet. A resonance chain is now complete and the three planets migrate together inwards.

3.2.4 Testing of Migration

In order to test the implementation of the migration recipes given in Papaloizou & Larwood (2000) in MERCURY6.2, I perform a semi-analytical analysis. The goal is to check that the output of MERCURY6.2 corresponds to the semi-analytical tests. From the section on perturbed orbits in the two-body problem in Murray & Dermott (1999) the perturbing acceleration is

$$\mathbf{a}_{pert} = R^*\hat{\mathbf{r}} + T^*\hat{\mathbf{t}} + N^*\hat{\mathbf{z}}_o. \tag{3.21}$$

Here $\hat{\mathbf{r}}$ is the radial unit vector of the orbit, $\hat{\mathbf{t}}$ is the tangential unit vector and $\hat{\mathbf{z}}_o$ is the normal unit vector. The vectors are in the orbital plane, which differs from the reference plane (x, y, z). R^*, T^* and N^* are the magnitudes of the radial, tangential and normal acceleration respectively.

The changes in the three considered orbital elements are given as follows (Murray & Dermott 1999)(using $\mu = n^2a^3$). They all depend in some way on the accelerations in equation 3.21 and some combination of orbital elements.

$$\frac{da}{dt} = \frac{2}{n\sqrt{1-e^2}}\left[R^* e\, sin\, f + T^*(1 + e\, cos\, f)\right]. \tag{3.22}$$

$$\frac{de}{dt} = \frac{\sqrt{1-e^2}}{na}\left[R^* sin\, f + T^*(cos\, f + cos\, E)\right]. \tag{3.23}$$

$$\frac{di}{dt} = \frac{\sqrt{1-e^2}}{na}\frac{N^* cos(\omega + f)}{1 + e\, cos\, f}. \tag{3.24}$$

E is the eccentric anomaly defined by the Kepler equation $M = E - e\, sin\, E$ (see Murray & Dermott 1999). I relate the implemented accelerations given in equations 3.14, 3.15 and 3.16 to the perturbing accelerations R^*, T^* and N^*. For the details on how this was done

I refer to Appendix C. The resulting accelerations in the orbital plane are given by

$$R^* = \dot{r}\left(\frac{1}{\tau_a} + \frac{2}{\tau_e} + \frac{2k_r^2}{\tau_i}\right) - r\dot{f}\left(\frac{2k_r k_t}{\tau_i}\right), \tag{3.25}$$

$$T^* = -r\dot{f}\left(\frac{1}{\tau_a} + \frac{2k_t^2}{\tau_i}\right) - \dot{r}\left(\frac{2k_r k_t}{\tau_i}\right), \tag{3.26}$$

$$N^* = -2\left(\frac{\dot{r}k_r}{\tau_i} + \frac{r\dot{f}k_t}{\tau_i}\right)k_z, \tag{3.27}$$

with k_r, k_t and k_z according to equation 7.13 in Appendix C.

Comparing to Mercury6.2 Output

The equations for R^*, T^* and N^* (3.25, 3.26 and 3.27) are used to calculate $\frac{da}{dt}$, $\frac{de}{dt}$ and $\frac{di}{dt}$ (3.22, 3.23 and 3.24). The resulting expressions are complex functions of the exact positions in the orbit f and E, which are both proportional to M. To simplify the problem I average the changes $\frac{da}{dt}$, $\frac{de}{dt}$ and $\frac{di}{dt}$ over each orbit. For details on how this was done see appendix C. The resulting averaged evolution of the orbital elements is

$$\langle\dot{a}\rangle = f_a(a, e, i, \omega, \tau_a, \tau_e, \tau_i), \tag{3.28}$$

$$\langle\dot{e}\rangle = f_e(e, i, \omega, \tau_a, \tau_e, \tau_i), \tag{3.29}$$

$$\langle\dot{i}\rangle = f_i(e, i, \omega, \tau_i), \tag{3.30}$$

where f_a, f_e and f_i are some complex functions of the variables stated in the respective equation above. The evolution of a, e and i now depends on some orbital elements and the planet-disk interaction parameters τ_a, τ_e and τ_i.

Equations 3.28, 3.29 and 3.30 form a system of differential equations that has to be solved simultaneously for $a(t)$, $e(t)$ and $i(t)$.

$$\begin{bmatrix}\dot{a}(t)\\ \dot{e}(t)\\ \dot{i}(t)\end{bmatrix} = \begin{bmatrix}\langle\dot{a}\rangle\\ \langle\dot{e}\rangle\\ \langle\dot{i}\rangle\end{bmatrix} \tag{3.31}$$

This system is complex and no analytical solution exists. It is solved using the built-in numerical differential equation solver NDSOLVER in MATHEMATICA. This routine utilizes a variety of methods including "Adams", "BDF" (implicit backwards differentiation formulas) and "Runge Kutta") depending on the type of differential equation. The resulting solutions $a(t)$, $e(t)$ and $i(t)$ are compared with the output of test simulations made in MERCURY6.2, using the same damping rates τ_a, τ_e and τ_i.

Figures 3.6 and 3.7 show a comparison between the MERCURY6.2 migration output and the semi-analytical orbital averaged evolution of $a(t)$, $e(t)$ and $i(t)$. A system of one

planet M_J around a star $M_\odot$ was considered for simplicity. For figure 3.6 the system was initialized with $i = 0$ and no inclination damping. This means $i(t) = 0$ always. The system of differential equations 3.31 is then simplified to only $\dot{a}(t)$ and $\dot{e}(t)$. For figure 3.7 the system was similarly initialized with $e = 0$, and no eccentricity damping. The system of differential equations 3.31 is then simplified to only $\dot{a}(t)$ and $\dot{i}(t)$.

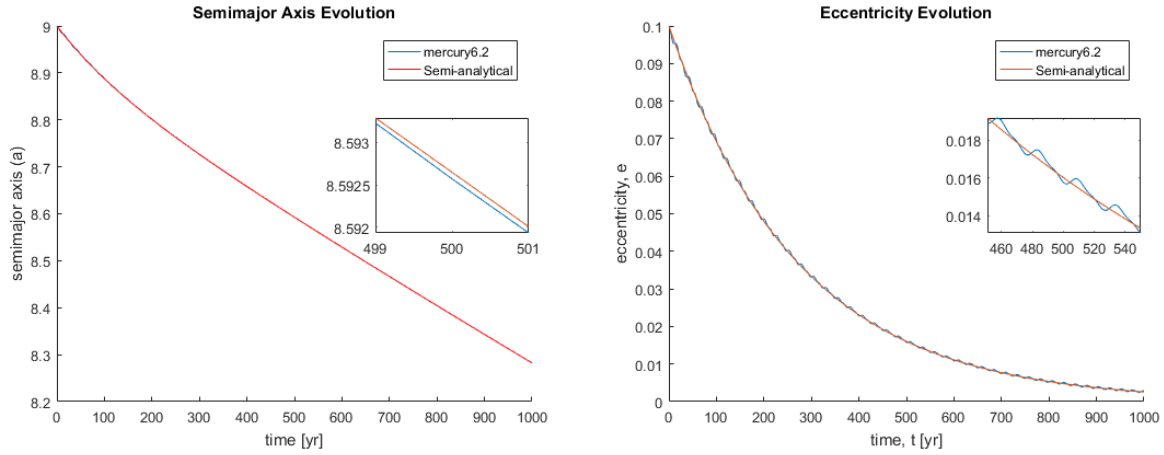

(a) (b)

Figure 3.6: a) shows the evolution $a(t)$ calculated by equation 3.31 for the simplified system (with $i = 0$ and $\tau_i \to \infty$) in red. The blue line is the MERCURY6.2 output for the same system. b) shows the evolution $e(t)$ calculated by equation 3.31 for the simplified system (with $i = 0$ and $\tau_i \to \infty$) in red. The blue line is the MERCURY6.2 output for the same system.

Figures 3.6 and 3.7 shows that the migration implementation in MERCURY6.2 is very accurate. Save for the orbit period oscillations that were removed by averaging in the semi-analytic calculations, the MERCURY6.2 simulations follows the semi-analytic evolution nearly perfectly.

3.2.5 Migration and Damping Decay

Protoplanetary disks around young stars are slowly accreted to the star and dissipated due to radiation from the star. The density of disk material decreases with time and therefore the migration, eccentricity- and inclination damping are all expected to fall off with time. I achieve this by increasing τ_a, τ_e and τ_i exponentially with time. For τ_a I introduce

$$\tau_a = C_1 e^{C_2 t/r}, \tag{3.32}$$

where t is the time from simulation start, r is the distance from the planet to the central star and C_1 and C_2 are constants. C_1 gives the initial value of τ_a and thus the initial

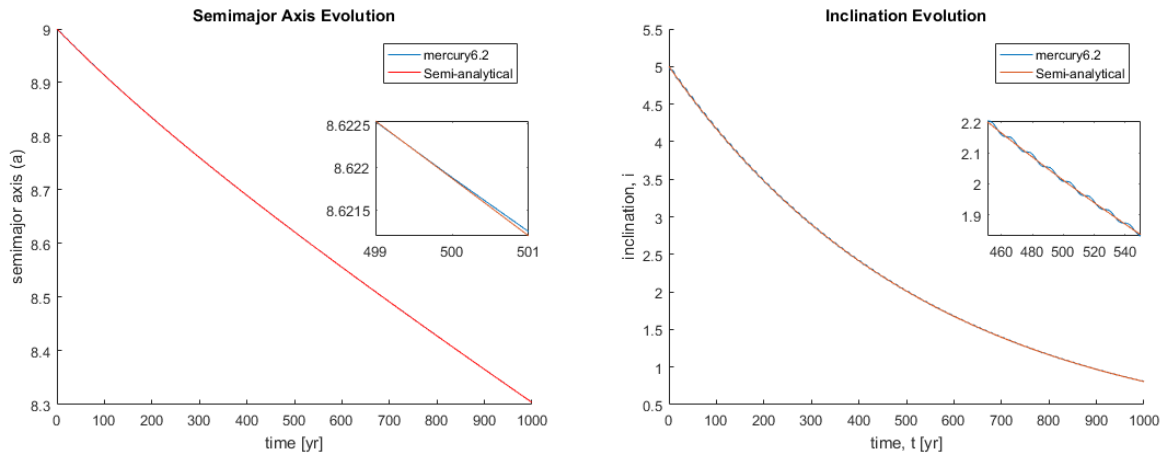

(a) (b)

Figure 3.7: a) shows the evolution $a(t)$ calculated by equation 3.31 for the simplified system (with $e = 0$ and $\tau_e \to \infty$) in red. The blue line is the MERCURY6.2 output for the same system. b) shows the evolution $i(t)$ calculated by equation 3.31 for the simplified system (with $e = 0$ and $\tau_e \to \infty$) in red. The blue line is the MERCURY6.2 output for the same system.

migration rate. C_2 determines the rate at which τ_a increases with t, thus the rate at which migration slows down. Through extensive testing I find that $C_2 = 10^{-6}\, d^{-1}$ results in planetary migration becoming negligible roughly at $t \sim 10^5\, yr$. I take this as an estimate of the disk dissipation time, t_{disk}. In Haisch et al. (2001) they find that disk lifetimes can vary between $0.3 - 30\,\mathrm{Myr}$. Given that, in these simulations the three giant planets are already fully formed when the simulations start, my disk dissipation time t_{disk} is consistent with their work. The factor $\frac{1}{r}$ in equation 3.32 was introduced to make planets at larger a have their migration rate decrease slower. This causes the outer planets to migrate for longer times and distances which allows them to catch up to their inner neighbor more reliably. In addition, equation 7.30 in the Appendix C shows that the migration rate is proportional to the semimajor axis. Both of these effects causes the migration rate and thus t_{disk} to increase toward larger semimajor axes.

For eccentricity damping I use the K-prescription, e.g. Libert & Tsiganis (2011) and (Sotiriadis et al. 2017),

$$\frac{\dot{e}}{e} = -K_e \left| \frac{\dot{a}}{a} \right|, \tag{3.33}$$

with $K_e \,\epsilon\, [1, 100]$ (Sotiriadis et al. 2017). In a similar manner I also take

$$\frac{\dot{i}}{i} = -K_i \left| \frac{\dot{a}}{a} \right|. \tag{3.34}$$

This means that the damping of eccentricity $\dot{e}$ and inclination $\dot{i}$ is proportional to the migration rate $\dot{a}$. For rapid migration (either inwards or outwards) the damping of eccentricity

and inclination is also rapid. The rate of damping depends heavily on the parameters K_e and K_i. From Papaloizou & Larwood (2000) I take the migration timescale to be defined by

$$\frac{\dot{a}}{a} = \frac{da/dt}{a} = -\frac{1}{\tau_a}, \tag{3.35}$$

with corresponding results for $\frac{\dot{e}}{e}$ and $\frac{\dot{i}}{i}$. In Papaloizou & Larwood (2000) they used $\frac{dJ/dt}{J} = -\frac{1}{\tau_a}$ where J is the angular momentum of the orbit. For a Keplerian orbit this is equivalent with equation 3.35. Using equations 3.33 and 3.34 with 3.35, the damping timescales of eccentricity and inclination are described by the K-parameter:

$$\tau_e = \frac{\tau_a}{K_e}, \tag{3.36}$$

$$\tau_i = \frac{\tau_a}{K_i}. \tag{3.37}$$

We see that large K-values leads to small timescales τ which means rapid damping. For first order resonances, inclination resonances and thus inclination excitation is relatively weak. As seen in works by eg. Libert & Tsiganis (2011) inclination resonances and subsequent inclination excitation can be triggered in a resonant planetary system if eccentricity damping is low enough that eccentricities reach large values (more on this in section 5.4). However, for this work I focus on the eccentricity damping which is more important for the stability of a system. Thus we take a fixed value $K_i = 5$ for the inclination damping.

3.2.6 Fine-Tuning of Migration

The migration and damping rate of planets in a protoplanetary disk is now characterized by four parameters: $C_1\,[d^{-1}]$, $C_2\,[d^{-1}]$, K_e and K_i. I have already fixed C_2 and K_i. In this section I outline my method of picking values of C_1 and K_e.

In section 2.3.4 we saw that eccentricity (and sometimes inclination) is excited during migration in resonance. The amount of excitation depends on the migration rate which is given by C_1. The damping of eccentricity enforced by the protoplanetary disk counters the excitation and keeps the eccentricity of involved planets at some equilibrium value. According to Sotiriadis et al. (2017), I can take $K_e\,\epsilon\,[1, 100]$. Since K_e is currently not well determined, the eccentricity damping depends strongly on what value I choose.

If K_e is low the eccentricity of the planets can grow large during the disk phase, which potentially leads to orbital crossing. As seen in section 1.2 this results in dynamical instabilities and scattering. If a system begins scattering before the disk has fully dissipated, the planet-disk interactions ($\dot{e}$, $\dot{i}$ and $\dot{a}$) directly affects the scattering phase. For a robust analysis this must be avoided. Similarly if K_e is too large it forces the eccentricity of

the planets to zero. A system in a stable mean motion resonance coupled with very low eccentricity can stay stable for very long times. However, as I want to test the effect of MMR on the scattering phase, the systems must go unstable at some point before t_{stop}.

C_1 determines the initial rate of migration. If C_1 is large then τ_a will be large and migration will be slow, and vice versa. Through the K-prescription τ_a also has direct effect on the eccentricity- and inclination damping, see equations 3.36 and 3.37. We saw in section 2.3.4 that capture probability increases with slow migration. Therefore τ_a is bounded from below where migration is so fast that probability of capture is zero. I can estimate this boundary by making use of the libration width. In Murray & Dermott (1999) they derive an approximate expression for the period of libration in the restricted three-body problem. The relation is valid for small amplitude oscillations about the stable ϕ. Without derivation we simply state the relation here

$$T_{lib} = \frac{2\pi}{\omega_0}, \tag{3.38}$$

where ω_0 is the same parameter as given in the pendulum equation 2.21. It depends on the type of resonance, the orbital elements and ϕ. I define the crossing time t_c as the time it takes for the test particle in the restricted three-body problem to cross a resonance with the massive body:

$$t_c = \frac{|\Delta a_+| + |\Delta a_-|}{\Delta \dot{a}}, \tag{3.39}$$

where Δa is given by equations 2.28 and 2.29. The $+$ and $-$ indicates what sign to use from the $\pm$. $\Delta \dot{a}$ is the relative migration rate between the two involved planets. For this work, I assume that the inner body is not migrating $\dot{a} = 0$ and thus $\Delta \dot{a} = \dot{a}'$. This approach allows for quick and simple capture into MMR although its physical interpretation may be unrealistic. By approximating $e = i = 0$ I have $\dot{a}'$ by equation 7.30 in Appendix C. For simplicity and since these are all approximate relations we also take $|\Delta a_+| + |\Delta a_-| \approx 2|\Delta a|$. Combining these leads to

$$t_c = \frac{\tau_a |\Delta a|}{a'}. \tag{3.40}$$

For high probability of smooth capture into mean motion resonance I need $t_c \leq T_{lib}$. This results in

$$\tau_a \leq \frac{2\pi}{\omega_0} \frac{a'}{|\Delta a|}. \tag{3.41}$$

I take this to be an approximate the lower limit of C_1. Note that given an initial value of C_1, τ_a will increase due to C_2 as the first resonance is approached. As can be seen in equation 3.41 this limit grows larger with a' and is thus not a constant property of a resonance.

K_e - C_1 Pairs

For the MMR simulations I need the systems to undergo a planetary scattering phase within t_{stop}. At the same time I also require the systems to capture and stay in stable MMR until the disk dispersion time t_{disk}. Systems that go unstable and scatter already during the disk phase have their scattering phase affected by the migration and damping effects. This means that $\dot{a}$, $\dot{e}$ and $\dot{i}$ will influence the relaxed system which must be avoided. I call the fraction of systems meeting the mentioned requirements f_{succ}. So f_{succ} describes the fraction of the total amount of systems that undergo scattering at some point between t_{disk} and t_{stop}. Below the parameters K_e and C_1 are chosen such that f_{succ} is maximized. Based on the limits for C_1 and K_e I test the following logarithmic ranges:

2:1	**3:2**
$C_1 \in [10^{6.4}, 10^{8.8}]\,\mathrm{d}^{-1}$	$C_1 \in [10^{6.2}, 10^{8.6}]\,\mathrm{d}^{-1}$
$K_e \in [10^0, 10^2]$	$K_e \in [10^0, 10^2]$

Table 3.3: K_e and C_1 ranges tested.

For each value of K_e, C_1 and each resonance, I perform ten simulations with the usual stopping time t_{stop}. The initial semimajor axes are as follows (including the gaussian spread described in section 3.2.3):

	$a_i^{2:1}$ [AU]	$a_i^{3:2}$ [AU]
planet 1	7.0	7.0
planet 2	11.5	9.5
planet 3	19.0	13.0

Table 3.4: Initial semimajor axes for 2:1 and 3:2 MMR respectively.

To determine whether a system is in resonance or has started the scattering, the period ratio T_2/T_1 is measured for each neighboring planet pair during the simulations. A planet pair is considered in resonance if T_2/T_1 corresponds to the given nominal MMR within some libration amplitude $\Delta\frac{T_{i+1}}{T_i}$. A system is successful if both planet pairs are in resonance at t_{disk} but not at t_{stop}. The limit of $\Delta\frac{T_{i+1}}{T_i}$ can be calculated using the theory in section 2.3.3 about libration width. However, these estimates proved to be too accepting when applied to simulations. Instead, by analyzing many resonant simulations, I provide approximate empirical limits for $\Delta\frac{T_{i+1}}{T_i}$. At the given initial separation a_1, a_2 and a_3 and the migration rates given by C_1 and K_e above the following are enough to describe the simulations:

2:1 $\Delta\frac{T_{i+1}}{T_i} = 0.15$
3:2 $\Delta\frac{T_{i+1}}{T_i} = 0.06,$

The two nominal MMRs have different initial separations a_1, a_2 and a_3 and thus the migration decay is slightly different. Empirically, I find different disk dissipation times t_{disk}:

2:1: $t_{disk} = 2 \cdot 10^5\,\mathrm{yr},$
3:2: $t_{disk} = 10^5\,\mathrm{yr}.$

The $K_e - C_1$ testing result can be seen in figure 3.8. The figures show the logarithmic grid in K_e and C_1 for the 2:1 and 3:2 MMR respectively. Each grid point corresponds to ten simulations of planet systems. The underlying number grid shows the number of systems that were in MMR at $t = 10^5\,\mathrm{yr}$ for each $K_e - C_1$ pair (Note that this corresponds to t_{disk} only for the 3:2 MMR). The colour bar shows the fraction of these $f_{scattered}$ that were unstable and underwent a planetary scattering phase within t_{stop}.

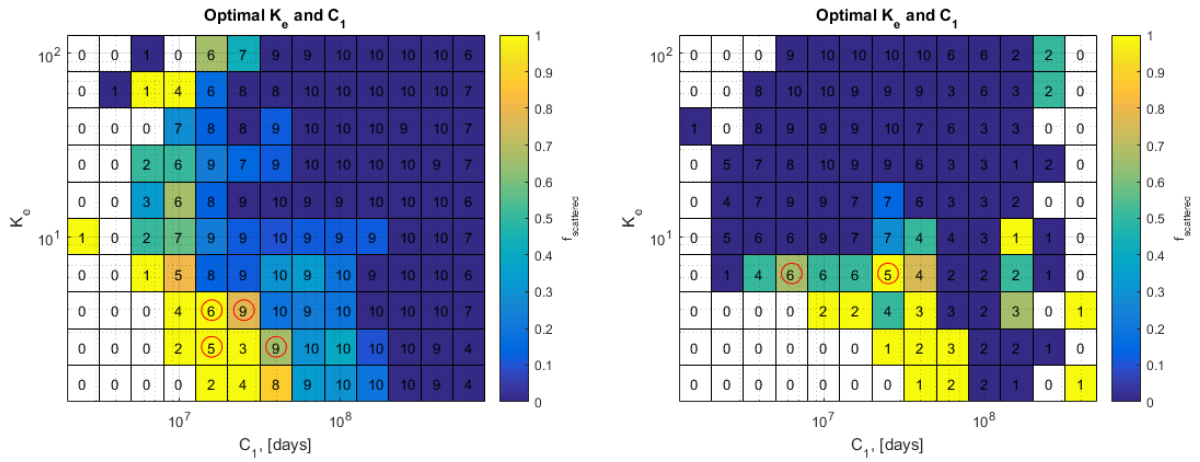

(a) (b)

Figure 3.8: Grid of tested $K_e - C_1$ pairs. Each grid point represents ten simulations. The underlying numbers show the number of simulations that were in MMR at $t = 10^5\,\mathrm{yr}$. The colour bar shows the fraction of these $f_{scattered}$ that went unstable within t_{stop}. Red circles represents the $K_e - C_1$ pairs that were picked for this project. a) 2:1 resonance b) 3:2 resonance

The fraction of successful systems f_{succ} is given by converting the grid numbers into fractions of ten and multiplying by the colourbar fraction. So for as many successful systems as possible I want large grid numbers and colours close to yellow. f_{succ} for the 2:1 MMR in figure 3.8a is slightly misleading since $t_{disk} = 2 \cdot 10^5\,\mathrm{yr}$ for 2:1. In figure 3.8 I find that low K_e leads to many systems going unstable within or even before t_{stop}. This confirms that low K_e leads to large τ_e (slow eccentricity damping) and large equilibrium

eccentricity. τ_e is by definition proportional to τ_a which is dependent on C_1. Small C_1 implies small τ_e and thus rapid eccentricity damping and more stable systems. However, small C_1 also results in rapid migration which excites eccentricity effectively. The effect of C_1 is ambiguous where both large and small C_1 leads to more systems going unstable before t_{disk}. However, in general it seems that systems with small C_1 that survive until t_{disk} have enough eccentricity to go unstable relatively quickly after. Systems with large C_1 that survive until t_{disk} have too low eccentricity and stay stable until t_{stop}. Furthermore, for very small C_1 migration is too rapid for MMR capture, as discussed in both this section and section 2.3.4. For very large C_1 migration is too slow meaning that the planets never reach the nominal MMR location. These two effects provide hard vertical boundaries in figures 3.8a and 3.8b.

For the 2:1 MMR there are a few $K_e - C_1$ pairs that have fairly high f_{succ}. I choose four grid points, marked in figure 3.8a, that span a small region of fairly successful simulations. The pairs are named after their simulation number and are showed in table 3.5.

2:1	K_e	$C_1\,[\mathrm{d}^{-1}]$	f_{succ}
K2C5	$10^{0.4}$	$10^{7.2}$	0.5
K2C7	$10^{0.4}$	$10^{7.6}$	0.63
K3C5	$10^{0.6}$	$10^{7.2}$	0.6
K3C6	$10^{0.6}$	$10^{7.4}$	0.72

Table 3.5: Chosen $K_e - C_1$ pairs for the 2:1 MMR.

For the 3:2 MMR the success rates are generally much lower. Because of the initially tight configuration, the 3:2 systems are pushed to very small semimajor axis during migration. The 3:2 planets thus have smaller orbital periods than the 2:1 planets and evolve quicker with time. This effect combined with tight orbital spacing means systems tend to go unstable before t_{disk}. I have identified two $K_e - C_1$ pairs that provide reasonable f_{succ}, marked in figure 3.8b and showed in table 3.6

3:2	K_e	$C_1\,[\mathrm{d}^{-1}]$	f_{succ}
K4C4	$10^{0.8}$	$10^{6.8}$	0.36
K4C7	$10^{0.8}$	$10^{7.4}$	0.5

Table 3.6: Chosen $K_e - C_1$ pairs for the 3:2 MMR.

Number of Simulations

For reasons that will become clear in section 3.3.2, I require a number of simulated planets comparable to the number of detected giant exoplanets. We create a subset of planets from `exoplanets.org` using the following restrictions:

In accordance with Winn & Fabrycky (2015) I take giant planets as $M > 0.1 M_J$. Planets with very small semimajor axis also have small Hill spheres, see equation 2.33. If the Hill sphere of a planet is comparable to its radius, close encounters in this region predominately leads to collisions rather than scattering. Petrovich et al. (2014) argue that such collisions most likely lead to a single merged planet with low eccentricity and low inclination. Such interactions cannot be responsible for the high eccentricity high inclination distribution of observed exoplanets. Therefore, if planetary scattering is responsible for the observed eccentricity/inclination distribution then it must occur at larger semimajor axis. In Petrovich et al. (2014) they take $a > 0.45\,AU$ for scattering to be dominant over collisions. I adopt this value as a minimum semimajor axis for giant planets. Furthermore I require that the host star is a single star in the mass range $M_* \in [0.5, 2]\,\mathrm{M}_\odot$.

Using these restrictions we find (February 2018) $N_p = 289$ (number of exoplanets that meets the above restrictions). It should be noted that a large majority of these exoplanets were detected by the RV method and suffer from any corresponding bias effects. I aim to create a simulated sample of $N_p \sim 300$ for both the 2:1 and 3:2 resonance. The fraction of surviving planets per system after the scattering phase is, for my simulations, roughly $f_{surviving} \sim 0.5$. This means that for the systems that successfully stay in MMR until t_{disk} and then scatter within t_{stop}, roughly half of the planets remain in the system after the scattering phase. Therefore that I need $N_s \sim 200$ successful systems to produce $N_p \sim 300$. Based on f_{succ} the number of simulations needed to create the sample of $N_p \sim 300$ is roughly:

2:1 $N_s \sim 400$,
3:2 $N_s \sim 560$.

The initial semimajor axis of the MMR simulations are given in the same way as for the $K_e - C_1$ plots, table 3.4.

3.2.7 NON-MMR Simulations

NON-MMR simulations are without planet-disk interactions. They feature no migration, no eccentricity damping and no inclination damping. It is very unlikely that resonance capture occurs without planetary migration and thus these simulations are without MMR as initial condition. The most important consideration for these simulations is dynamical instability within the simulation time, which has already been analyzed in section 3.2.2. Another important consideration is making sure that the only difference between the MMR and NON-MMR simulations is whether systems are in MMR initially or not. In particular I want to get rid of any bias due to initial orbital elements. The initial orbital elements $a(t = 0)$, $e(t = 0)$ and $i(t = 0)$ affect the scattering phase in some way. This is because the total energy E_{tot} and total angular momentum L_{tot} of a multi-planet system are functions

of a, e and i (E_{tot} of a multi-planet system is only weakly dependent on e and i). E_{tot} and L_{tot} are quantities that are conserved, even through the chaotic scattering phase, and thus the initial $a(t = 0)$, $e(t = 0)$ and $i(t = 0)$ leave imprints on the system even after relaxation.

For this reason, I initialize the planetary orbits of NON-MMR simulations with similar orbital elements that were found in the MMR simulations at t_{disk}. I expect the successful systems of the MMR simulations to be in their respective resonant configuration at t_{disk}. At t_{disk} in the MMR simulations I create empirical cumulative distributions of a, e and i for all three planets individually. The initial $a(t = 0)$, $e(t = 0)$ and $i(t = 0)$ for NON-MMR simulations are drawn from these cumulative distributions individually for all three planets. This provides $a_i(t = 0)$ close to the nominal 2:1 and 3:2 resonance for all planets in the system. Also $e(t = 0)$ and $i(t = 0)$ are close to the values obtained for systems in MMR. However, due to the rest of the orbital elements being randomized according to $U(0°, 360°)$, it is very unlikely that any of these systems are in MMR. The only difference between the MMR and NON-MMR systems is now initial MMR.

Provided enough eccentricity, the nominal resonance locations (without MMR) are unstable for $M_* = M_\odot$ and $M_p = M_J$ as seen in section 3.2.2. Again I want the number of planets to be $N_p \sim 300$. $f_{surviving} \sim 0.5$ gives the number of systems $N_s \sim 200$.

NON-MMR-CIRCULAR Simulations

As a subset of the NON-MMR simulations I make a NON-MMR-CIRCULAR set of simulations, using circular orbits and small inclinations. For these I draw semimajor axes in the same way as for the regular NON-MMR, from t_{disk} of the MMR simulations. For eccentricities I take $e(t = 0) = 0$ and for inclinations $i(t = 0)$ I draw small numbers from the Rayleigh distribution, equation 3.20. The point of this is to compare to the standard NON-MMR simulations, both to test the effect of initial eccentricity and inclination, but also to compare to other works as described later in section 3.3.3.

3.3 Analysis

For each $K_e - C_1$ pair, successful systems of the MMR simulations are singled out and analyzed while unsuccessful systems are discarded. Each $K_e - C_1$ pair of the MMR simulations has a corresponding set of NON-MMR simulations with appropriate initial conditions.

3.3.1 Comparisons

The goal of this thesis is to investigate and compare the scattering phase between systems initially in MMR and systems initially not in MMR. To do this, a few parameters of the scattering phase were chosen for analysis and comparisons.

Eccentricity and Inclination

Eccentricity of exoplanets is relatively straightforward to measure from RV observations to reasonable accuracy. Inclinations, while more difficult to obtain accurately, are also observable. The excited eccentricity and inclination distributions of observed exoplanets, compared to the solar system, is what the planet-planet scattering theory tries to explain. It is therefore necessary to analyze eccentricity and inclination. As discussed in the introduction, eccentricity and inclination are highly affected by planetary scattering. Jurić & Tremaine (2008) showed that the final eccentricity distribution of a planetary system reflects the amount of scattering it underwent. I analyze the cumulative distribution of eccentricity and inclination of surviving planets at the end of simulations when systems are relaxed.

Semimajor axis

Semimajor axes of surviving planets after a phase of planetary scattering is highly dependent on their initial semimajor axes. Eccentricity- and inclination are much less dependent on the initial eccentricity and inclination. Despite planetary migration, semimajor axes of planetary systems just before a scattering phase varies heavily due to varying planet- and stellar mass. For this reason, semimajor axis is rarely used when analyzing planetary scattering. However, as a scale-independent parameter, the ratio of semimajor axes of surviving planets is analyzed. Most unstable systems relax by ejecting one or two (in rare cases zero or all three) planets. For two-planet survivor systems I compare the ratio of semimajor axes between MMR- and non-MMR systems.

Minimum Pericenter

During the scattering phase planets rapidly vary their orbital elements. The pericenter of a giant planet orbit $r_{min} = a(1-e)$ thus scans a large range of semimajor axis. As discussed in Carrera et al. (2016) this has a major effect on the allowed range of semimajor axes of small planets. Systems of small planets that have giant planet excursions tend to scatter and dissipate. I analyze the cumulative distribution of the smallest measured pericenter of

any planet in all systems.

Scattering Phase Timescales

The onset time t_{onset} of the scattering phase is non-trivial to measure. I test three different methods. The first method uses excursions in semimajor axis, by the criterion $\frac{\Delta a}{a} \geq 10\,\%$. I can only measure the orbital elements in each output time step Δt and therefore each onset time is rounded up to the nearest Δt. Despite this drawback it is perhaps the most robust method. The second method uses the built-in close encounter analysis tool CLOSE6.FOR in MERCURY6.2. I take $3\,R_H$ (Hill radii) as the limit for a close encounter and record every time two planets come closer than this. As a third method I compute the first time during simulation that the pericenter of an outer planet meets the apocenter of an inner planet, $r_{max} \geq r'_{min}$. This is a rough estimation of the orbit crossing time.

Using the close encounter analysis tool CLOSE6.FOR the best precision in t_{onset} is obtained. This is because it utilizes the integration time step $\tau = 10\,\mathrm{d}$ while the other two methods uses the output time step $\Delta t = 10^4\,\mathrm{yr}$. However, for the MMR simulations some systems can potentially stay in MMR even after having close encounters, due to the strong restoring force. Therefore CLOSE6.FOR is inaccurate in determining t_{onset}. For reasons outlined in the Discussion, section 5.1.2, the orbital crossing condition does not accurately predict t_{onset} for the MMR simulations. For consistency $\frac{\Delta a}{a} \geq 10\,\%$ is used to determine t_{onset} for both MMR and non-MMR simulations. I analyze the cumulative distribution t_{onset} for all systems.

The duration of the scattering phase is measured by $t_{dur} = t_{finish} - t_{onset}$. Since t_{onset} is measured by the $\frac{\Delta a}{a} \geq 10\,\%$ method, I use the same method for t_{finish}.

Collisions

Closely separated systems have increased probabilities for collisions between planets, as opposed to ejections. As can be seen in e.g. Petrovich et al. (2014) the rate of collisions relative to ejections for a given planet increases for smaller semimajor axis and larger planetary radius. Ford et al. (2001) showed that collisional evolution, in contrast to ejections, leads to low eccentricity daughter planets. I analyze differences in average number of collisions per simulation between MMR and NON-MMR simulations.

3.3.2 Hypothesis testing

I perform hypothesis tests to investigate whether two cumulative distribution functions (CDF) are consistent with being drawn from the same underlying distribution. A test statistic D must be defined and sampled under the null hypothesis H_0 that the two CDFs belong to the same probability distribution function (PDF). With a defined distribution of Ds under H_0 we can measure the test statistic of our observed samples D_{obs}. The probability p that a randomly drawn D from the distribution is equally or more extreme than D_{obs}, under the assumption that H_0 is true, should be as small as possible for us to be able to reject H_0. As a limit for whether H_0 can be rejected or not a significance level α is used. If $p \leq \alpha$ H_0 is rejected.

The p-value related to comparing two distributions can be dependent on the sample size of the two distributions. The effect on p depends on how the sample size affects the test statistic D and the distributions themselves. Generally, distributions get more well defined with less spread as sample size increases. Any differences between the distributions get more pronounced, which means that if H_0 is true (the distributions are the same) p will increase. However, if H_0 is false p decreases with sample size. This is the reason for choosing a similar sample size of simulated planets as the observed sample of giant exoplanets, see section 3.2.5. Without comparable sample sizes a p-value can be meaningless.

For this work I have used two hypothesis tests with different test statistic D for comparing CDFs: Two-sample Kolmogorov-Smirnov (K-S test) and two-sample Anderson-Darling (A-D test). Both of these utilize test statistics that measure differences between two CDFs. For details on how they work I provide a short summary in Appendix D.

Bonferroni Correction

The more hypothesis tests with different observed test statistic D_{obs} we perform the more likely it is to eventually reject an H_0 even though H_0 is true. To avoid this a Bonferroni correction is used. Each individual hypothesis test performed is tested using a modified significance level $\alpha^* = \frac{\alpha}{m}$, where α is the desired significance level of the whole experiment and m is the number of individual tests. In order to be called individual tests they have to be somewhat uncorrelated. For example the final e and minimum a_{per} during a simulation should have only very small correlation at most. On the other hand e and i are significantly correlated.

For this work I compare MMR simulations with NON-MMR simulations for all six $K_e - C_1$ pairs. Furthermore, as can be seen in the next section, I compare NON-MMR to NON-MMR-CIRCULAR for $K4C4$ and $K4C7$. I perform hypothesis tests for e, i, a_{per}, $\frac{a_i}{a_j}$, t_{onset} and t_{dur}. That makes a total of $m = 48$ different D_{obs}.

3.3.3 Comparing to Other Works

There are several popular works on planetary scattering, most of which focus only on the scattering phase whithout MMR, eg. Jurić & Tremaine (2008), Chambers et al. (1996) and Chatterjee et al. (2008). Due to planet-disk interactions discussed in section 1.3, planetary systems without MMR are believed to have low eccentricity and inclination early on, before planets grow large enough or migrate close enough for scattering to start. Many previous works on planetary scattering therefore have their planets initialized with low eccentricity and inclination (Note that this is not the case in Jurić & Tremaine (2008)). This is in contrast to my work. Since eccentricity and inclination are excited during migration in MMR, the NON-MMR simulations are initialized with significant eccentricity and inclination.

In order to better make comparisons to existing work I test additional systems, with $e(t = 0) = 0$ and $i(t = 0)$ drawn from a Rayleigh distribution, equation 3.20, for all three planets. The initial semimajor axes $a(t = 0)$ are drawn from K4C4 and K4C7 MMR simulations at t_{disk} in the same way as for the regular NON-MMR simulations. Migration parameters K4C4 and K4C7 are specifically chosen because of the 3:2 nominal MMR locations. The 3:2 nominal MMR locations tend to go unstable much earlier than 2:1, as we saw in section 3.2.2. This is important since instabilities are countered by small eccentricities. In fact, by testing I find that only a very small fraction of the 2:1 configuration goes unstable within t_{stop} when initialized with $e(t = 0) = 0$.

The comparisons to the standard NON-MMR simulations are done in the same way as described above in this section.

Chapter 4

Results

Each $K_e - C_1$ pair provides a set of MMR simulations for a resonance configuration. Each set of MMR simulations comes with a corresponding set of NON-MMR simulations. I compare MMR simulations with NON-MMR simulations for each given $K_e - C_1$ pair below. K-S and A-D tests are performed to check the null hypothesis H_0 that MMR- and NON-MMR simulation CDFs come from the same underlying distribution. The significance level that determines whether two distributions are statistically different or not is set to $\alpha = 0.05$ in this project. This significance level is chosen since it is commonly used in other works. With a Bonferroni correction each individual distribution comparison is tested using $\alpha^* = \frac{\alpha}{m}$. See section 3.3.2 for details about this. The number of K-S and A-D tests I perform is $m = 48$ (see section 3.3.2) which means $\alpha^* = 1.04 \cdot 10^{-3}$. This is the corrected significance level I use to determine whether two distributions are statistically different or not.

I also compare NON-MMR simulations to the NON-MMR-CIRCULAR simulations with $e(t = 0) = 0$ and small $i(t = 0)$. This is done in the exact same way. As explained in section 3.3.3 above these comparisons were only made for K4C4 and K4C7 in the 3:2 simulations.

The resulting comparison plots turns out to be very similar for all $K_e - C_1$ pairs. Therefore, for each resonance, the CDFs of only one $K_e - C_1$ pair is shown below. The CDFs for all the simulated $K_e - C_1$ pairs are explicitly found in appendix A. The important p-values of the hypothesis testing are summarized in a table in the end of the result section.

4.1 2:1 Nominal Resonance Configuration

4.1.1 K2C5

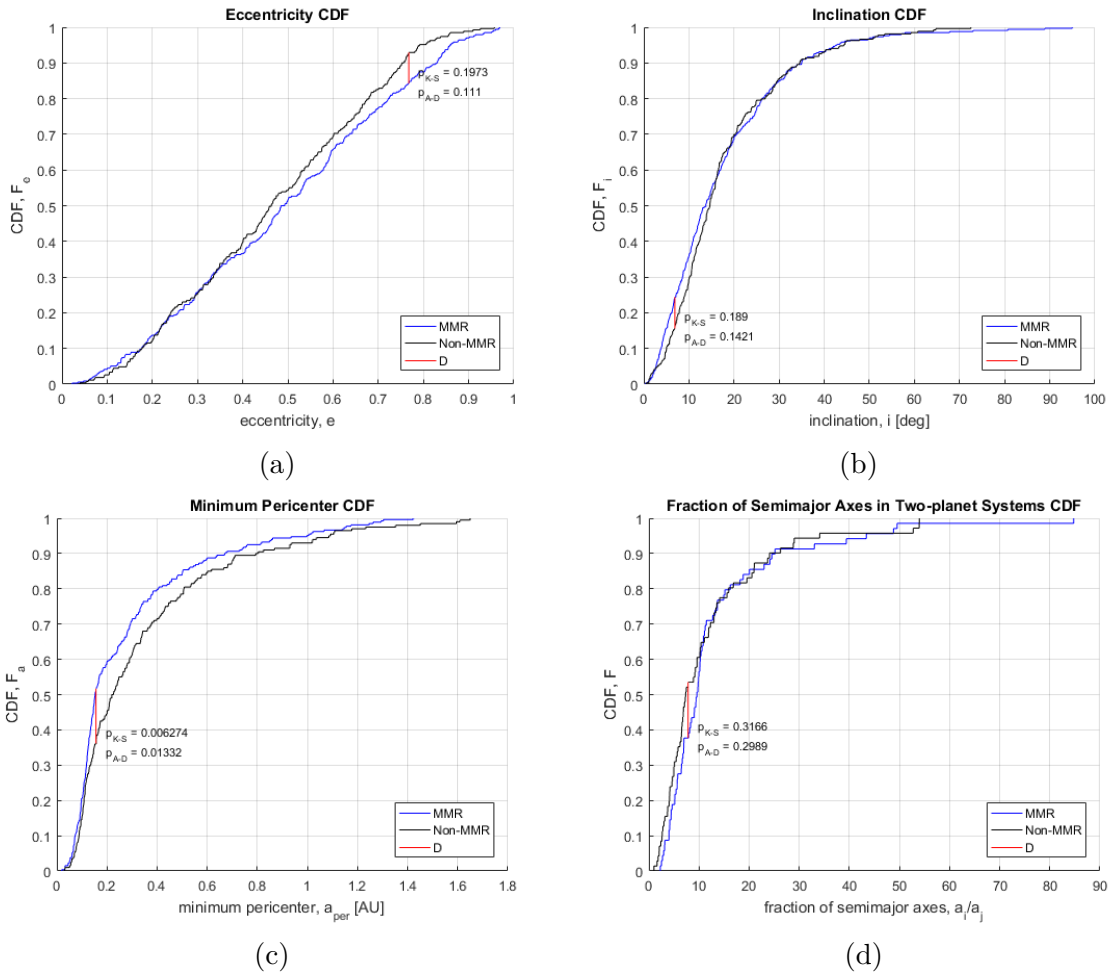

Figure 4.1: CDFs of surviving planets after the scattering phase, for K2C5. The results of MMR- and NON-MMR simulations are shown in the same plots for comparisons. Red vertical lines represent the K-S test statistic. K-S and A-D tests are performed to check the null hypothesis H_0. a) Eccentricity CDF. b) Inclination CDF. c) Minimum pericenter CDF. d) Ratios of semimajor axis in two-planet survivor systems CDF.

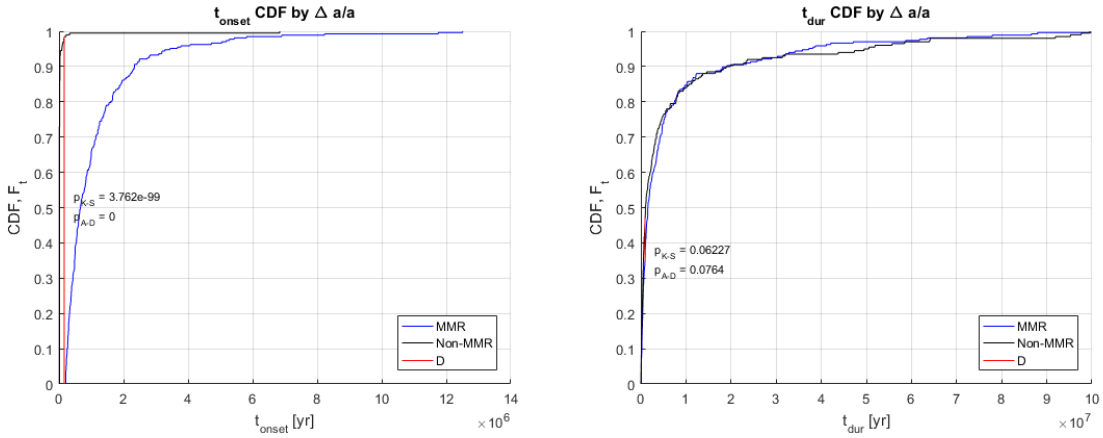

(a) (b)

Figure 4.2: CDFs of scattering phase timescales, for K2C5. The results of MMR- and NON-MMR simulations are shown in the same plots for comparisons. Red vertical lines represent the K-S test statistic. K-S and A-D tests are performed to check the null hypothesis H_0. a) Onset time of scattering phase CDF. b) Duration of scattering phase CDF.

4.2 3:2 Nominal Resonance Configuration

4.2.1 K4C4

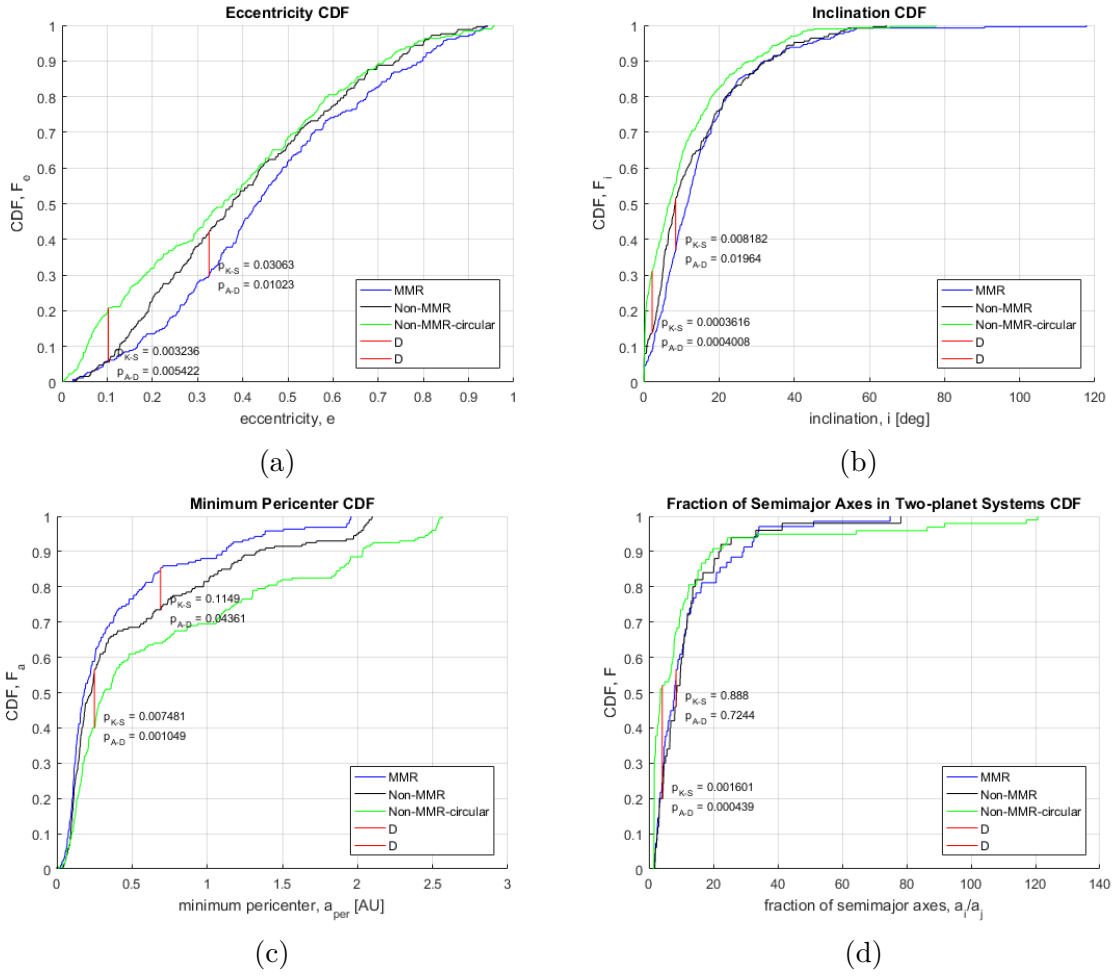

Figure 4.3: CDFs of surviving planets after the scattering phase, for K4C4. The results of MMR-, NON-MMR- and NON-MMR-CIRCULAR simulations are shown in the same plots for comparisons. Red vertical lines represent the K-S test statistic. K-S and A-D tests are performed to check the null hypothesis H_0. a) Eccentricity CDF. b) Inclination CDF. c) Minimum pericenter CDF. d) Ratios of semimajor axis in two-planet survivor systems CDF.

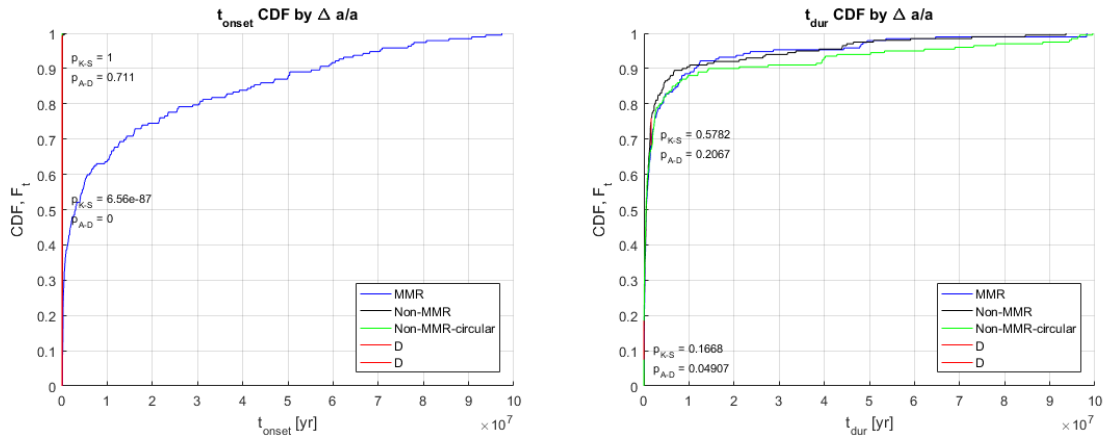

(a) (b)

Figure 4.4: CDFs of scattering phase timescales, for K4C4. The results of MMR-, NON-MMR- and NON-MMR-CIRCULAR simulations are shown in the same plots for comparisons. Red vertical lines represent the K-S test statistic. K-S and A-D tests are performed to check the null hypothesis H_0. a) Onset time of scattering phase CDF. b) Duration of scattering phase CDF.

4.3 Statistics and p-values

Kolmogorov-Smirnov test comparing MMR to NON-MMR

K-S	e	i	a_{per}	a_i/a_j	t_{dur}	t_{onset}
$K2C5$	$1.97 \cdot 10^{-1}$	$1.89 \cdot 10^{-1}$	$6.27 \cdot 10^{-3}$	$3.17 \cdot 10^{-1}$	$6.23 \cdot 10^{-2}$	$\mathbf{3.76 \cdot 10^{-99}}$
$K2C7$	$9.66 \cdot 10^{-1}$	$4.59 \cdot 10^{-1}$	$8.75 \cdot 10^{-1}$	$4.86 \cdot 10^{-1}$	$9.30 \cdot 10^{-1}$	$\mathbf{5.26 \cdot 10^{-81}}$
$K3C5$	$4.82 \cdot 10^{-1}$	$3.85 \cdot 10^{-3}$	$4.96 \cdot 10^{-1}$	$7.21 \cdot 10^{-1}$	$8.80 \cdot 10^{-1}$	$\mathbf{9.08 \cdot 10^{-110}}$
$K3C6$	$2.89 \cdot 10^{-1}$	$9.79 \cdot 10^{-1}$	$2.77 \cdot 10^{-2}$	$6.83 \cdot 10^{-1}$	$8.85 \cdot 10^{-2}$	$\mathbf{3.90 \cdot 10^{-81}}$
$K4C4$	$3.06 \cdot 10^{-2}$	$8.18 \cdot 10^{-3}$	$1.15 \cdot 10^{-1}$	$8.88 \cdot 10^{-1}$	$5.78 \cdot 10^{-1}$	$\mathbf{6.56 \cdot 10^{-87}}$
$K4C7$	$3.28 \cdot 10^{-1}$	$1.77 \cdot 10^{-1}$	$8.61 \cdot 10^{-3}$	$4.84 \cdot 10^{-1}$	$1.74 \cdot 10^{-1}$	$\mathbf{7.91 \cdot 10^{-121}}$

Table 4.1: p-values for the K-S hypothesis tests. Boldface numbers represent rejected H_0 at Bonferroni-corrected significance α^*.

Anderson-Darling test comparing MMR to NON-MMR

A-D	e	i	a_{per}	a_i/a_j	t_{dur}	t_{onset}
$K2C5$	$1.11 \cdot 10^{-1}$	$1.42 \cdot 10^{-1}$	$1.33 \cdot 10^{-2}$	$2.99 \cdot 10^{-1}$	$7.64 \cdot 10^{-2}$	**0**
$K2C7$	$6.87 \cdot 10^{-1}$	$4.47 \cdot 10^{-1}$	$7.31 \cdot 10^{-1}$	$4.41 \cdot 10^{-1}$	$6.40 \cdot 10^{-1}$	**0**
$K3C5$	$4.45 \cdot 10^{-1}$	$1.21 \cdot 10^{-3}$	$5.03 \cdot 10^{-1}$	$3.71 \cdot 10^{-1}$	$6.25 \cdot 10^{-1}$	**0**
$K3C6$	$1.66 \cdot 10^{-1}$	$6.29 \cdot 10^{-1}$	$2.17 \cdot 10^{-1}$	$5.07 \cdot 10^{-1}$	$6.64 \cdot 10^{-2}$	**0**
$K4C4$	$1.02 \cdot 10^{-2}$	$1.96 \cdot 10^{-2}$	$4.36 \cdot 10^{-2}$	$7.24 \cdot 10^{-1}$	$2.07 \cdot 10^{-1}$	**0**
$K4C7$	$3.47 \cdot 10^{-1}$	$6.80 \cdot 10^{-2}$	$2.82 \cdot 10^{-3}$	$6.13 \cdot 10^{-1}$	$1.58 \cdot 10^{-1}$	**0**

Table 4.2: p-values for the A-D hypothesis tests. Boldface numbers represent rejected H_0 at Bonferroni-corrected significance α^*.

Kolmogorov-Smirnov test comparing NON-MMR to NON-MMR-CIRCULAR

K-S	e	i	a_{per}	a_i/a_j	t_{dur}	t_{onset}
$K4C4$	$3.24 \cdot 10^{-3}$	$\mathbf{3.62 \cdot 10^{-4}}$	$7.48 \cdot 10^{-3}$	$1.60 \cdot 10^{-3}$	$1.67 \cdot 10^{-1}$	1
$K4C7$	$1.34 \cdot 10^{-3}$	$5.73 \cdot 10^{-3}$	$7.31 \cdot 10^{-2}$	$4.30 \cdot 10^{-3}$	$1.23 \cdot 10^{-1}$	$9.84 \cdot 10^{-1}$

Table 4.3: p-values for the K-S hypothesis tests. Boldface numbers represent rejected H_0 at Bonferroni-corrected significance α^*.

Anderson-Darling test comparing NON-MMR to NON-MMR-CIRCULAR

A-D	e	i	a_{per}	a_i/a_j	t_{dur}	t_{onset}
$K4C4$	$5.42 \cdot 10^{-3}$	$\mathbf{4.01 \cdot 10^{-4}}$	$1.05 \cdot 10^{-3}$	$\mathbf{4.39 \cdot 10^{-4}}$	$4.91 \cdot 10^{-2}$	$7.11 \cdot 10^{-1}$
$K4C7$	$\mathbf{1.04 \cdot 10^{-3}}$	$3.83 \cdot 10^{-3}$	$3.21 \cdot 10^{-2}$	$7.86 \cdot 10^{-3}$	$2.97 \cdot 10^{-2}$	$\mathbf{7.22 \cdot 10^{-5}}$

Table 4.4: p-values for the A-D hypothesis tests. Boldface numbers represent rejected H_0 at Bonferroni-corrected significance α^*.

Number of simulated systems and average number of collisions per simulation for each $K_e - C_1$ pair

$K_e - C_1$	N_s			f_c		
	MMR	NON-MMR	NON-MMR-CIRCULAR	MMR	NON-MMR	NON-MMR-CIRCULAR
$K2C5$	267	200	-	0.0861	0.08	-
$K2C7$	181	200	-	0.0552	0.0500	-
$K3C5$	340	199	-	0.0706	0.0603	-
$K3C6$	212	200	-	0.0755	0.0750	-
$K4C4$	192	200	200	0.2656	0.3600	0.3950
$K4C7$	421	200	198	0.1496	0.2500	0.3030

Table 4.5: Statistics of each $K_e - C_1$ pair. N_s is the number of successful simulations. f_c is the average number of collisions per simulation.

Average number of 1-planet and 2-planet survivors per system for each $K_e - C_1$ pair

$K_e - C_1$	f_{sys}, 1-planet			f_{sys}, 2-planet		
	MMR	NON-MMR	NON-MMR-CIRCULAR	MMR	NON-MMR	NON-MMR-CIRCULAR
$K2C5$	0.7416	0.6350	-	0.2584	0.3550	-
$K2C7$	0.5359	0.5500	-	0.4586	0.4400	-
$K3C5$	0.5941	0.6231	-	0.3941	0.3769	-
$K3C6$	0.4906	0.5700	-	0.5047	0.4300	-
$K4C4$	0.6302	0.7500	0.5100	0.3594	0.2500	0.4900
$K4C7$	0.6105	0.6050	0.4899	0.3895	0.3950	0.5101

Table 4.6: Average number of 1-planet and 2-planet survivors per system after relaxation f_{sys}. (The remaining few systems have either zero surviving planets or three surviving planets.)

4.4 Initial MMR Comparisons

In this section I compare MMR simulations to NON-MMR simulations.

4.4.1 Orbital Elements

Tables 4.1 and 4.2 show fairly large p-values for eccentricity and inclination comparisons. We are likely to find more extreme test statistics and the null hypothesis cannot be neglected for any of the $K_e - C_1$ pairs at the given $\alpha^* = 1.04 \cdot 10^{-3}$. Therefore the eccentricity and inclination of MMR simulations and NON-MMR simulations are consistent with being from the same underlying distribution. The eccentricity distributions are almost uniform over the allowed range, with small deficits at both very large and very small eccentricities, for all $K_e - C_1$ pairs. The inclination distributions are highly clustered around $0\,^\circ - 40\,^\circ$. These are good indications of planetary scattering, given that the systems started with smaller eccentricity and inclination.

The p-values and CDFs showing the fraction of semimajor axes in two-planet survivor systems, $\frac{a_i}{a_j}$, similarly show large p-values and very similar distributions. There seems to be a range of favoured fractions of semimajor axes after scattering since $\frac{a_i}{a_j}$ is clustered around $\sim 1.5 - 20$ for all $K_e - C_1$ pairs.

The minimum pericenter during integration is heavily clustered within $a_{per} < 0.25\,\mathrm{AU}$ for all $K_e - C_1$ pairs. The p-values for the pericenter hypothesis testing are generally large. Even the smallest p-values, for $K2C5$ and $K4C7$, are larger than the Bonferroni corrected significance level α^*, and thus H_0 cannot be neglected.

By looking at individual planets I find no statistical differences in the final distributions of eccentricity, inclination and minimum pericenter.

4.4.2 Scattering Timescales

The p-values for t_{onset} are very low indicating that the observed test statistics are extreme. In the CDF plots, figures 4.2a and 4.4a, we see that the MMR simulations have significantly larger t_{onset}, meaning the scattering phase starts late. For MMR simulations, t_{onset} seems to be very dependent on the migration parameters $K_e - C_1$. Most of the $K_e - C_1$ pairs have t_{onset} clustered around $\sim 1 - 2 \cdot 10^6\, yr$, although both K2C7 and K3C6 show significantly larger $t_{onset} \sim 10^7\, yr$. For NON-MMR simulations t_{onset} occurs within the first output timestep $\Delta t = 10^4$ yr.

Among the unsuccessful MMR simulations for each $K_e - C_1$ pair, I find that a large fraction of the total number of simulations are stable for the full t_{stop}.

The distributions of t_{dur} for MMR- and NON-MMR simulations are very similar. The p-values are not low enough to reject H_0 for any $K_e - C_1$. t_{dur} is highly clustered around $10^5 - 10^6\, yr$ for both MMR and NON-MMR simulations, meaning that this could be a typical range of scattering phase durations.

4.5 Initial Orbital Elements Comparisons

In this section I compare the NON-MMR simulations to NON-MMR-CIRCULAR simulations.

4.5.1 Orbital Elements

Given the significance level α^* I find that the eccentricity distributions in figure 4.3a are consistent with being from the same underlying distribution, despite NON-MMR showing a deficit in small e compared to NON-MMR-CIRCULAR. However, for K4C7, figure 7.11a, the A-D test shows a statistical difference. For the inclination I find, similarly but reversed, that the distributions for K4C4 in figure 4.3b are statistically different while the ones for K4C7 in figure 7.11b are consistent with being from the same distribution. This is again due to a deficit at small i for NON-MMR simulations.

As can be seen in figures 4.3c, 4.3d, 7.11c and 7.11d, the minimum pericenter and fraction of semimajor axes in 2-planet survivor systems show similar dependence on initial

e and i. The minimum pericenter during simulations is systematically larger for NON-MMR-CIRCULAR simulations, although the difference is not enough to be significant according to α^*. The final fraction of semimajor axes is smaller for NON-MMR-CIRCULAR simulations, which leads to a statistical difference for the K4C4 A-D test.

4.5.2 Scattering Timescales

As can be seen in figures 4.4a and 7.12a the onset time measured by the $\frac{\Delta a}{a}$ is not precise enough to properly compare NON-MMR to NON-MMR-CIRCULAR. This is due to the output time step $\Delta t = 10^4$ yr being larger than most t_{onset}. Therefore the p-values measured for t_{onset} between NON-MMR and NON-MMR-CIRCULAR cannot be trusted. In absence of MMR I can safely use the more precise close encounter routine method to compare the two. Without performing extra hypothesis tests, figure 4.5 shows that t_{onset} is systematically larger for NON-MMR-CIRCULAR.

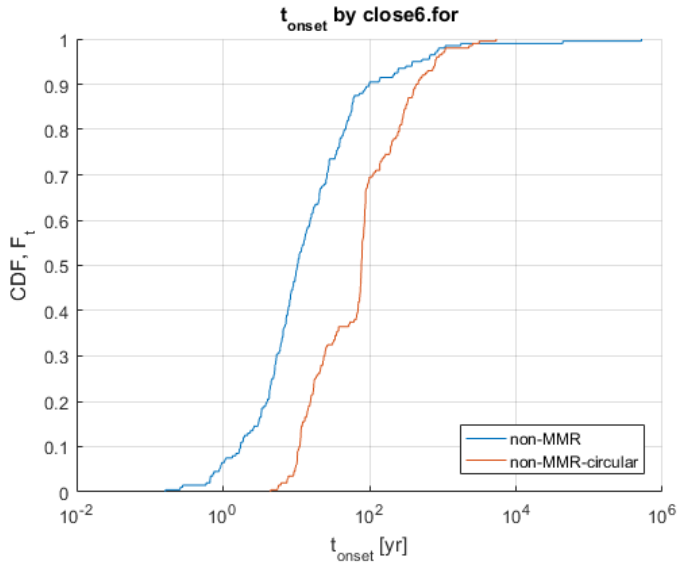

Figure 4.5: CDF of scattering phase onset time for K4C4. The results of NON-MMR and NON-MMR-CIRCULAR are shown in the same plot for comparisons. Note the logarithmic scale on the x-axis.

The duration of scattering shows large p-values similar to those measured when comparing MMR to NON-MMR. H_0 cannot be neglected for t_{dur}

Chapter 5

Discussion

Is initial MMR important for the planetary scattering phase? My results indicate that most of the analyzed parameters of the scattering phase are not directly correlated with initial MMR. However, as migration in MMR significantly changes the orbital elements, initial MMR has an indirect effect on the scattering phase. Initial MMR determines the orbital elements prior to the scattering phase which then affects the scattering. The effect seems to be systematic an in section 5.2 below I show the influence that initial e and i has on the final orbital elements and scattering timescales.

5.1 MMR Correlations

5.1.1 Orbital Elements

Based on the results in chapter 4, I find that eccentricity, inclination, minimum pericenter and fraction of semimajor axes in two-planet survivor systems are all uncorrelated with initial MMR. It seems that the planetary scattering phase quickly removes any relics in orbital elements from initial MMR. Based on the existance of short t_{dur} it is likely that any observable trace (e, i or $\frac{a_i}{a_j}$) of initial MMR is erased early on during the scattering phase, possibly even in the first couple of scattering events.

Following the discussion in Carrera et al. (2016) the minimum pericenter being uncorrelated with MMR implies that the survival rate of terrestrial planets at small separations is the same for systems initially in MMR and systems that are not.

5.1.2 Scattering Timescales

Onset Time of Scattering

The onset of scattering t_{onset} is highly correlated with MMR. In fact, initial MMR causes t_{onset} to occur significantly later than for NON-MMR simulations. This is not surprising considering the restoring force and geometry of MMR systems. As described in the Theory section (2.2), the forces on a planet in a system with at least one more planet can be treated as a two-body (star-planet) system with a perturbing force from the other planets. The perturbing force grows large as planets approach each other. In a non-resonant, non-circular system, the perturbing force is not periodic and acts in a chaotic way which increases eccentricity (and inclination) until orbits cross. The first close encounter starts the scattering phase. In a system in MMR, most of the perturbing force is periodic and acts to keep the system in the exact orbital configuration. This is the restoring force. Without external forces, such as planet-disk interactions, the increase in eccentricity (and inclination) is slow, even for tight orbital configurations. The restoring force can counter weak close encounters and protect a system from scattering. As can be seen in figure 2.2, a MMR configuration also naturally protects against close encounters due to the eccentricities, alignments and periods of the orbits (geometry of MMR). This is mathematically described by taking $\dot{\phi} \approx 0$ in equation 2.14. The orbital geometry of a non-resonant system is random and close encounters can occur more frequently.

Onset Time Method Comparisons

Figures 5.1 and 5.2 show the onset time of the scattering phase as calculated by the three methods described in section 3.3.1: The semimajor axis excursions ($\frac{\Delta a}{a} \geq 10\%$), the built-in close encounter analysis tool in MERCURY6.2 (CLOSE6.FOR) and the orbital crossing approximation. I show the onset time here for the same $K_e - C_1$ pairs displayed in the result section. For NON-MMR simulations t_{onset} occurs very early for all methods considered. All three methods are consistent , see figures 5.1b and 5.2b. On the other hand, for the MMR simulations, figures 5.1a and 5.2a, t_{onset} determined by the simple orbital crossing condition differs from the other methods. Below I explain why the $\frac{\Delta a}{a}$ condition is the best method for determining t_{onset} and why the simple orbital crossing method does not work.

According to the simple treatment of comparing pericenter of the outer orbit to apocenter of the inner orbit, all systems have orbital crossing already before the disk dispersion t_{disk} (t_0 for NON-MMR). During migration in MMR eccentricity becomes excited enough to fulfill the simplified orbital crossing condition. Due to the orbital geometry of MMR most of these systems avoid close encounters and can stay stable for long times, even though orbits cross. On the other hand, the NON-MMR systems have the same distribution of eccentricity and semimajor axes as the MMR systems at t_{disk}, but without ordered MMR

orbital geometry (all orbital elements are drawn randomly from given distributions). For this reason, close encounters start immediately at t_0. This is most likely the main reason for later t_{onset} in my MMR simulations. It is also the reason why the simple orbital crossing method is not good enough. The method can be significantly improved by taking the orbital angles ω, Ω and i into account to find true orbit crossings. However, systems in MMR can avoid close encounters even though orbits cross.

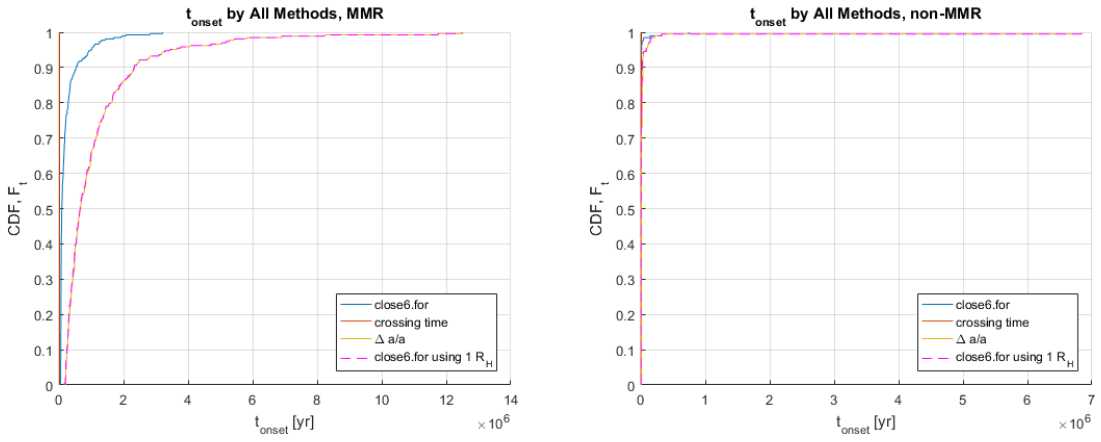

(a) (b)

Figure 5.1: Onset time of scattering phase CDF, for K2C5. Different colours represent the various methods used for estimating t_{onset}: The semimajor axis excursions ($\frac{\Delta a}{a}$), the built-in close encounter analysis tool in MERCURY6.2 (CLOSE6.FOR) and the orbital crossing time. For this project $\frac{\Delta a}{a} \geq 10\%$ is considered most reliable. a) MMR simulations. b) NON-MMR simulations.

Another important feature can be seen in figure 5.1a. Evidently, t_{onset} measured by CLOSE6.FOR is significantly earlier than for the $\frac{\Delta a}{a}$ condition. This was predicted due to the restoring force overcoming weak close encounters, keeping the system in MMR. In the CLOSE6.FOR routine, a close encounter is defined as one of the planets having the other planet at a distance $r \leq 3\,R_H$, where R_H is the Hill radius of the considered planet, defined in equation 2.33. I limit the search to stronger close encounters by instead imposing the requirement $r \leq R_H$. This is shown by the purple dashed line in figures 5.1 and 5.2. The stronger close encounters provide an almost identical distribution of t_{onset} as the $\frac{\Delta a}{a}$ method (yellow line), supporting both the validity of the $\frac{\Delta a}{a}$ condition and the argument of the restoring force overcoming weak close encounters.

The trend of weak close encounters being countered by the restoring force is only visible for two $K_e - C_1$ pairs: K2C5 and K3C5. By analysis of eccentricity at t_{disk} I find that these two $K_e - C_1$ pairs provide migration parameters that results in the largest eccentricity at t_{disk}. Remember, small K_e values means low eccentricity damping and thus high eccentricity. Small C_1 values means rapid and long migration. The implication for eccentricity is ambiguous: rapid migration means large eccentricity excitation but at the

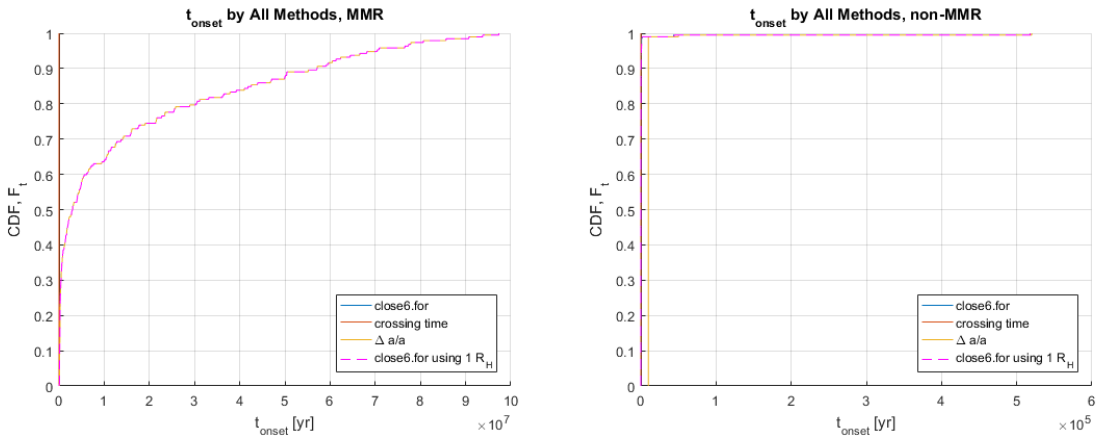

(a) (b)

Figure 5.2: Onset time of scattering phase CDF, for K4C4. Different colours represent the various methods used for estimating t_{onset}: The semimajor axis excursions ($\frac{\Delta a}{a}$), the built-in close encounter analysis tool in MERCURY6.2 (CLOSE6.FOR) and the orbital crossing time. For this project $\frac{\Delta a}{a} \geq 10\%$ is considered the most reliable method. Note that for the K4C4 migration and damping parameters, the $\frac{\Delta a}{a}$ and the CLOSE6.FOR methods give the same t_{onset}. a) MMR simulations. b) NON-MMR simulations.

same time large eccentricity damping. Visualized in figure 3.8, simulations on the lower left side (low Ke and C_1) result in large eccentricity while simulations on the lower right side result in small eccentricity. Sufficiently high eccentricities means that orbits come close to each other and have close encounters, even despite MMR geometry. At the same time, large eccentricity also means that the orbital velocity is rapid at pericenter and slow at apocenter. Thus close encounters are rapid and weak and can be overcome by the restoring force.

Finally, for a given resonance, the distribution of t_{onset} seems to vary heavily with $K_e - C_1$ for MMR simulations. This behaviour can be explained simply by the eccentricity and inclination distribution at t_{disk} which depend on the migration parameters $K_e - C_1$. In general, small C_1 and small K_e leads to the largest eccentricity at t_{disk} and thus also the earliest t_{onset} (see figure 3.8 and associated paragraphs).

Duration of Scattering

I find no correlation between t_{dur} and initial MMR. This suggests that the three-planet MMR chains are generally broken at the same time the scattering phase start, and any initial trace of MMR is quickly removed. Even though the onset close encounter occurs between two planets, the scatter seems to be enough to break the other resonant pair as

well. Potentially this can be different for systems with more than three planets and/or non-equal planetary mass.

5.2 Initial Orbital Element Correlations

I compare NON-MMR simulations with NON-MMR-CIRCULAR. In tables 4.3 and 4.4 we see that the hypothesis tests results in quite small p-values. This indicates that NON-MMR and NON-MMR-CIRCULAR parameters are less similar than comparing MMR to NON-MMR. In which cases is this significant enough to infer statistically differing distributions?

5.2.1 Orbital Elements

Both the final eccentricity- and inclination distributions are on the border of being statistically different comparing NON-MMR to NON-MMR-CIRCULAR. The NON-MMR-CIRCULAR simulations feature smaller e and i of relaxed systems than NON-MMR thus confirming that initial values of e and i indeed affects the scattering phase and the relaxed systems. It seems that starting systems with small e and i results in slightly smaller final e and i after the scattering phase, compared to starting the simulations with significant e and i. As mentioned already in section 3.2.7, the orbital elements a, e and i determine the total energy E_{tot} and angular momentum L_{tot} of a multi-planet system. Generally, these are the only conserved quantities in a planetary system. Therefore it is not surprising that the initial e and i just prior to the scattering phase affect the relaxed system. For this reason, direct comparisons between distributions of orbital elements from this work to other works are biased.

Although not quite enough to be statistically different according to α^* the minimum pericenter of NON-MMR-CIRCULAR simulations seems to be larger than for NON-MMR simulations. This is not surprising given that NON-MMR-CIRCULAR has lower eccentricity. The smaller fraction of semimajoraxes in 2-planet survivor systems for NON-MMR-CIRCULAR is also expected, given that small eccentricity systems can be stable at closer orbital separation.

5.2.2 Scattering Timescales

In the Result section (figure 4.5) we saw that t_{onset} is systematically later for NON-MMR-CIRCULAR simulations compared to NON-MMR simulations. This is expected since low e leads to more stability.

My results show that the duration of scattering is not different given differing initial e and i. Combined with the similarities of t_{dur} between MMR and NON-MMR it seems that the duration of the scattering phase is independent of initial conditions, at least for systems of three equally massive planets. It should be noted that the timescales of scattering, both t_{onset} and t_{dur}, are expected to depend heavily on the semimajor axis which sets the orbital time scale.

5.3 Collisions

The average number of collisions per simulation does not seem to be correlated with initial MMR for the 2:1 configuration. However, for the 3:2 configuration I see two things: a) The number of collisions increases drastically for 3:2 resonances compared to 2:1. This is because of the tighter orbital separation of both individual planets and the planets and the star, as discussed in section 3.3.1. b) The average number of collisions per simulation seems to be lowest for MMR simulations and largest for NON-MMR-CIRCULAR simulations. As seen in section 3.3.1 increased number of collisions should lead to lower final eccentricity. Could this be one of the reasons behind the low final eccentricity in the NON-MMR-CIRCULAR simulations? Because of the following two findings, collisions most likely have a negligible effect on the final eccentricities in my simulations: I do not find any statistical differences in the final eccentricities of MMR and NON-MMR simulations, even though the NON-MMR simulations feature more collisions. Furthermore, K4C4 simulations does not have lower eccentricities than K4C7 simulations, even though they feature more collisions.

5.4 Implications and Recommendations

In this project I find that all but one of the chosen parameters, e, i, a_{per}, a_i/a_j and t_{dur}, are uncorrelated with initial MMR for a system that has undergone a scattering phase. In the light of this it is tempting to draw the conclusion that MMR need not be considered in planetary scattering simulations where only these parameters are of interest. However, as is evident from section 3.2.6 the initial semimajor axes, eccentricities and inclinations affect the final relaxed distributions of e, i, a_{per} and a_i/a_j. I have found that the orbital elements a, e and i before the scattering phase (at t_{disk}) do depend heavily on the preceding MMR evolution. For this reason, initial MMR indeed has an indirect effect on e, i and a_i/a_j of a relaxed system, as well as on the minimum a_{per}. Whether this effect is significant enough to deduce initial MMR in a system that underwent scattering is a scope for future work. For example one could compare systems that migrate directly into scattering without capture in MMR to systems that migrate and capture in MMR before scattering. In such

simulations, the systems that migrate directly into scattering without MMR would most likely start the scattering phase with smaller e and i compared to MMR systems.

For future works on planetary scattering, MMR can safely be decoupled from the scattering simulations as long as t_{onset} is not of interest. By using a, e and i at t_{disk} from previous MMR simulations, a scattering simulation with these initial conditions (no MMR) is equally good as the full initial MMR treatment presented in this work.

The duration of the scattering phase is independent of the system being in MMR initially. It also seems to be independent of initial e and i. However, due to orbital timescales, t_{dur} is most likely dependent on a. Since MMR affects the initial semimajor axes for the scattering phase, it could have a small indirect effect on t_{dur}. The onset of the scattering phase and similarly the long term stability of a system is, both directly and indirectly, dependent on MMR. An MMR system is, due to the geometry of MMR orbits and the restoring force, inherently more stable than a NON-MMR system. For projects where the onset of scattering is of interest MMR cannot be neglected.

5.5 Comparisons to Other Works

In accordance with Carrera et al. (2016) I find that systems of three equally massive giant planets have pericenters that span the whole inner planetary system during the simulations. Such a system would scatter large quantities of super Earth candidates found at small orbital separations.

In Jurić & Tremaine (2008) they define different regions of scattering based on the final eccentricity distribution, the amount of evolution from the initial eccentricity and the smallest initial Hill separation D_{min}. Systems with $D_{min} \leq 1$ are active systems that undergo violent planetary scattering. The final eccentricity distribution of active systems seems to converge towards a common distribution regardless of the initial conditions, the end point of planetary scattering. This is in contrast to the inclination distribution which is dependent on initial conditions, in particular on the initial number of planets (Jurić & Tremaine 2008). Partially active systems $D_{min} \in [1, 10]$, while undergoing scattering, do not reach the same final eccentricity distribution as active systems. The eccentricity distribution of partially active systems possibly retains some memory of the initial conditions (Jurić & Tremaine 2008). Inactive systems are essentially stable for the full t_{stop}. They feature little or no planetary scattering and retain their initial eccentricity distribution.

According to the D_{min} criterion, all of my systems are partially active. However, my D_{min} measure is defined for circular orbits. Due to the significant eccentricity right before scattering, my MMR- and NON-MMR systems would most likely be active. My NON-MMR-CIRCULAR simulations are partially active. Therefore, the differences between NON-MMR

and NON-MMR-CIRCULAR are due to them being active and partially active systems respectively, in accordance with Jurić & Tremaine (2008). Expanding upon this, according to Jurić & Tremaine (2008), creating a new NON-MMR-ECCENTRIC simulation set using larger initial e and i than NON-MMR simulations should mean no differences in the relaxed eccentricity distribution since both systems are classified as active. It is important to note that Jurić & Tremaine (2008) use a wider range of initial conditions, including large numbers of initial planets and non-equal masses in the range $m_p \, \epsilon \, [0.1, 10] \, M_J$.

In Libert & Tsiganis (2011) they investigate various resonance captures for 3-planet systems of masses similar to M_J. Migration forces and eccentricity- and inclination damping are applied to make the planets capture and migrate in MMR. They find that all systems initially enter eccentricity resonances which excite eccentricity. For low enough eccentricity damping (low K_e-value), eccentricity can grow large enough to trigger inclination resonance. Migration in inclination resonances similarly excite inclination rapidly. Inclination of the planets in the system can then grow up to $i \sim 35°$.

In this work I see the exact same behaviour. Specifically for low K_e coupled with low C_1 eccentricity is rapidly excited in MMR migration. At large enough equilibrium eccentricity the systems enter inclination type resonances and inclinations are excited, which can be seen in figure 5.3 for K2C5. This occurs for systems in K2C5 and K3C5 where the inclination at t_{disk} is significant. For K2C7 and K3C6 inclination resonances occur as well but not as pronounced since C_1 is bigger. For systems in K4C4 and K4C7 inclination resonances are never triggered, most likely because of large K_e.

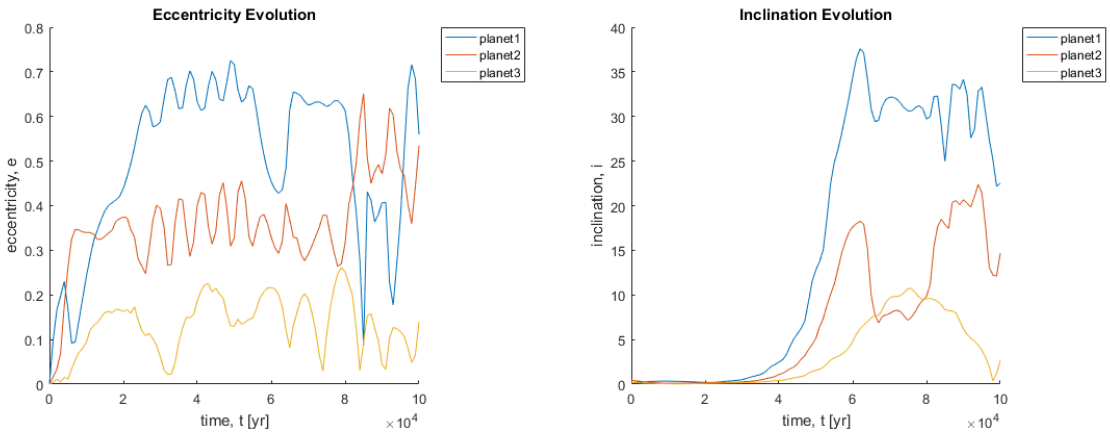

(a) (b)

Figure 5.3: The evolution of eccentricity and inclination of the three planets until t_{disk} in MMR simulations. The figure shows the result for K2C5 migration parameters. The system enters inclination resonances after eccentricities have been excited sufficiently. a) Eccentricity evolution. b) Inclination evolution.

5.6 Limitations and Future Work

As a natural extension to this project it would be interesting to test more resonances than 2:1 and 3:2 to get more statistics. Libert & Tsiganis (2011) has shown that, for a range of initial semimajor axes in three-giant planet systems $m_p \leq 1.5\,M_J$, the most common resonance captures are 2:1 and 3:1. Furthermore they find that, for the considered planetary masses, capture into the 3:2 resonance is very rare, due to its unstable configuration. Based on this, it would be of interest to investigate the 3:1 resonance in the future.

To expand on the generality of the project it would be interesting to repeat the simulations using non-equal planetary masses and more planets than three. This would also make the simulations more realistic. Non-equal planet masses leads to more stable systems (Chambers et al. 1996). Furthermore it means that the most massive planets are less affected by the scattering phase while the less massive planets are more strongly affected. Therefore the final orbital elements of relaxed systems would probably show a wider spread. Adding more planets would most likely make the systems more unstable. It might also increase the duration of the scattering phase since more planets needs to be ejected in order to achieve stability. Inclusion of both unequal masses and more planets would most likely affect the investigated parameters, in particular the stability of the systems, but would it affect MMR and NON-MMR simulations differently? For example, the t_{dur} (and other parameters) of the MMR systems could be affected as parts of the system potentially remains in MMR for some time when one two-planet resonance is broken (due to the restoring force). However, resonance crossing and irregular perturbing forces that ensues from planetary scattering might well destabilize the rest of the system quickly after the first scattering anyway. In this work I have neglected to include unequal masses and more planets due to the time constraint.

For the purpose of the science goal of this report, some physics have been greatly simplified or even overlooked. I'm referring mainly to the planet-disk interactions (migration eccentricity- and inclination damping), the growth of planets in a protoplanetary disk, the disk dispersion and tidal interactions with the star. In the future these areas can be expanded on. For example one might implement planetary growth and more realistic migration as in e.g. Bitsch et al. (2015), and refined eccentricity- and inclination damping prescriptions from hydrodynamical code e.g. Sotiriadis et al. (2017) and Bitsch et al. (2013). For an extensive treatment of the disk dispersion one could make use of Bitsch et al. (2015).

In Correia et al. (2017) they argue that simply measuring T_2/T_1 for two planets is not enough to determine MMR. For a robust MMR determination one needs to analyze the time evolution of the resonance angle ϕ to see that it librates. For my work, determining MMR by T_2/T_1 can be justified because I am actively trying to make systems capture into MMR. In my simulations I expect systems to either capture into MMR during migration

or go unstable and scatter due to a stationary inner planet. A system ending up with the nominal MMR T_2/T_1 by chance in this case is extremely improbable.

In table 4.5 I find that, despite efforts to get a sample size comparable to the observed sample $N_p \sim 300 \rightarrow N_s \sim 200$ (N_p = number of surviving planets, N_s = number of systems), some of the MMR simulations have many more successful systems, e.g. the K4C7 simulations has $N_s = 421$. For the NON-MMR simulations I find that $N_s \sim 200$ for all migration and damping parameters. This means that I compare two distributions that can have large differences in the number of data points. The two-sample hypothesis tests, both K-S and A-D, might be affected by such differing distribution sizes. A limitation of this work is therefore not investigating the effects of differing distribution sizes in two-sample K-S and A-D tests.

By looking at tables 4.1, 4.2, 4.3, 4.4 there is a large difference between the p-values for MMR to NON-MMR comparisons and NON-MMR to NON-MMR-CIRCULAR comparisons. This indicates that NON-MMR- and NON-MMR-CIRCULAR distributions might be different. On the other hand there are only a few comparisons in tables 4.3 and 4.4 that can reject the null hypothesis due to the very strict significance level α^*. This signals that the Bonferroni correction might be too strict in this case. It might be more instructive to disregard the significance level and look only at the p-values relative to each other.

Expanding upon this, by looking at tables 4.1, 4.2, 4.3 and 4.4 the differences in p-values between the K-S and A-D tests for the same two-sample comparison are in some cases quite large. This signals that one of the tests might not be good enough for this purpose. Generally the A-D test is regarded as better than the K-S test for comparing distributions. Instead of the K-S test it would have been interesting to perform some multidimensional hypothesis test, taking into account correlations between the different variables I analyzed.

Finally, due to lack of time I have omitted to make comparisons to observed giant exoplanet eccentricity and inclination distributions. This would be interesting to do as an expansion to this work.

Chapter 6

Conclusions

In this work I have tested the importance of mean motion resonances for dynamically unstable planetary systems that undergo a scattering phase. I have numerically simulated planet systems of three Jupiter-mass planets around a solar mass star. The simulations are split in two parts: MMR simulations, with the planets locked in specific resonance chains before the scattering phase, and NON-MMR simulations, with similar initial conditions but no MMR before the scattering phase. All systems undergo significant planetary scattering and subsequent relaxation after one or more planets were ejected.

I show by hypothesis testing, using K-S and A-D tests, that the distribution of eccentricity and inclination of the surviving planets is the same for MMR and NON-MMR simulations. I conclude that eccentricity and inclination of planets that underwent scattering is not directly correlated with initial MMR. The final eccentricity and inclination seems to be a product of the chaotic scattering phase only and show no relics from initial resonance chains. In a similar manner, the minimum pericenter of any planet in the system during the scattering phase and the ratio of final semimajor axes in two-planet survivor systems is not directly correlated with initial MMR.

The starting time of the scatter phase is statistically different comparing MMR- to NON-MMR simulations. NON-MMR systems enter the scattering phase much earlier than the MMR systems, most likely due to the geometry and restoring force of MMR. In general t_{onset} is different for different planet-disk interaction parameters. Critically dependent on K_e and C_1, I find that a large fraction of MMR systems stay stable for the full t_{stop}, while corresponding NON-MMR systems undergo scattering. Furthermore, it seems that very eccentric MMR systems can have close encounters without going unstable due to the strong restoring force.

The duration of the scattering phase is not directly correlated with initial MMR. In this work we have worked exclusively with systems of three equally massive planets. For

future works it would be interesting to test correlations between t_{dur} and initial MMR for systems of more planets and/or unequal masses.

I compared my significant initial eccentricity and inclination NON-MMR simulations to similar NON-MMR-CIRCULAR simulations using circular orbits with small inclinations. I find that the distributions of orbital elements and onset time of scattering comparing NON-MMR and NON-MMR-CIRCULAR are border-lining the given significance level. In other words, I see slight correlations between initial eccentricity/inclination values and the final distributions of e, i, a_{per}, a_i/a_j and t_{onset}. However, these correlations are significant only in a few cases. I conclude that when comparing this work to other works on scattering using small initial e and i, there will be slight differences. Note that this does not affect the duration of the scattering phase which seems to be independent of initial conditions (except for initial semimajor axis).

For systems of three equally massive planets it seems that MMR-chains are broken in the first, or first few, major close encounters ($r \leq R_H$). The time of the first major close encounter is very different between MMR- and NON-MMR systems. After MMR has been broken, any trace of initial MMR is quickly removed during the scattering phase. After relaxation there is no observable distinction between initial MMR and initial non-MMR. However, as we have seen, MMR evolution significantly affects the initial conditions for scattering. MMR keeps the system locked in specific orbital configurations and excites eccentricity, and sometimes also inclination, to high levels. The initial orbital elements for the scattering phase, comparing a system that captured into MMR during migration and a system that failed to capture, will therefore be inherently different. This means that, indirectly, MMR has an effect on the final orbital elements of a relaxed system. This can be expanded upon in future work.

Chapter 7

Appendix

7.1 A: Complete Set of Results

7.1.1 2:1 Nominal Resonance Configuration

K2C5

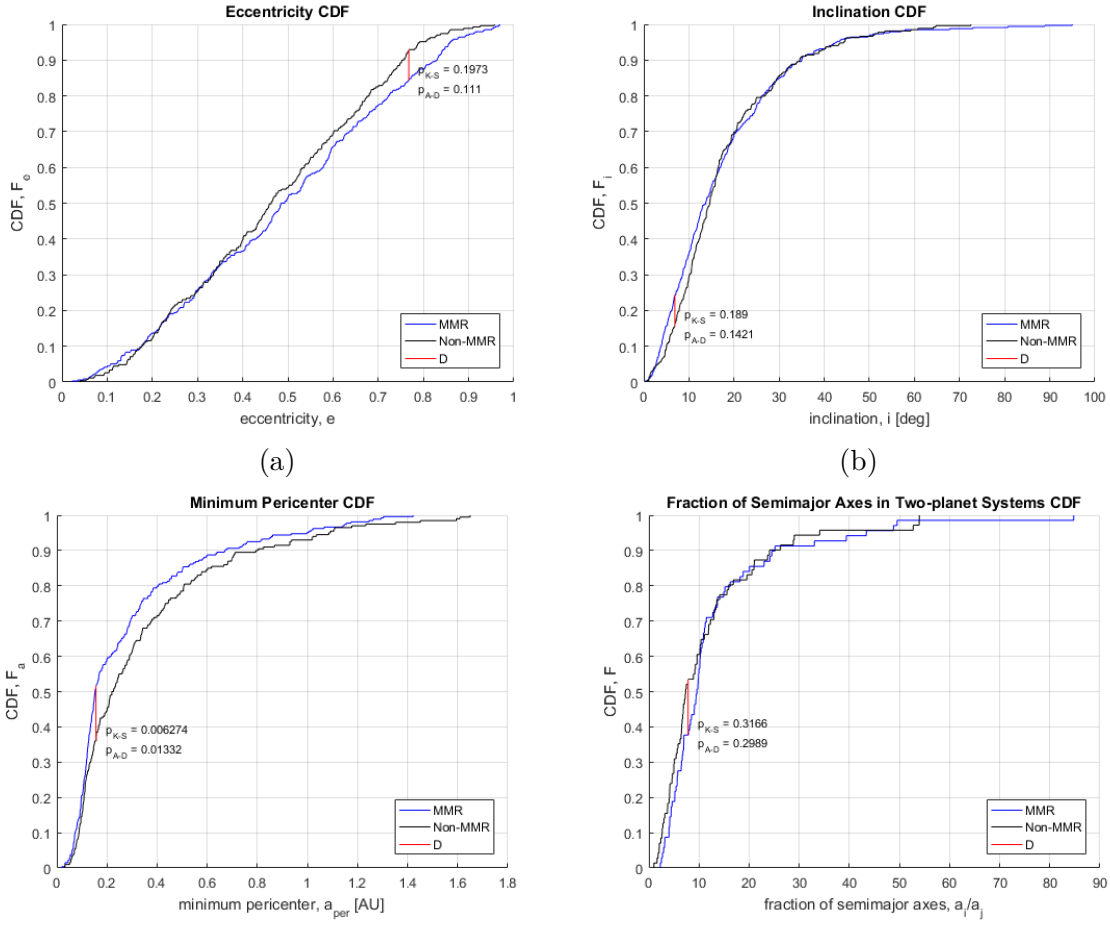

Figure 7.1: CDFs of surviving planets after the scattering phase, for K2C5. The results of MMR- and NON-MMR simulations are shown in the same plots for comparisons. Red vertical lines represent the K-S test statistic. K-S and A-D tests are performed to check the null hypothesis H_0. a) Eccentricity CDF. b) Inclination CDF. c) Minimum pericenter CDF. d) Ratios of semimajor axis in two-planet survivor systems CDF.

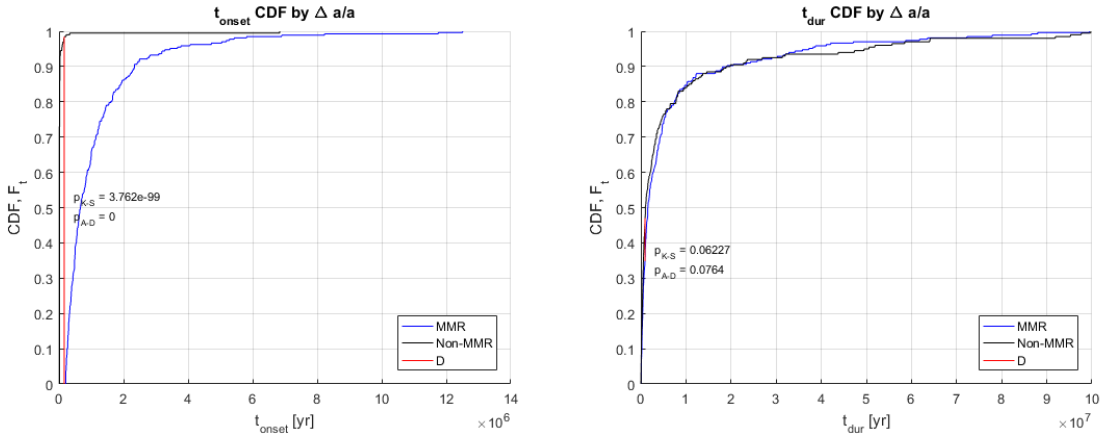

(a) (b)

Figure 7.2: CDFs of scattering phase timescales, for K2C5. The results of MMR- and NON-MMR simulations are shown in the same plots for comparisons. Red vertical lines represent the K-S test statistic. K-S and A-D tests are performed to check the null hypothesis H_0. a) Onset time of scattering phase CDF. b) Duration of scattering phase CDF.

K2C7

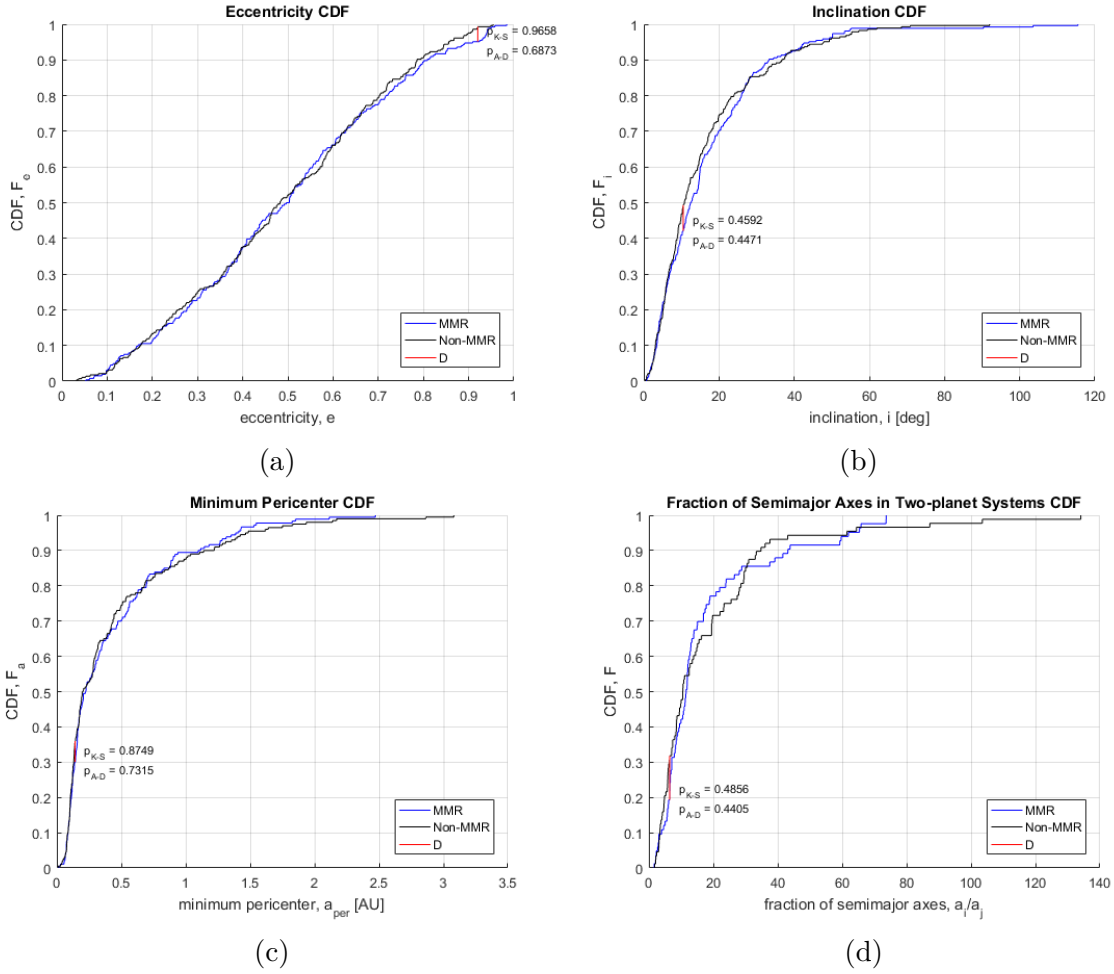

Figure 7.3: CDFs of surviving planets after the scattering phase, for K2C7. The results of MMR- and NON-MMR simulations are shown in the same plots for comparisons. Red vertical lines represent the K-S test statistic. K-S and A-D tests are performed to check the null hypothesis H_0. a) Eccentricity CDF. b) Inclination CDF. c) Minimum pericenter CDF. d) Ratios of semimajor axis in two-planet survivor systems CDF.

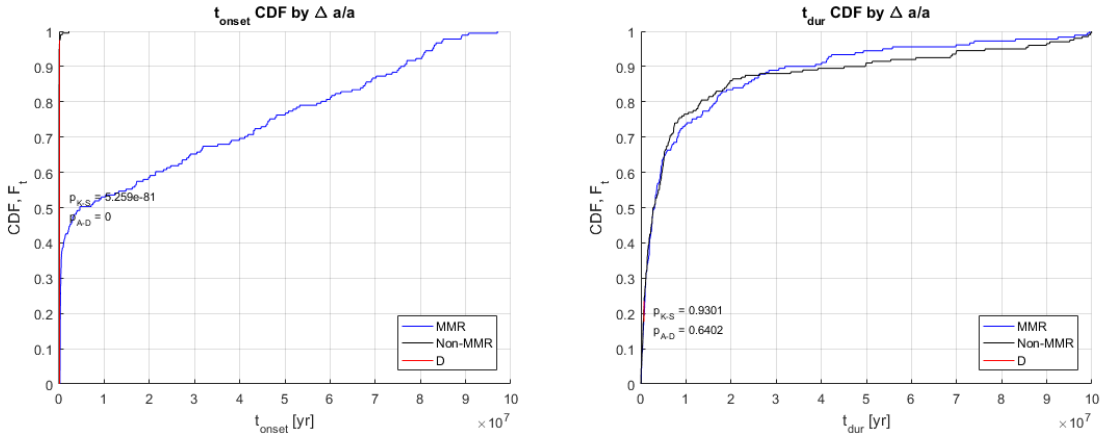

(a) (b)

Figure 7.4: CDFs of scattering phase timescales, for K2C7. The results of MMR- and NON-MMR simulations are shown in the same plots for comparisons. Red vertical lines represent the K-S test statistic. K-S and A-D tests are performed to check the null hypothesis H_0. a) Onset time of scattering phase CDF. b) Duration of scattering phase CDF.

K3C5

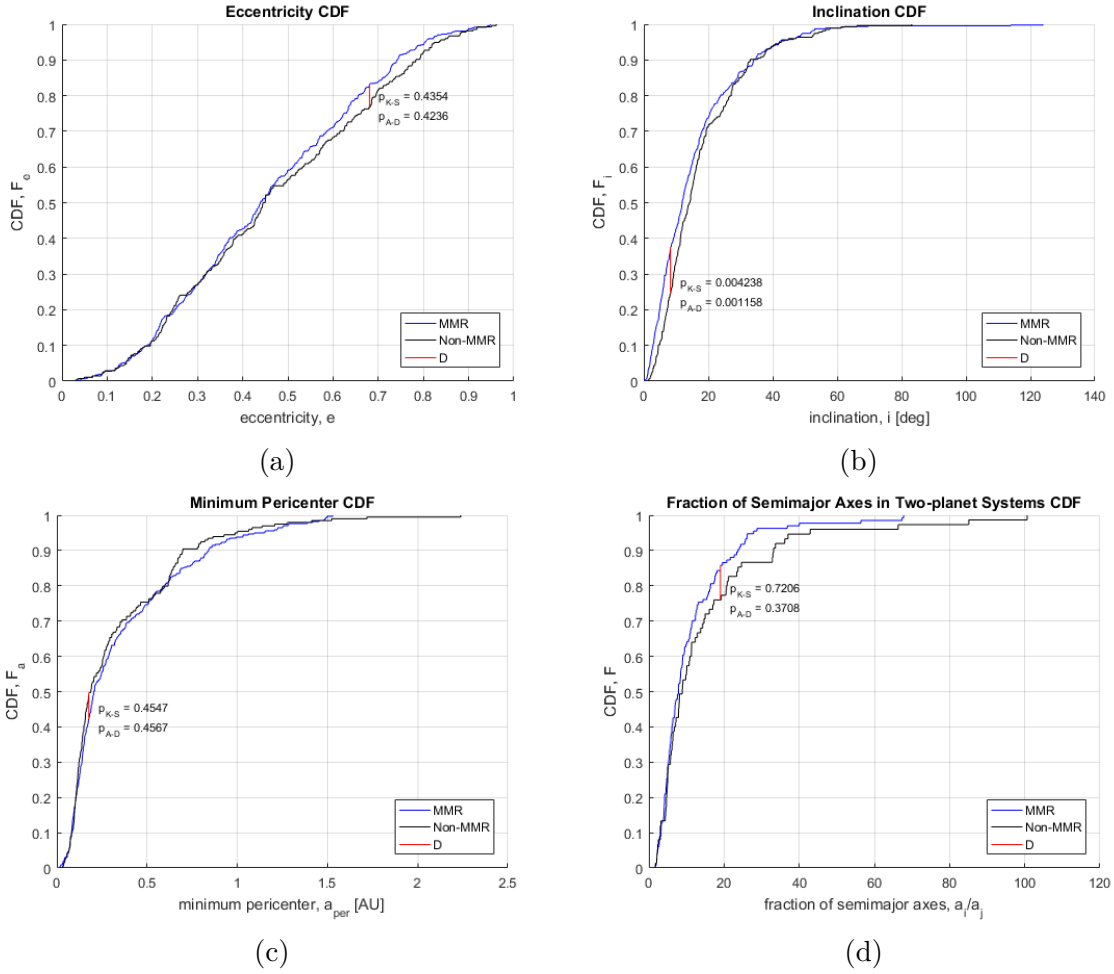

Figure 7.5: CDFs of surviving planets after the scattering phase, for K3C5. The results of MMR- and NON-MMR simulations are shown in the same plots for comparisons. Red vertical lines represent the K-S test statistic. K-S and A-D tests are performed to check the null hypothesis H_0. a) Eccentricity CDF. b) Inclination CDF. c) Minimum pericenter CDF. d) Ratios of semimajor axis in two-planet survivor systems CDF.

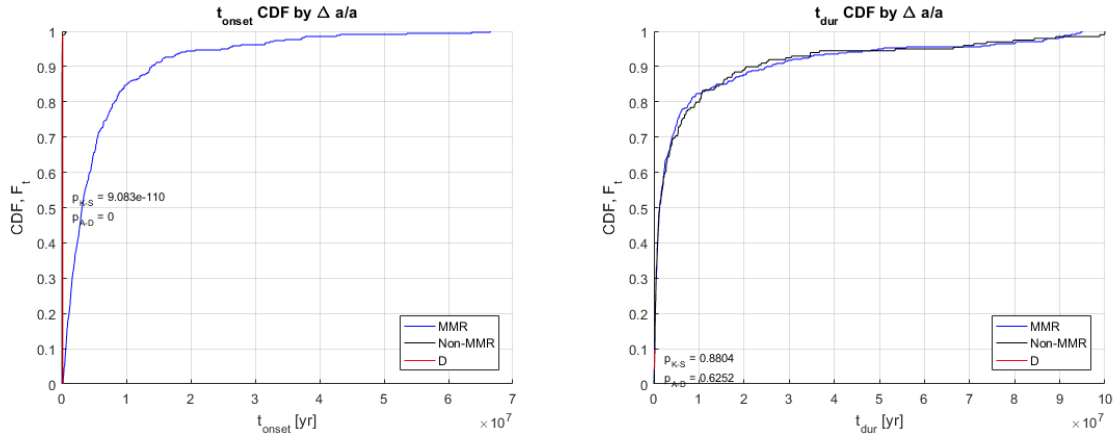

(a) (b)

Figure 7.6: CDFs of scattering phase timescales, for K3C5. The results of MMR- and NON-MMR simulations are shown in the same plots for comparisons. Red vertical lines represent the K-S test statistic. K-S and A-D tests are performed to check the null hypothesis H_0. a) Onset time of scattering phase CDF. b) Duration of scattering phase CDF.

K3C6

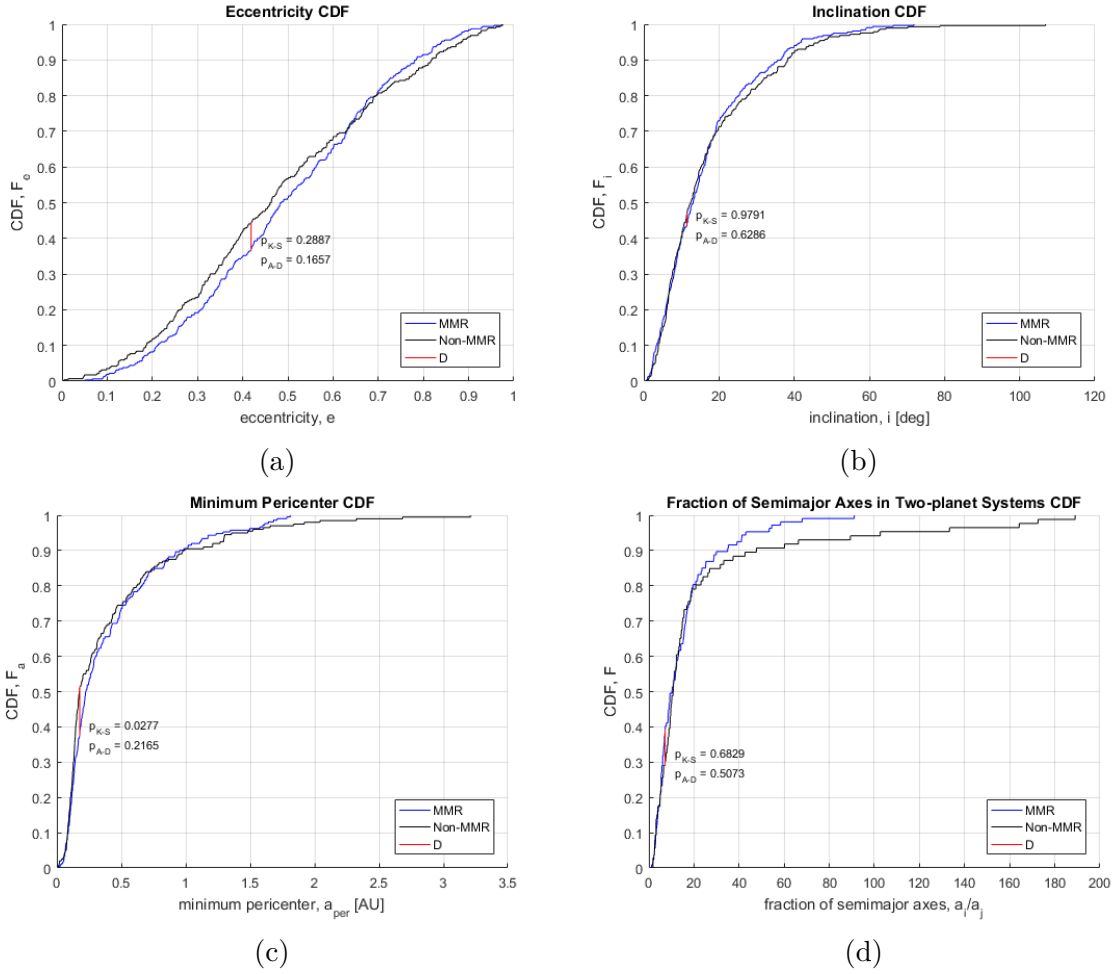

Figure 7.7: CDFs of surviving planets after the scattering phase, for K3C6. The results of MMR- and NON-MMR simulations are shown in the same plots for comparisons. Red vertical lines represent the K-S test statistic. K-S and A-D tests are performed to check the null hypothesis H_0. a) Eccentricity CDF. b) Inclination CDF. c) Minimum pericenter CDF. d) Ratios of semimajor axis in two-planet survivor systems CDF.

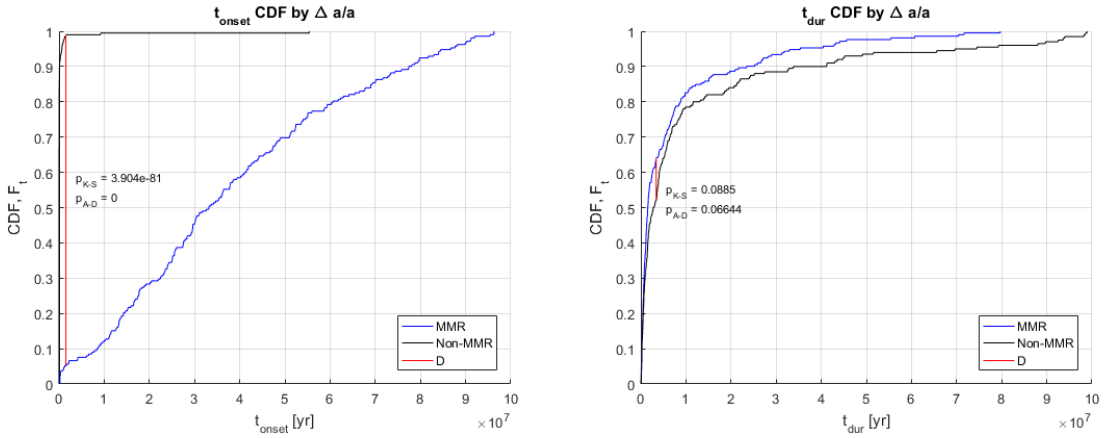

(a) (b)

Figure 7.8: CDFs of scattering phase timescales, for K3C6. The results of MMR- and NON-MMR simulations are shown in the same plots for comparisons. Red vertical lines represent the K-S test statistic. K-S and A-D tests are performed to check the null hypothesis H_0. a) Onset time of scattering phase CDF. b) Duration of scattering phase CDF.

7.1.2 3:2 Nominal Resonance Configuration

K4C4

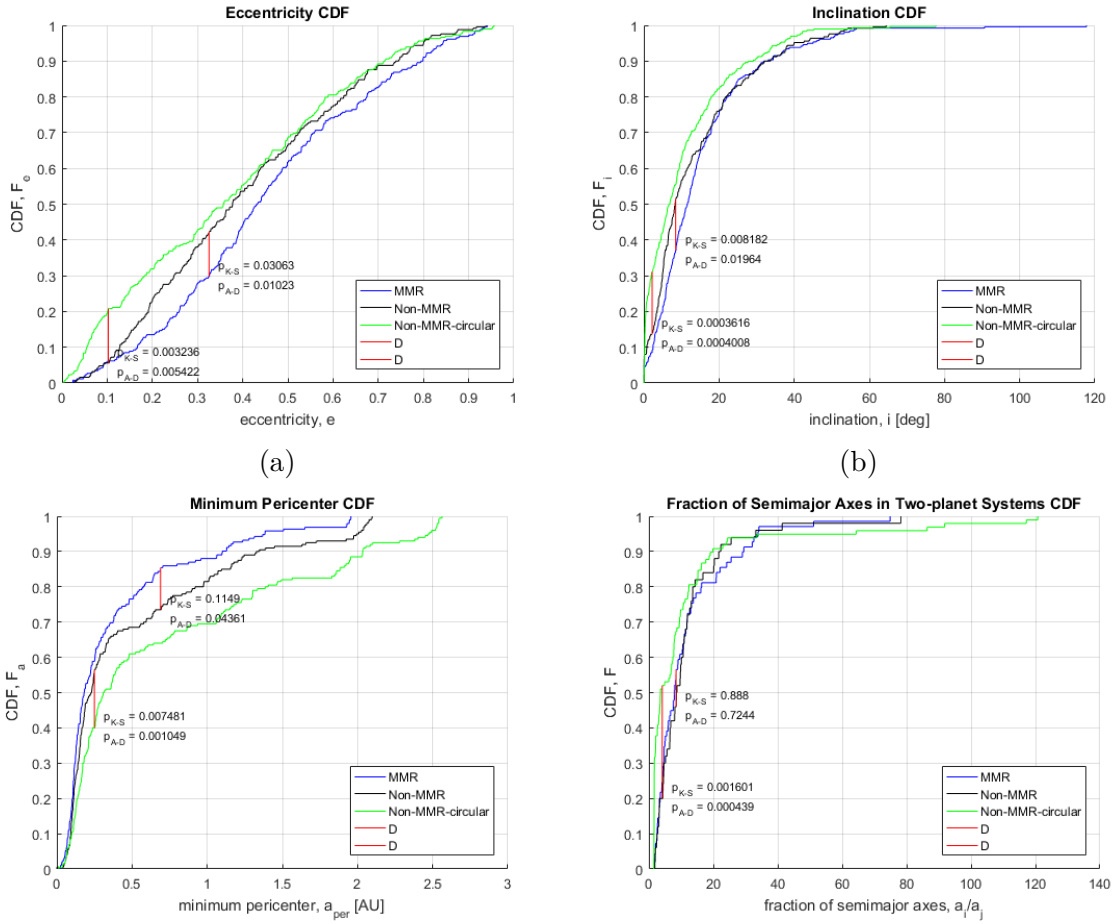

Figure 7.9: CDFs of surviving planets after the scattering phase, for K4C4. The results of MMR-, NON-MMR- and NON-MMR-CIRCULAR simulations are shown in the same plots for comparisons. Red vertical lines represent the K-S test statistic. K-S and A-D tests are performed to check the null hypothesis H_0. a) Eccentricity CDF. b) Inclination CDF. c) Minimum pericenter CDF. d) Ratios of semimajor axis in two-planet survivor systems CDF.

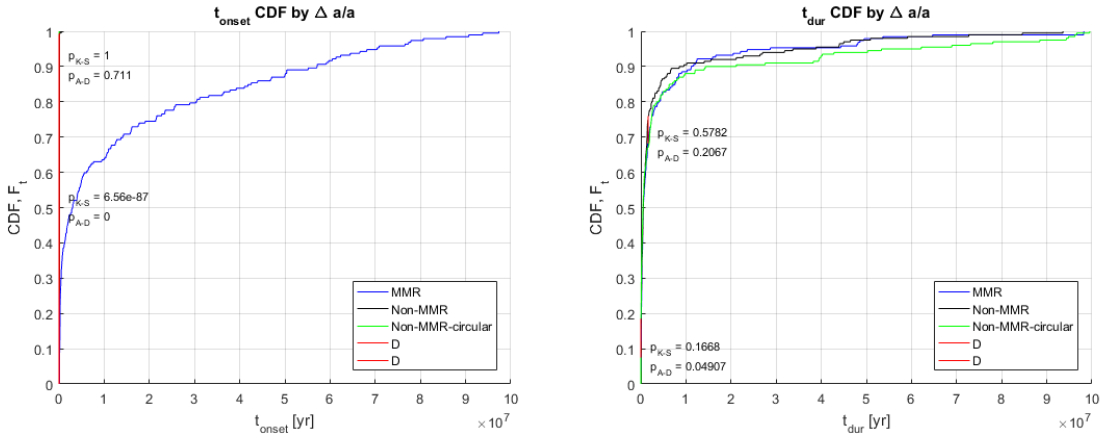

(a) (b)

Figure 7.10: CDFs of scattering phase timescales, for K4C4. The results of MMR-, NON-MMR- and NON-MMR-CIRCULAR simulations are shown in the same plots for comparisons. Red vertical lines represent the K-S test statistic. K-S and A-D tests are performed to check the null hypothesis H_0. a) Onset time of scattering phase CDF. b) Duration of scattering phase CDF.

K4C7

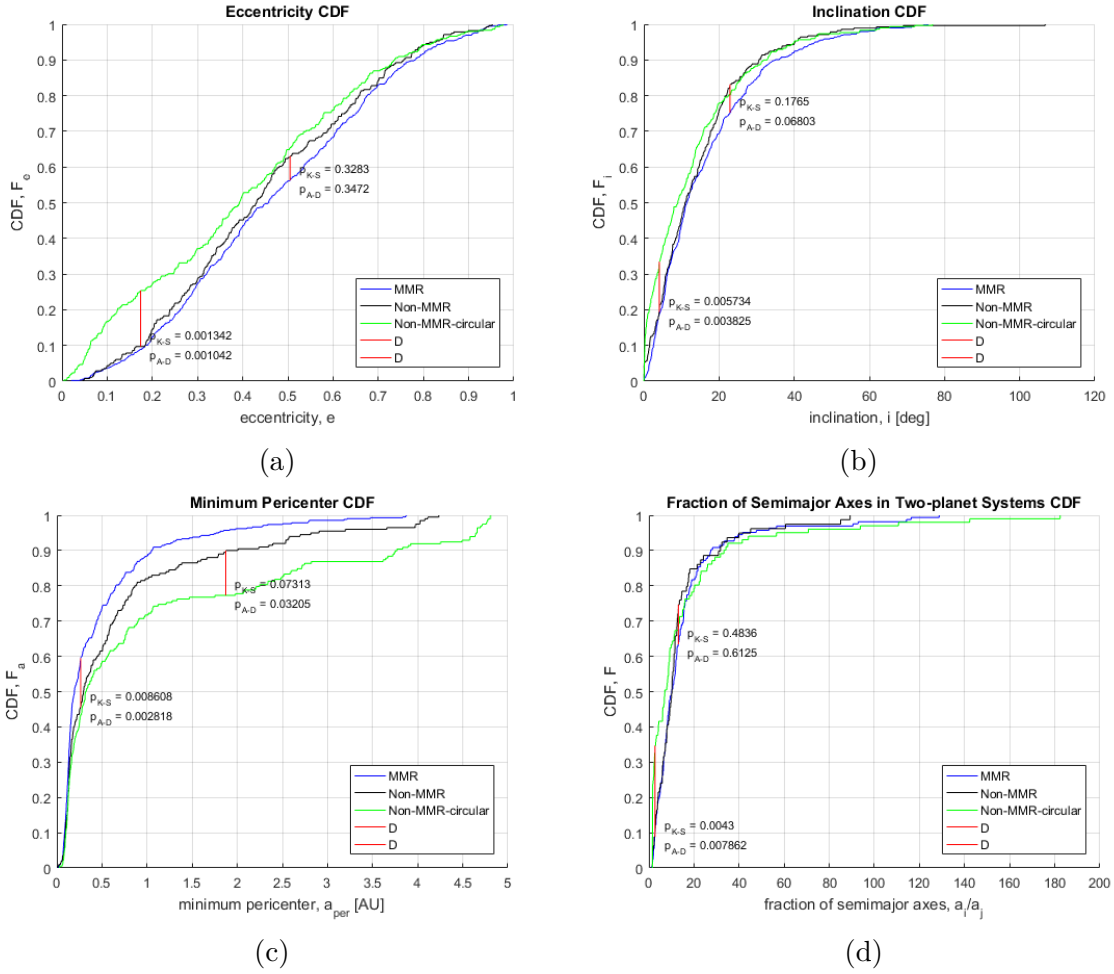

Figure 7.11: CDFs of surviving planets after the scattering phase, for K4C7. The results of MMR-, NON-MMR- and NON-MMR-CIRCULAR simulations are shown in the same plots for comparisons. Red vertical lines represent the K-S test statistic. K-S and A-D tests are performed to check the null hypothesis H_0. a) Eccentricity CDF. b) Inclination CDF. c) Minimum pericenter CDF. d) Ratios of semimajor axis in two-planet survivor systems CDF.

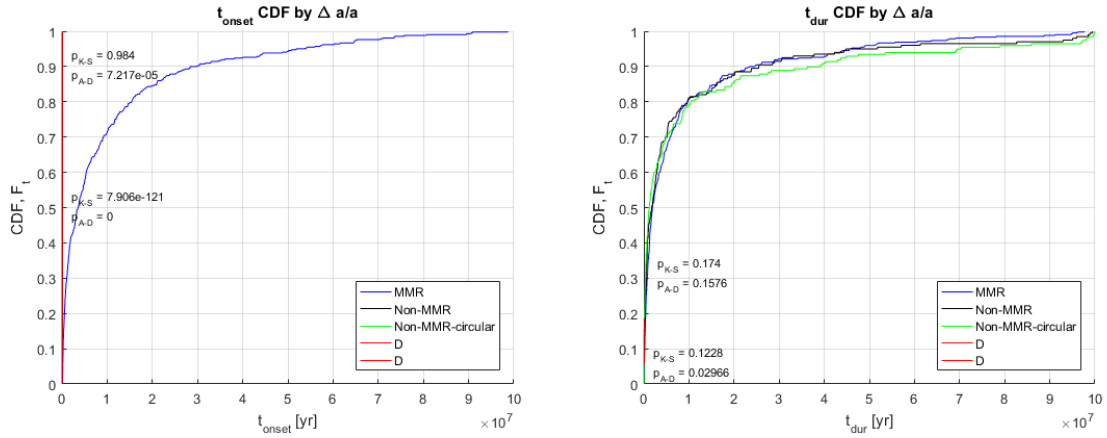

(a) (b)

Figure 7.12: CDFs of scattering phase timescales, for K4C7. The results of MMR-, NON-MMR- and NON-MMR-CIRCULAR simulations are shown in the same plots for comparisons. Red vertical lines represent the K-S test statistic. K-S and A-D tests are performed to check the null hypothesis H_0. a) Onset time of scattering phase CDF. b) Duration of scattering phase CDF.

7.2 B: Symplectic Integrators

Symplectic integrators solve the equations of motion of a constructed Hamiltonian H_c rather than the real Hamiltonian H of the system. The advantage of this is that there is no buildup of energy errors over time. Instead the system is solved for H_c exactly and the only error is the difference between H_c and H.

The Hamiltonian of a planetary system is the sum of kinetic- and potential energy,

$$H = \sum_i \frac{p_i^2}{2m_i} - G\sum_i m_i \sum_{j=i+1} \frac{m_j}{r_{ij}}, \tag{7.1}$$

where p_i is the momentum of body i, m_i is the mass of body i and r_{ij} is the separation between body i and j. We can express the position x_i and momentum p_i of a body using

$$\frac{dx_i}{dt} = \frac{\partial H}{\partial p_i}, \tag{7.2}$$

$$\frac{dp_i}{dt} = -\frac{\partial H}{\partial x_i}. \tag{7.3}$$

Any quantity of the system, q, can then be expressed as

$$\frac{dq}{dt} = \sum_i \left(\frac{\partial q}{\partial x_i}\frac{dx_i}{dt} + \frac{\partial q}{\partial p_i}\frac{dp_i}{dt} \right) = \sum_i \left(\frac{\partial q}{\partial x_i}\frac{\partial H}{\partial p_i} + \frac{\partial q}{\partial p_i}\frac{\partial H}{\partial x_i} \right) = Fq. \tag{7.4}$$

Integrating to solve for q gives (Chambers 1999)

$$q(t) = e^{\tau F} q(t-\tau) = \left(1 + \tau F + \frac{\tau^2 F^2}{2} + ...\right) q(t-\tau), \tag{7.5}$$

where τ is the integration time step. This is still unsolvable analytically when we are dealing with three or more bodies. However, the trick here is to split the Hamiltonian into several parts, each one solvable separately. So $F = A + B$ and

$$q(t) = e^{\tau(A+B)} q(t-\tau). \tag{7.6}$$

We now have $H = H_A + H_B$. Importantly, the operators A and B are generally not commutative. Therefore we generally have $e^{\tau A} e^{\tau B} \neq e^{\tau(A+B)}$. However, by splitting F into appropriate parts A and B (most often A and B are separately analytically solvable) $q(t) = e^{\tau A} e^{\tau B} q(t-\tau)$ can be solved for exactly. First, q is evolved through H_A for one time step, as seen in equation 7.5. Then the resulting q is evolved through H_B for one time step. This is a first order symplectic integrator. A second order symplectic integrator would solve the system for

$$q(t) = e^{\tau B/2} e^{\tau A} e^{\tau B/2} q(t-\tau). \tag{7.7}$$

This equivalent to solving the system for a constructed Hamiltonian $H_c \approx H$.

The symplectic integrator conserves the constructed Hamiltonian exactly. This means that the energy error does not grow with iterations. The error induced by the symplectic integrator is the difference $\Delta H = H_c - H$ and it depends on τ and the splitting of F. Therefore to prevent energy error build up, we keep τ constant. As shown in Saha & Tremaine (1992) the hamiltonian error ΔH of a symplectic integrator is given by

$$\Delta H \propto \epsilon \tau^n, \tag{7.8}$$

where ϵ is given by $B \sim \epsilon A$. This means that ΔH decreases when H_A is dominant over H_B. The constructed hamiltonian H_c more resembles the real H if the splitting is such that $H_A \gg H_B$. n is the order of the integrator.

7.3 C: Testing of Migration

7.3.1 Change of Coordinate System

In this section I convert vectors from the reference coordinate system (x, y, z) used in equations 3.14, 3.15 and 3.16 to the orbital coordinate system (r, t, z_o) used for the perturbing acceleration in equation 3.21. The goal is to express R^*, T^* and N^* in terms of τ_a, τ_e and τ_i.

I Start with $\mathbf{k} = (0, 0, 1)$ in equation 3.16. This is the vector perpendicular to the reference plane. By using conversion formulae from reference plane to orbital plane (given in section 2.8 of Murray & Dermott 1999), we have

$$\begin{bmatrix} x \\ y \\ z \end{bmatrix} = \mathbf{P}_1\mathbf{P}_2\mathbf{P}_3 \begin{bmatrix} x_{orb} \\ y_{orb} \\ z_{orb} \end{bmatrix} \qquad \Rightarrow \qquad \begin{bmatrix} x_{orb} \\ y_{orb} \\ z_{orb} \end{bmatrix} = \mathbf{P}_1^{-1}\mathbf{P}_2^{-1}\mathbf{P}_3^{-1} \begin{bmatrix} 0 \\ 0 \\ 1 \end{bmatrix} \tag{7.9}$$

where $\mathbf{P}_1$, $\mathbf{P}_2$ and $\mathbf{P}_3$ are conversion vectors between the reference plane and the orbital plane given in Murray & Dermott (1999). Making use of these yields $\mathbf{k}$ in Cartesian orbital coordinates $x_{orb}, y_{orb}, z_{orb}$

$$\mathbf{k} = \begin{bmatrix} sin\,\omega\, sin\, i \\ cos\,\omega\, sin\, i \\ cos\, i \end{bmatrix} \tag{7.10}$$

I express this in therms of the radius vector $\mathbf{r}$ and the tangential vector $\mathbf{t}$ by rotating the coordinate system along the orbital angle, the true anomaly f, in the orbital plane

$$\mathbf{r} = x_o\, cos\, f + y_o\, sin\, f, \tag{7.11}$$
$$\mathbf{t} = -x_o\, sin\, f + y_o\, cos\, f, \tag{7.12}$$

and finally we have

$$\mathbf{k} = \begin{bmatrix} sin\,\omega\, sin\, i\, cos\, f + cos\,\omega\, sin\, i\, sin\, f \\ -sin\,\omega\, sin\, i\, sin\, f + cos\,\omega\, sin\, i\, cos f \\ cos\, i \end{bmatrix} \tag{7.13}$$

The position coordinate and the velocity coordinate expressed in terms of $\mathbf{r}$, $\mathbf{t}$ and $\mathbf{z}_o$ are more straightforward

$$\mathbf{r} = (r, 0, 0), \tag{7.14}$$
$$\mathbf{v} = (\dot{r}, r\dot{f}, 0), \tag{7.15}$$

where $\dot{r}$ is the radial velocity and $\dot{f}$ is the angular velocity. Since we are in the orbital plane there cannot be any velocity in the $\mathbf{z}_o$-direction

From Murray & Dermott (1999) section 2.3 I make use of

$$\dot{r} = \frac{na}{\sqrt{1-e^2}} e\, sin\, f, \tag{7.16}$$
$$r\dot{f} = \frac{na}{\sqrt{1-e^2}} \left(1 + e\, cos\, f\right), \tag{7.17}$$

where r is given by equation 2.1. We are now in position to rewrite equations 3.14, 3.15

and 3.16 using equations 7.13, 7.14 and 7.15

$$\mathbf{a}_a = -\left(\frac{\dot{r}}{\tau_a}\hat{\mathbf{r}} + \frac{r\dot{f}}{\tau_a}\hat{\mathbf{t}}\right), \tag{7.18}$$

$$\mathbf{a}_e = -2\frac{\dot{r}}{\tau_e}\hat{\mathbf{r}}, \tag{7.19}$$

$$\mathbf{a}_i = -2\frac{(k_r\dot{r} + k_t r\dot{f})\mathbf{k}}{\tau_i}, \tag{7.20}$$

with $\dot{r}$ and $r\dot{f}$ given by equations 7.16 and 7.17. We see that a_a contributes to R^* and T^*, a_e only contributes to R^* and a_i contributes to all three directions through $\mathbf{k}$. Using, equations 7.18, 7.19 and 7.20 the expressions for R^*, T^* and N^* then becomes

$$R^* = \dot{r}\left(\frac{1}{\tau_a} + \frac{2}{\tau_e} + \frac{2k_r^2}{\tau_i}\right) - r\dot{f}\left(\frac{2k_r k_t}{\tau_i}\right), \tag{7.21}$$

$$T^* = -r\dot{f}\left(\frac{1}{\tau_a} + \frac{2k_t^2}{\tau_i}\right) - \dot{r}\left(\frac{2k_r k_t}{\tau_i}\right), \tag{7.22}$$

$$N^* = -2\left(\frac{\dot{r}k_r}{\tau_i} + \frac{r\dot{f}k_t}{\tau_i}\right)k_z, \tag{7.23}$$

with k_r, k_t and k_z according to equation 7.13.

7.3.2 Orbital Averaging

From Murray & Dermott (1999) chapter 2 we have the following useful relations between f, E and M

$$cos\, E = cos\, M + \frac{e}{2}(cos\, 2M - 1) + \mathcal{O}(e^2), \tag{7.24}$$

$$sin\, f = sin\, M + e\, sin\, 2M + \mathcal{O}(e^2), \tag{7.25}$$

$$cos\, f = cos\, M + e\,(cos\, 2M - 1) + \mathcal{O}(e^2). \tag{7.26}$$

Using first order in e, I substitute into equations 3.22, 3.23 and 3.24 and integrate over 0 to 2π in dM to obtain the orbital averaged evolution $\langle\dot{a}\rangle$, $\langle\dot{e}\rangle$ and $\langle\dot{i}\rangle$. The integration of such equations is non-trivial and thus a symbolic integrator, INTEGRATE in MATHEMATICA, was used. The result is

$$\langle\dot{a}\rangle = f_a(a, e, i, \omega, \tau_a, \tau_e, \tau_i), \tag{7.27}$$

$$\langle\dot{e}\rangle = f_e(e, i, \omega, \tau_a, \tau_e, \tau_i), \tag{7.28}$$

$$\langle\dot{i}\rangle = f_i(e, i, \omega, \tau_i), \tag{7.29}$$

where f_a, f_e and f_i are some complex functions of the variables stated in the respective equation above.

7.3.3 Example of Migration Implementation

As an instructive example we show the effect of a_a on a simple planetary orbit with $e = i = 0$. Combining equations 3.22, 7.13, 7.17 and 7.22 we obtain

$$\frac{da}{dt} = -\frac{2a}{\tau_a}. \tag{7.30}$$

This single differential equation can be solved analytically to obtain

$$a(t) = a_0\, e^{-\frac{2t}{\tau_a}}. \tag{7.31}$$

We can see here that the timescale τ_a sets the migration rate.

7.4 D: Hypothesis Tests

7.4.1 Two-sample Kolmogorov-Smirnov (K-S) test

In a two-sample $K - S$ test the test statistic D is the greatest vertical distance between the two CDFs for any given measurable quantity. For two CDFs $S_n(x)$ and $R_m(x)$ where x are the measured quantities and n and m are the number of data points,

$$D = max|S_n(x) - R_m(x)|. \tag{7.32}$$

The null hypothesis H_0 is that the two CDFs belong to the same underlying distribution.

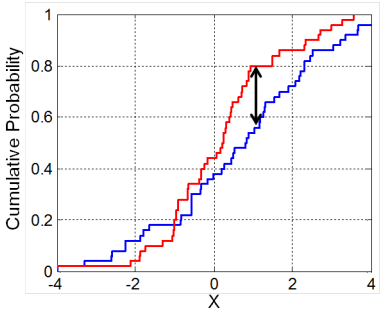

Figure 7.13: Two cumulative distribution functions of an arbitrary parameter X are compared by a two-sample K-S test. The black arrow shows the observed K-S test statistic D_{obs} (equation 7.32).

By randomly drawing two CDFs from a single underlying distribution we can measure the

test statistic D. By repeating this multiple times we obtain a distribution of Ds given that H_0 is true. From the MMR and NON-MMR simulations I then get two CDFs that I want to compare. I measure the observed test statistic D_{obs} by equation 7.32 above. The p-value is then the probability of randomly drawing a D from the true distribution of Ds that is equal or more extreme ($|D| \geq |D_{obs}|$). p is given by the following formula for the K-S test:

$$p = 2\sum_{j=1}^{\infty}(-1)^{(j-1)}\, exp\left(-2j^2\left(D_{obs}\sqrt{\frac{nm}{n+m}}\right)^2\right). \tag{7.33}$$

7.4.2 Two-sample Anderson-Darling (A-D) test

A two-sample A-D test is similar to a K-S test but with a different test statistic that is more sensitive to the wings of the CDFs. In Pettitt (1976) a simplified test statistic is given for the two CDFs $S_n(x)$ and $R_m(x)$ by

$$A^2_{nm} = \frac{1}{nm}\sum_{i=1}^{N-1}\frac{(M_iN - ni)^2}{i(N-i)}, \tag{7.34}$$

where M_i is the number of data points x less than or equal to the x in $H(x)$. $H(x)$ is the combined CDF given by $H(x) = \frac{nS_n(x)+mR_m(x)}{N}$. N is the total number of data points $N = n + m$. By sampling two CDFs from a single underlying distribution A^2_{nm} can be calculated. Repeating this process leads to a distribution of A^2_{nm} given that H_0 is true. From my MMR and NON-MMR CDFs I can calculate an observed test statistic $A^2_{nm,obs}$. The p-value is the probability of randomly drawing an A^2_{nm} from the distribution where H_0 is true that is equal or more extreme than $A^2_{nm,obs}$. For details on the distribution of A^2_{nm} given that H_0 is true and how to compute p I refer to Pettitt (1976).

Bibliography

Baruteau, C., Crida, A., Paardekooper, S.-J., et al. 2014, Protostars and Planets VI, 667

Bitsch, B., Crida, A., Libert, A.-S., & Lega, E. 2013, A&A, 555, A124

Bitsch, B., Johansen, A., Lambrechts, M., & Morbidelli, A. 2015, A&A, 575, A28

Bitsch, B., Lambrechts, M., & Johansen, A. 2015, A&A, 582, A112

Bitsch, B., & Kley, W. 2010, A&A, 523, A30

Bitsch, B., & Kley, W. 2011, A&A, 530, A41

Brouwer, D., & Clemence, G. M. 1961, Mechanics of Composite Materials,

Carrera, D., Davies, M. B., & Johansen, A. 2016, MNRAS, 463, 3226

Chambers, J. E. 1999, MNRAS, 304, 793

Chambers, J. E., Wetherill, G. W., & Boss, A. P. 1996, Icarus, 119, 261

Chatterjee, S., Ford, E. B., Matsumura, S., & Rasio, F. A. 2008, ApJ, 686, 580-602

Correia, A. C. M., Delisle, J.-B., & Laskar, J. 2017, arXiv:1702.02494

Cresswell, P., Dirksen, G., Kley, W., & Nelson, R. P. 2007, A&A, 473, 329

Cumming, A., & Dragomir, D. 2010, MNRAS, 401, 1029

Davies, M. B., Adams, F. C., Armitage, P., et al. 2014, Protostars and Planets VI, 787

Ford, E. B., Havlickova, M., & Rasio, F. A. 2001, Icarus, 150, 303

Goldreich, P., & Tremaine, S. 1980, ApJ, 241, 425

Haisch, K. E., Jr., Lada, E. A., & Lada, C. J. 2001, ApJ, 553, L153

Johansen, A., Blum, J., Tanaka, H., et al. 2014, Protostars and Planets VI, 547

Johansen, A., & Lambrechts, M. 2017, Annual Review of Earth and Planetary Sciences, 45, 359

Jurić, M., & Tremaine, S. 2008, ApJ, 686, 603-620

Kley, W. 2000, MNRAS, 313, L47

Lee, M. H., & Peale, S. J. 2002, ApJ, 567, 596

Libert, A.-S., & Tsiganis, K. 2011, Celestial Mechanics and Dynamical Astronomy, 111, 201

Lin, D. N. C., & Papaloizou, J. 1986, ApJ, 309, 846

Marzari, F., & Weidenschilling, S. J. 2002, Icarus, 156, 570

Murray, C. D., & Dermott, S. F. 1999, Solar system dynamics by C.D. Murray and S.F. McDermott. (Cambridge, UK: Cambridge University Press), ISBN 0-521-57295-9 (hc.), ISBN 0-521-57297-4 (pbk.).,

Nelson, R. P., Papaloizou, J. C. B., Masset, F., & Kley, W. 2000, MNRAS, 318, 18

Papaloizou, J. C. B., & Larwood, J. D. 2000, MNRAS, 315, 823

Petrovich, C., Tremaine, S., & Rafikov, R. 2014, ApJ, 786, 101

Saha, P., & Tremaine, S. 1992, AJ, 104, 1633

Shakura, N. I., & Sunyaev, R. A. 1973, A&A, 24, 337

Sotiriadis, S., Libert, A.-S., Bitsch, B., & Crida, A. 2017, A&A, 598, A70

Williams, J. P., & Cieza, L. A. 2011, ARA&A, 49, 67

Winn, J. N., & Fabrycky, D. C. 2015, ARA&A, 53, 409

Wittenmyer, R. A., Butler, R. P., Tinney, C. G., et al. 2016, ApJ, 819, 28

Wittenmyer, R. A., Tinney, C. G., O'Toole, S. J., et al. 2011, ApJ, 727, 102

Yoshida, H. 1993, Celestial Mechanics and Dynamical Astronomy, 56, 27